Investigations of Local Reaction Conditions During Electrochemical CO_2 Reduction by *in operando* Magnetic Resonance Spectroscopy

Untersuchung der lokalen Reaktionsbedingungen bei der elektrochemischen CO_2 Reduktion mittels *in operando* Magnetresonanz-Spektroskopie

Von der
Fakultät für Mathematik, Informatik und Naturwissenschaften
der RWTH Aachen University
zur Erlangung des akademischen Grades eines
Doktors der Ingenieurwissenschaften *genehmigte*

Dissertation

vorgelegt von
Michael Schatz, MSc
geboren in
Moers

Berichter: Univ.-Prof. Dr. rer. nat. Josef Granwehr
Univ.-Prof. Dr.-Ing. Matthias Wessling
Univ.-Prof. Dr. rer. nat. Rüdiger-A. Eichel

Tag der mündlichen Prüfung: 22. November 2023
Diese Dissertation ist auf den Internetseiten der Universitätsbibliothek verfügbar.

RWTH AACHEN UNIVERSITY

Eidesstattliche Erklärung

Michael Schatz

erklärt hiermit, dass diese Dissertation und die darin dargelegten Inhalte die eigenen sind und selbstständig, als Ergebnis der eigenen originären Forschung, generiert wurden.

Hiermit erkläre ich an Eides statt

1. Diese Arbeit wurde vollständig oder größtenteils als Doktorand dieser Fakultät und Universität angefertigt;

2. Sofern irgendein Bestandteil dieser Dissertation zuvor für einen akademischen Abschluss oder eine andere Qualifikation an dieser oder einer anderen Institution verwendet wurde, wurde dies klar angezeigt;

3. Wenn immer andere eigene- oder Veröffentlichungen Dritter herangezogen wurden, wurden diese klar benannt;

4. Wenn aus anderen eigenen- oder Veröffentlichungen Dritter zitiert wurde, wurde stets die Quelle hierfür angegeben. Diese Dissertation ist vollständig meine eigene Arbeit, mit der Ausnahme solcher Zitate;

5. Alle wesentlichen Quellen von Unterstützung wurden benannt;

6. Wenn immer ein Teil dieser Dissertation auf der Zusammenarbeit mit anderen basiert, wurde von mir klar gekennzeichnet, was von anderen und was von mir selbst erarbeitet wurde;

7. Ein Teil oder Teile dieser Arbeit wurden zuvor veröffentlicht und zwar in:

   (a) Michael Schatz (Korrespondenzautor), Sven Jovanovic, Rüdiger-A. Eichel and Josef Granwehr, **Quantifying local pH changes in carbonate electrolyte during copper-catalysed CO_2 electroreduction using in operando ^{13}C NMR**, *Scientific Reports*, Volume 12, Number 1 (2022).

   (a) Michael Schatz (Korrespondenzautor), Johannes Kochs, Sven Jovanovic, Rüdiger-A. Eichel and Josef Granwehr, **Interplay of local pH and cation hydrolysis**

during electrochemical CO_2 reduction visualized by *in operando* chemical shift resolved Magnetic Resonance Imaging, *The Journal of Physical Chemistry C* (2023), Volume 127, Number 38 (2023).

_____ (Datum) _____ (Unterschrift)

Danksagung

Drei Jahre Promotion liegen hinter mir, mit unzähligen Experimenten, einigen Präsentationen und Veröffentlichungen, Tage mit ernüchternden Fehlschlägen aber auch aufregenden Erfolgen. Im Alleingang ist solch ein Projekt nicht zu bewältigen, daher möchte ich mich bei all den lieben Menschen bedanken, die mich auf diesem Weg unterstützt haben.

Zuerst möchte ich meinem Doktorvater, Prof. Dr. Josef Granwehr, danken, der mir mit seinem Glauben daran, dass ein Verfahrenstechniker es mit der Magnetresonanz aufnehmen könne, ermöglichte, dieses spannende Projekt in der Spektroskopie Gruppe des IEK-9 zu übernehmen. Auch danke ich ihm für die zahlreichen Stunden, die er sich genommen hat, um mit viel Leidenschaft die Eigenarten der *in operando* NMR auszudiskutieren.

Des Weiteren danke ich Prof. Dr-Ing. Matthias Wessling für seine stete Unterstützung seit meiner Zeit als Hiwi und Masterand an der CVT und für seinen Einsatz als zweiter Berichter. Meinem Institutsleiter und dritten Berichter Prof. Dr. Rüdiger-A. Eichel danke ich für die Möglichkeit, am IEK-9 zu arbeiten, und für seine aufrechte Begeisterung für meine “lokale pH-Wert”-Methode.

Für die intensive Betreuung während meiner Doktorandenzeit danke ich Dr. Sven Jovanovic. Von Dir habe ich alles gelernt, was man zum Bestehen seiner Promotion braucht. Danke dafür, dass Du immer ein offenes Ohr für Fragen jeglicher Art hattest und für Dein wertvolles Feedback.

In Zeiten einer weltweiten Pandemie taten die ganz normalen Gespräche mit Kolleg*innen besonders gut, egal ob mit IEK-9 Doktorand*innen im Seecasino oder mit der Spektroskopie-Gruppe in der Halle. Nicht nur persönlich sondern auch fachlich wertvoll waren die Gespräche mit Philipp Schleker und Emmanouil Veroutis. Vielen Dank für Euren Input. Johannes Kochs möchte ich danken für die sorgfältige und geduldige Durchführung vieler wichtiger Experimente für diese Arbeit.

Wie bereichernd es sein kann, mit langjährigen Freunden zusammen am selben Institut zu arbeiten, durfte ich dank Julian und Max erfahren. Vielen Dank für unzählige Jokes und Gespräche in der Zoe oder in der Küche in 09.7, ohne die meine Zeit in Jülich nur halb so schön gewesen wäre. Ich freue mich auf das Bewerbungsgespräch mit Euch als Trio.

Meinen Eltern danke ich für ihre aufopferungsvolle und bedingungslose Unterstützung. Meine Freiheit ist Euer Lebenswerk.

Zuletzt danke ich meiner wundervollen Frau Marie, die selbst in den dunkelsten Novembertagen mein Sonnenschein war – und immer sein wird.

Abstract

In this work, *in operando* magnetic resonance techniques for the investigation of the Cu-catalysed electrochemical CO_2 reduction were developed and employed. The primary focus was on understanding the local reaction conditions, specifically the local pH value at the working electrode and the effect of cations on it. Magnetic Resonance Imaging (MRI) was utilised to provide spatial resolution in electrode-vicinity. Increasing pH profiles evolving during electrochemical CO_2 reduction were observed for $NaHCO_3$ and $KHCO_3$ electrolytes with varying concentrations and the interplay between buffer capacity and cation identity was elucidated.

In the first part of the thesis, the pH determination method based on the ^{13}C Nuclear Magnetic Resonance (NMR) resonances of CO_2, HCO_3^- and CO_3^{2-} was presented and validated for a pH range between ca. 4 to 12. Here, the Hendersson–Hasselbalch equation was employed to determine the pH in electrode-proximity during electrolysis. Increasing local pH values and resulting formate production were in accordance with literature data.

The second part dealt with the development of the established cell setup towards application of MRI using magnetic field gradients along the longitudinal axis of the NMR tube. Three cell designs were presented and assessed for their reproducibility in terms of current–voltage characteristics and product distribution of electrochemical CO_2 reduction on Cu. To estimate the influence of distortions of magnetic field and radiofrequency field, frequency encoded and purely phase encoded imaging with chemical shift resolution was introduced. These imaging methods allowed for the identification of systematic errors during *in operando* investigations under electrolytic conditions, aligning with theoretical predictions.

In the third part, the pH determination method was applied on spatially resolved ^{13}C NMR spectra of CO_2 saturated $NaHCO_3$ and $KHCO_3$ electrolytes, yielding the local pH as a function of distance to the electrode. In combination with ^{23}Na imaging, increased buffer capacity of $KHCO_3$ electrolytes compared to $NaHCO_3$ was confirmed and experimental evidence of the dehydration of Na^+ in electrode-proximity was provided.

Zusammenfassung

Zur Untersuchung der elektrochemischen CO_2 Reduktion an Kupfer wurden im Rahmen dieser Arbeit *in operando* Magnetresonanz Methoden entwickelt und angewendet. Hierbei standen lokale Reaktionsbedingungen im Fokus, insbesondere lokale pH-Werte an der Arbeitselektrode und der Einfluss von Kationen auf diesen. Pulssequenzen aus der Magnetresonanztomographie (MRT) wurden verwendet, um das Volumen in der Nähe der Arbeitselektrode räumlich aufzulösen. Bei der elektrochemischen CO_2-Reduktion wurden steigende pH-Profile für $NaHCO_3$ und $KHCO_3$ Elektrolyte mit unterschiedlichen Konzentrationen festgestellt, und das Zusammenspiel zwischen Pufferkapazität des Elektrolyten und der Kationengröße verdeutlicht.

Im ersten Teil der Arbeit wurde eine Methode zur pH-Bestimmung basierend auf den ^{13}C-Resonanzen von CO_2, HCO_3^- and CO_3^{2-} mittels Kernspinresonanz (NMR) vorgestellt und für einen pH-Bereich von ca. 4 bis 12 validiert. Dabei wurde die Henderson–Hasselbalch Gleichung verwendet, um den pH-Wert in Elektrodennähe während des Elektrolysebetriebs zu bestimmen. Steigende lokale pH-Werte und die daraus resultierende Formiatproduktion stimmten mit Literaturdaten überein.

Der zweite Teil beschreibt die Weiterentwicklung des etablierten Zellsetups für die Anwendung von MRT Pulssequenzen mittels Magnetfeldgradienten entlang der Längsachse des NMR-Röhrchens. Drei Zelldesigns wurden entwickelt und hinsichtlich der Reproduzierbarkeit der Strom-Spannungs-Charakteristik und der Produktverteilung der elektrochemischen CO_2 Reduktion an Kupfer bewertet. Zur Abschätzung des Einflusses von Verzerrungen des magnetischen Felds und des Hochfrequenzfelds wurden Pulssequenzen mit Frequenzkodierung und reiner Phasenkodierung mit Auflösung der chemischen Verschiebung präsentiert. In Übereinstimmung mit Simulationen ermöglichten diese Bildgebungstechniken die Beurteilung systematischer Fehler bei den *in operando* Untersuchungen unter elektrolytischen Bedingungen.

Im dritten Teil wurde die pH-Bestimmungsmethode auf räumlich aufgelöste ^{13}C-NMR-Spektren von CO_2-gesättigten $NaHCO_3$ und $KHCO_3$ Elektrolyten angewendet, wodurch der lokale pH-Wert als Funktion der Entfernung zur Elektrode bestimmt wurde. In Kombination mit der ^{23}Na Untersuchungen wurde eine höhere Pufferkapazität beim $KHCO_3$ Elektrolyt im Vergleich zu $NaHCO_3$ festgestellt. Schließlich konnte die Dehydratisierung von Na^+ in der Nähe der Elektrode experimentell erwiesen werden.

Contents

Glossary

$\mathbf{Ag^+}$	Silver ion
$\mathbf{Li^+}$	Lithium ion
$\mathbf{C_{2+}}$	Hydrocarbons with two or more carbon atoms
$\mathbf{CO}$	Carbon monoxide
$\mathbf{CO_2}$	Carbon dioxide
$\mathbf{CO_3^{2-}}$	Carbonate anion
$\mathbf{H^+}$	Hydrogen ion
$\mathbf{HCO_3^-}$	Bicarbonate anion
$\mathbf{KHCO_3}$	Potassium bicarbonate
$\mathbf{NaHCO_3}$	Sodium bicarbonate
$\mathbf{K^+}$	Potassium ion
$\mathbf{KOH}$	Potassium hydroxide
$\mathbf{N_2}$	Molecular nitrogen
$\mathbf{Na^+}$	Sodium ion
$\mathbf{OH^-}$	Hydroxide ion
$\mathbf{PO_4^{3-}}$	Phosphate ion
$\mathbf{HPO_4^{2-}}$	Hydrogen phosphate ion
$\mathbf{H_2PO_4^-}$	Dihydrogen phosphate ion

Acronyms

CA	Chronoamperometry
CCS	carbonate chemical shift
CE	Counter Electrode
CP	Chronopotentiometry
CSI	Chemical Shift Imaging
CV	Cyclovoltammetry
DFT	Density Functional Theory
eCO_2R	electrochemical Carbon Dioxide Reduction
EDL	Electrical Double Layer
EEI	electrode/electrolyte interface
EU	European Union
FE	Faradaic Efficiency
FEM	Finite Element Method
FID	Free Induction Decay
FOV	Field of View
FWHM	Full Width at Half Maximum
GDE	Gas Diffusion Electrode
HER	Hydrogen Evolution Reaction
HH	Hendersson–Hasselbalch
IHP	Inner Helmholtz Plane
LSV	Linear Sweep Voltammetry
MEA	Membrane Electrode Assembly
MHD	magnetohydrodynamic
MRI	Magnetic Resonance Imaging
NHE	Normal Hydrogen Electrode
NMR	Nuclear Magnetic Resonance
OCV	Open Circuit Voltage
OHP	Outer Helmholtz Plane
PEEK	polyether ether ketone
PLA	polylactide
PTFE	Polytetrafluoroethylene

RDS	Rate Determining Step
RE	Reference Electrode
RF	Radio Frequency
RHE	Reversed Hydrogen Electrode
SECM	scanning electrochemical microscopy
SEIRAS	surface-enhanced infrared absorption spectroscopy
SERS	surface-enhanced Raman spectroscopy
SHE	Standard Hydrogen Electrode
TSP	trimethylsilylpropanoic acid
WE	Working Electrode

Notations

$a(\mathbf{A})$	Activity of A
β	Flip angle of NMR pulse
B_0	Magnetic field in NMR experiment
B_z	Magnetic field in z-direction
B_1	Radiofrequency field in NMR experiment
BW	Transmitter bandwidth
$\delta_{\mathbf{A}}$	Chemical shift of A
E	Voltage
ε	Standard error
e_0	Elementary charge
F	Faraday constant
G	Magnetic field gradient strength
γ	Gyromagetic ratio
$\hbar$	Reduced Planck's constant
H	Henry's constant
I	Current
i	Current density
k	Fourier transform of image dimension
L	Angular momentum
M	Magnetisation
M	Molar mass
m	Mass
$N_{\mathbf{A}}$	Avogadro constant
n	Number of transferred electrons
ω	Angular frequency
ω_0	Larmor frequency
ω_1	Nutation frequency
Ω	Offset frequency
$p(\mathbf{A})$	Partial pressure of A
ϕ_0	Equilibrium potential
ϕ_{00}	Standard potential

$\mathrm{p}K_a$	Ionisation constant of an acid
Q	Transferred charge
R	Universal gas constant
σ	Shielding constant
S	Spin quantum momentum
s	Integral of NMR resonance
$\mathbf{S_{ox}}$	Oxidized species
$\mathbf{S_{red}}$	Reduced species
T	Temperature
T_1	Longitudal relaxation time constant
T_2	Transverse relaxation time constant
T_2'	Additional dephasing of transverse relaxation time due to magnetic field inhomogeneities
T_2^*	Transverse relaxation time constant, considering additional dephasing due to magnetic field inhomogeneities
t	Time
t_d	Dwell time
t_g	Duration of gradient pulse
τ	Half echo time
t_p	Pulse length of RF pulse
t_{aq}	Acquisition time of NMR experiment
t_r	Repetition time of NMR experiment
v	Scan rate of potential sweep
z	Longitudinal direction of NMR experiments; direction of magnetic field and magnetic field gradients

List of Figures

List of Tables

Chapter 1

Introduction

In March 2023, Germany's solo effort to circumvent the complete phaseout of sales of internal combustion cars in the European Union (EU) fuelled the international discussion about CO_2-neutral combustibles [1–3]. EU leaders had agreed on a ban of new vehicles powered by fossil fuels as of 2035 in the context of EU's Green Deal, imposing a 100 % reduction in CO_2 emissions, but Germany's transport ministry forced a deal to exempt cars that run on synthetic, so called e-fuels, synthesised from CO_2 using renewable energy sources [4]. The EU's efforts are based on the Paris Agreement and the goals defined in it, which resolved on joint international endeavours to limit the global average temperature increase to 1.5 °C above pre-industrial levels or at least prevent warming of more than 2 °C [5]. Nonetheless, studies state that the current efforts of EU countries are not aligned with the 1.5 °C goal, and further measures to reduce CO_2 emissions have to be taken [6, 7].

To achieve this goal, rapid decarbonisation of all energy sectors using currently available measures is necessary. The combination of direct electrification, sector coupling, and the use of synthetic fuels in the mobility and heat sectors were considered decisive in reaching this goal [8–10]. However, decarbonisation should not be confused with defossilisation. In contrast to a decarbonised scenario, a defossilised scenario that includes synthetic carbon-based, but CO_2-neutral fuels in the energy transition benefits from already existing infrastructure and processing pathways [11, 12].

The electrochemical Carbon Dioxide Reduction (eCO_2R), driven by renewable sources, has the potential to promote defossilisation of fuels and platform chemicals. Acting simultaneously as stabilisation for the electricity grid due to fluctuations of wind and solar power systems, the transition towards a defossilised energy sector is further supported [12–14]. However, slow kinetics of the electrocatalysis and high reduction overpotentials lead to low energy efficiency of the process, and the competitive decomposition reaction of the solvent, *i.e.* Hydrogen Evolution Reaction (HER) usually, complicates the design of highly efficient processes [15].

The activation of CO_2 seems thermodynamically not favourable. The first electron transfer to form the CO_2^- radical intermediate has a very negative reduction potential of −1.9 V *vs.* Normal Hydrogen Electrode (NHE). Thus, catalyst engineering plays a significant role, as electrocatalysts stabilise the radical intermediate, leading to a less

negative reduction potential [14]. By the middle of last decade, the main factors preventing eCO_2R from widespread applications were determined as high overpotential, low catalytic activity, low selectivity for single products, and insufficient catalyst stability, which would make the process competitively unviable. These issues were addressed by engineering of new catalysts in terms of surface engineering, chemical modifications, nanostructures, but also investigations on the reaction mechanisms [16–18].

Along with the catalyst performance, recent research highlighted the importance of local reaction and process conditions at the electrode/electrolyte interface (EEI). Here, the complex interplay between catalyst, buffering ions and reactant was found to be crucial for the product selectivity [14, 17]. Especially the evolution of local pH, not only at the EEI but also in the diffusion layer, and its impact on product distributions were of interest [19].

To resolve the correlation of electrolyte parameters with reaction conditions in electrode proximity during electrolysis operation, *in operando* Nuclear Magnetic Resonance (NMR) and Magnetic Resonance Imaging (MRI) measurements are presented in this study. This way, information about all species dissolved in the electrolyte can be acquired simultaneously in an operating eCO_2R cell. To provide contextual information, important theoretical concepts are presented in chapter 2. After introducing electrochemical cells and reactions in general, it is specifically focused upon the eCO_2R. For this, the CO_2 chemistry in water has to be understood, before the influence of electrolyte parameters on product selectivity of eCO_2R are assessed. The fundamentals of magnetic resonance techniques are then presented, followed by an overview of the most important works on electrochemical cells for *in operando* NMR and MRI. Chapter 3 describes a methodology for the determination of local pH values in bicarbonate electrolytes, based on the ^{13}C resonances of HCO_3^-/CO_3^{2-} and CO_2. The electrochemical cell used in chapter 3 is subsequently adjusted to enable application of chemical shift resolved MRI pulse sequences, *i.e.* Chemical Shift Imaging (CSI), using magnetic field gradients along one dimension. All required advancement of the cell and the experimental procedures are presented and validated in chapter 4. In chapter 5, spatially resolved NMR spectra are acquired using CSI for varying initial concentrations of $NaHCO_3$ and $KHCO_3$ electrolyte. For $NaHCO_3$, additionally ^{23}Na CSI is applied to investigate changes in the Na^+ resonances. Finally, the thesis is summarised and an outlook is given that describes possible extensions of the method towards industrially more relevant operation conditions and refined spatial resolution.

Chapter 2

Theory

2.1 Electrochemical reactions

2.1.1 Electrochemical cells

Electrochemical systems are characterised by a transport of charge across the interface between an electronic conductor, *i.e.* an electrode, and an ionic conductor, *i.e.* an electrolyte [20]. In electrodes, charge is transferred in the form of freely moving electrons in metals, carbon-based materials or semiconductors, while in electrolytes, it is transferred by movement of ions, either solvated in liquids such as aqueous solutions or in solids such as ion exchange membranes [20, 21]. A simple electrochemical cell typically consists of two electrodes that are separated by at least one electrolytic phase. The electrodes are connected via conductors to either a power supply or a consumer. To control electrochemical conditions in the cell, an ampere meter with a resistance is connected in series, while a high impedance voltmeter is connected in parallel. When applying a potential by an external power supply, a current is induced through the cell, which moves negatively charged anions to the positively charged anode and positively charged cations to the negatively charged cathode. At the EEI, electrochemical reactions occur, which are the core of electrochemical investigations. A reaction taking place on one of the electrodes is called half cell reaction and is described by

$$\mathrm{S_{ox}} + n\mathrm{e^-} \rightleftharpoons \mathrm{S_{red}}\,, \tag{2.1}$$

with the oxidised species $\mathrm{S_{ox}}$, the reduced species $\mathrm{S_{red}}$ and the number of transferred electrons n. An example for such a so called redox couple is $\mathrm{Cu^{2+}} + 2\,\mathrm{e^-} \rightleftharpoons \mathrm{Cu}$, which describes the half cell reaction between $\mathrm{Cu^{2+}}$ ions and metallic Cu. This reaction equation shows the main difference between electronic and ionic conductor. The electronic conductor, such as a metal wire, is not modified during charge transfer, while the ionic conductor changes not only in local but also bulk concentration [20, 21].

The electrode, at which the reactions under investigation occurs, is called Working Electrode (WE). To standardise measured potentials, the so called Reference Electrode (RE) is chosen such that a half cell reaction of a redox couple with a reproducible composition takes place. In applications where passing charge across the RE is unwanted, an

additional Counter Electrode (CE) is introduced. The current is passed through the CE, while the potential is still measured *vs.* the RE [20, 21].

Referencing potentials

Since it is not possible to directly measure the potential between electrode and electrolyte of a redox couple, reference half cell reactions were chosen as standard by convention. To describe the equilibrium potential ϕ_0 of a half cell, the Nernst equation is introduced,

$$\phi_0 = \phi_{00} + \frac{RT}{nF} \ln \frac{a_{ox}}{a_{red}}\,, \tag{2.2}$$

with the molar gas constant R, the temperature T, the Faraday constant F, the activity of the oxidised species a_{ox} and the activity of the reduced species a_{red}. The standard potential ϕ_{00} of the electrochemical potential scale was set to the NHE by definition, which is equal to the Standard Hydrogen Electrode (SHE). The corresponding half cell reaction is $2\,\mathrm{H^+} + \mathrm{e^-} \rightleftharpoons \mathrm{H_2}$ at an inert platinum electrode. Since such a RE is impractical in regular laboratory use, REs of the second kind, such as the Ag/AgCl electrode, are applied. Here, the half cell reaction $\mathrm{AgCl} + \mathrm{e^-} \rightleftharpoons \mathrm{Ag} + \mathrm{Cl^-}$ takes place. The potential *vs.* NHE for a 1 M KCl solution is +0.2368 V. To consider the proton activity in the solution, the Reversed Hydrogen Electrode (RHE) is introduced as pH-dependent reference frame. The potential *vs.* RHE, E_{RHE}, can be converted to the potential *vs.* NHE, E_{NHE}, by [20, 21]

$$E_{NHE} = E_{RHE} - 0.058\ \mathrm{pH}\,. \tag{2.3}$$

Faradaic charge transfer

The potential that is measured by a high impedance voltmeter between WE and RE at no current flow is called the Open Circuit Voltage (OCV). If the potential at the WE has to be made more negative by an external power supply in order to set in a current flow, one speaks of an electrolysis cell. Any further negative potential from this onset potential is called overpotential. It linearly increases with increasing current in proportion to the internal resistance of the cell. If on the other hand current flows spontaneously between WE and CE, one speaks of a galvanic element. With increasing current the potential hence decreases in proportion to the internal resistance [20, 21].

The described charge transfers across the EEI are governed by Faraday's first law and are therefore called Faradaic processes. The transferred charge by electrons in the electrode equals the charge transferred by ions in the electrolyte. The overall exchanged charge Q can thus be calculated by $Q = I\ t$, with the current I and time t. The charge of 1 mol of transferred ions with a monovalent charge e_0 is given as the Faraday constant $F = N_A\ e_0$ with the Avogadro constant N_A. The transferred charge to form a product with mass m and molar mass M is therefore calculated by [20, 21]

$$Q = \frac{m\ n}{M\ F}\,. \tag{2.4}$$

Electrical double layer

In contrast to Faradaic processes, non-Faradaic processes occur at the EEI without charge transfer. Still, they can be accountable for external current flow or potential changes. Adsorption and desorption are examples for such processes, but also the formation of the Electrical Double Layer (EDL). If a metal electrode gets into contact with a solution of the respective metal ions, the redox reaction $\mathrm{Me}^{n+} + n\,\mathrm{e}^- \rightleftharpoons \mathrm{Me}$ takes place. Assuming the forward reaction predominates, the electrode surface will be locally scarce of electrons. Hence, this positive surface charge attracts anions of the same amount of charge. Applying an external potential, this charge can be increased, decreased or even reversed in its sign. The EDL can consequently act as a capacitor [20, 21].

The solution side of the EDL can be described by various models, which assume the EDL consists of one or multiple layers. The simplest EDL model is the rigid Helmholtz layer. Solvated excess ions form the Outer Helmholtz Plane (OHP) with distance $\frac{a}{2}$ to the electrode which corresponds to half of the radius of the solvated ion. Interpreting the EDL as a capacitor, this is comparable with a plate distance of $\frac{a}{2}$. In larger distance to the electrode a three-dimensional region called the diffuse layer extends from the OHP to the bulk of the solution. For electrolyte concentrations greater than $10^{-2}\,\mathrm{mM}$, this layer's thickness is up to ca. 100 Å. The potential as a function of distance to a positively charged electrode is depicted in figure 2.1. If van-der-Waals interactions of so called specifically adsorbed anions or Coulomb interactions between solutes and surface electrons are considered, the rigid EDL layer is extended by an Inner Helmholtz Plane (IHP) [20, 21].

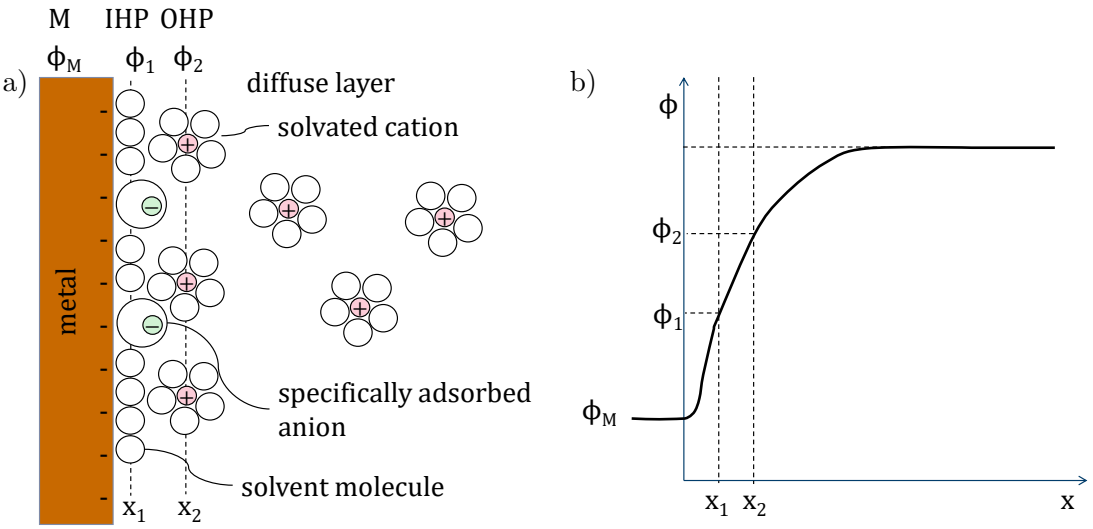

Figure 2.1: (a) Illustration of the EDL with IHP, OHP, specifically adsorbs anions and solvated cations; (b) Potential curve over the different regions of the EDL.

2.1.2 Electrochemical measurements

To control the electrochemical conditions at the WE of an electrochemical cell, a device is necessary that regulates potential and current. The potentiostat, depicted in figure 2.2, measures the current between WE and CE as potential drop over an internal resistance as well as the voltage between WE and RE by a high-impedance loop. A function generator specifies a control potential $E_{controlled}$ that is compared to the measured potential $E_{measured}$. This potential difference is then regulated to a minimum by a control circuit adjusting the current through the cell [20, 21].

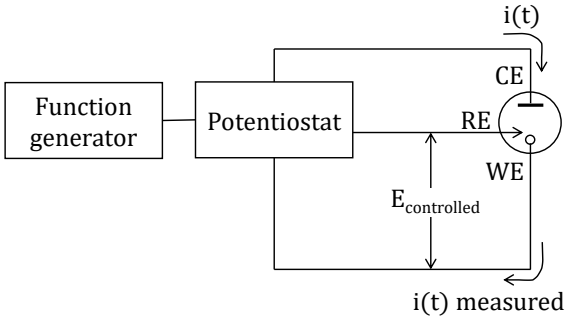

Figure 2.2: Schematic of a potentiostat controlling the electrochemical conditions in a electrochemical cell with a three-electrode setup.

Potentiostatic and galvanostatic measurements

In a potentiostatic experiment, the current is recorded as result of a potential step. Such measurements are also called Chronoamperometry (CA) and the evolution of potential, current and local concentration over time are depicted in figure 2.3.a. Assuming a sudden increase at $t = 0$ from a potential E_1, at which only non-Faradaic processes occur, to a potential E_2 that activates a chemical reaction, the concentration of the reactant drops to nearly zero at the EEI. In an unstirred solution, the reaction rate is mass transfer limited and governed by diffusion of the reactant towards the WE. The Faradaic current is at maximum at $t = 0$ due to the initial reaction of the educt at the WE. The subsequent reaction rate depends on the resulting concentration gradient and is decreasing over time, which leads to an exponentially decreasing current towards a constant value. The current is constant once the diffusion layer is fully established.

In a galvanostatic experiment, a step in control current results in the potential curve displayed in 2.3.b. These measurements are also called Chronopotentiometry (CP). The constant current leads to a constant reduction rate, while the potential needed to ensure the constant conversion rate constantly increases with decreasing surface concentration of the reactant. When due to mass transfer limitations, the concentration drops to zero, the potential increases dramatically until another reaction takes place that requires a higher overpotential. The time passed until this transition in potential is called transition time τ [20, 21].

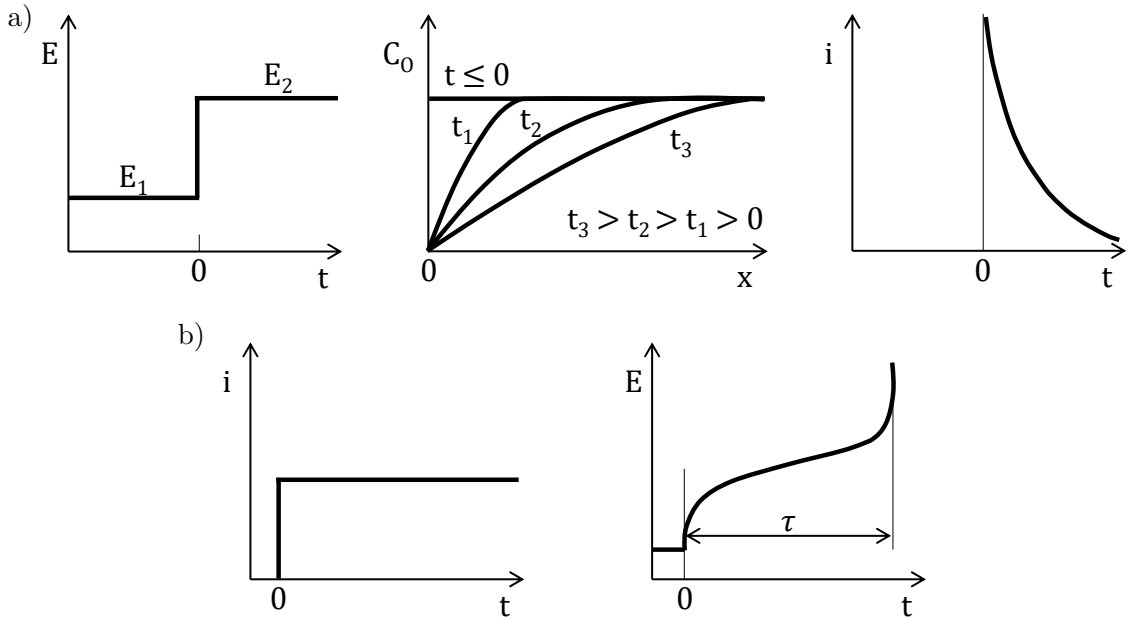

Figure 2.3: (a) Evolution of potential E, spatial concentration profiles C with distance to electrode x and current density i during CA. C_0 represents the initial concentration at $t = 0$. (b) Evolution of current density i and potential E during CP. τ represents the transition time.

Potential sweep methods

If potentiostatic experiments with various step potentials E_2 are performed, the time dependent current curves can be represented by an i-t-E surface, cf. figure 2.4. Particularly in the case of species that react at similar potentials, closely spaced potential steps are time-consuming. If the potential is linearly swept however, a single experiment could provide information more time-efficiently. In the three-dimensional i-t-E surface, this experiment is represented by a plane described by the linear function

$$E(t) = E_1 + vt\,, \tag{2.5}$$

with scan rate v. The current response corresponds to the intersection between i-t-E surface and this plane, which illustrates the influence of the scan rate. A steeper linear function $E(t)$ would compress the temporal response of the current, but could also result in a shift of the t-E characteristics. If the potential is modulated as described, the experiment is called Linear Sweep Voltammetry (LSV). If the potential change is reversed after reaching E_2 and cycled several times, it is denominated as Cyclovoltammetry (CV). This technique enables a quick initial study of electrochemical reaction systems taking place on the WE. An additional advantage of this technique is that cycling the cell's potential multiple times will remove adsorbed impurities by reduction or oxidation that would otherwise block

active sites [20, 21].

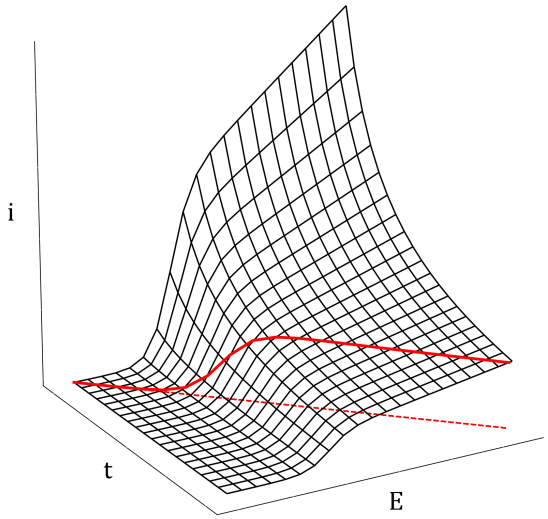

Figure 2.4: An exemplary *i*-*t*-*E* surface, illustrating the dynamics of potential sweep measurements. A linear sweep across this surface is depicted as red line and corresponds to the projection of the linear sweep function in the *t*-*E* plane on the *i*-*t*-*E* surface.

2.2 Electrochemical CO_2 reduction

2.2.1 CO_2 reduction reactions towards liquid fuels

Research on eCO_2R has accelerated over the past 15 years with exponentially increasing numbers of publications [22]. The first proof that electrochemical reduction of CO_2 is possible goes back to 1954, where CV curves were investigated under N_2 and CO_2 saturation at large area mercury electrodes [23]. The pioneering work of Hori *et al.*, who first accounted for 100% Faradaic Efficiency (FE) by analysing both gaseous and liquid products, followed 30 years later [11]. With their subsequent work [24–28], they were able to classify metal electrodes into groups regarding their primary product of eCO_2R. Pb, Hg, Tl, In, Sn, Cd and Bi catalyse formate formation; Au, Ag, Zn, Pd and Ga catalyse CO formation; Ni, Fe, Pt and Ti reduce water instead of CO_2 and finally, Cu has the unique ability to catalyse a variety of hydrocarbons [11, 29]. This variation in product selectivity is a result of varying binding energies for the key intermediates *H, *OCHO, *COOH and *CO. Comparing the binding energies to *CO with the binding energies to *H of the various metal elements, this classification in four groups gets evident. The water reducing metals exhibit negative binding energies to both *H and *CO. Formate and CO forming metals show a positive binding energy to *CO and *H, while the binding energy to *H is higher for the formate catalysing metals. Cu in contrast is the only metal with positive binding energy to *H but negative to *CO [30], which explains its unique catalytic activity.

Building on the fundamental work on Cu-catalysed eCO_2R [27], Kuhl *et al.* detected a total of 16 products from eCO_2R at a polycrystalline Cu WE making use of more sensitive analysis methods [31]. Among these products were not only gaseous products such as CO, methane or ethylene, but also products in the liquid phase such as formate, ethanol, methanol, acetate and even n-propanol. Potentiostatic experiments at potentials in the range of -0.6 to $-1.2\,\mathrm{V}$ *vs.* RHE showed how the product selectivity was potential dependent. Thus, FE of CO and formate formation peaked at -0.8 to $-0.9\,\mathrm{V}$ *vs.* RHE, while ethylene FE plateaus at ca. $-1.0\,\mathrm{V}$ *vs.* RHE, which is in accordance with findings of the Hori group. The reaction equilibria in equation 2.6 to 2.12 show how many electrons are necessary to form the respective product, ranging from two electrons for CO and formate up to 18 for n-propanol [11, 29].

$$CO_2 + 2\,H^+ + 2\,e^- \longrightarrow HCOOH \tag{2.6}$$

$$CO_2 + 2\,H^+ + 2\,e^- \longrightarrow CO + H_2O \tag{2.7}$$

$$CO_2 + 6\,H^+ + 6\,e^- \longrightarrow CH_3OH + H_2O \tag{2.8}$$

$$CO_2 + 8\,H^+ + 8\,e^- \longrightarrow CH_4 + 2\,H_2O \tag{2.9}$$

$$2\,CO_2 + 8\,H^+ + 8\,e^- \longrightarrow CH_3COOH + 2\,H_2O \tag{2.10}$$

$$2\,CO_2 + 12\,H^+ + 12\,e^- \longrightarrow C_2H_5OH + 3\,H_2O \tag{2.11}$$

$$3\,CO_2 + 18\,H^+ + 18\,e^- \longrightarrow C_3H_7OH + 5\,H_2O \tag{2.12}$$

2.2.2 Reactions of CO_2 in aqueous solution

To understand the eCO_2R in aqueous media, the reactions of CO_2 in water have to be understood first. The dissolution of gaseous CO_2 in water can be described by the Henry correlation,

$$a(CO_2(aq)) = H \cdot p(CO_2)\,, \tag{2.13}$$

with the activity $a(CO_2(aq))$ of dissolved CO_2 , the partial pressure $p(CO_2)$ of gaseous CO_2 and the Henry constant $H = 33.8\ \frac{\text{mmol}}{\text{L·atm}}$ [29] at 25 °C, meaning that the solubility of CO_2 in water at standard conditions equals 33.8 mM. The Henry constant is furthermore a function of temperature. With decreasing temperature, the solubility generally increases. *E.g.* at 10 °C and atmospheric pressure, the solubility of CO_2 in water increases to 53.3 mM [32].

Dissolved CO_2 reacts via two reversible reaction pathways to carbonic acid and bicarbonate,

$$CO_2(aq) + H_2O \underset{k_{-1}}{\overset{k_1}{\rightleftharpoons}} H_2CO_3\,, \tag{2.14}$$

$$CO_2(aq) + OH^- \underset{k_{-2}}{\overset{k_2}{\rightleftharpoons}} HCO_3{}^-\,. \tag{2.15}$$

Three further protonation reactions are important for the CO_2 chemistry in water, *i.e.* the equilibrium between bicarbonate and carbonate,

$$CO_3{}^{2-} + H^+ \overset{K_{a1}}{\rightleftharpoons} HCO_3{}^-\,, \tag{2.16}$$

the equilibrium between carbonic acid and bicarbonate,

$$HCO_3{}^- + H^+ \overset{K_{a2}}{\rightleftharpoons} H_2CO_3\,, \tag{2.17}$$

and the protonation of hydroxide to water,

$$OH^- + H^+ \overset{K_w}{\rightleftharpoons} H_2O\,. \tag{2.18}$$

An overview about these reactions is given in figure 2.5. As reactions 2.16, 2.17 and 2.18 are considered instantaneous, only the equilibrium constants are given here. Due to the fast reaction of carbonic acid to bicarbonate, the concentration of carbonic acid is usually negligible [33]. The reaction equilibrium and their corresponding pK_a values can therefore be summarised as [29]

$$CO_3{}^{2-} + H^+ \rightleftharpoons HCO_3{}^-\,, \quad pK_{a1} = 10.3\,, \tag{2.19}$$

$$HCO_3{}^- + H^+ \rightleftharpoons CO_2(aq) + H_2O\,, \quad pK_{a2} = 6.4\,. \tag{2.20}$$

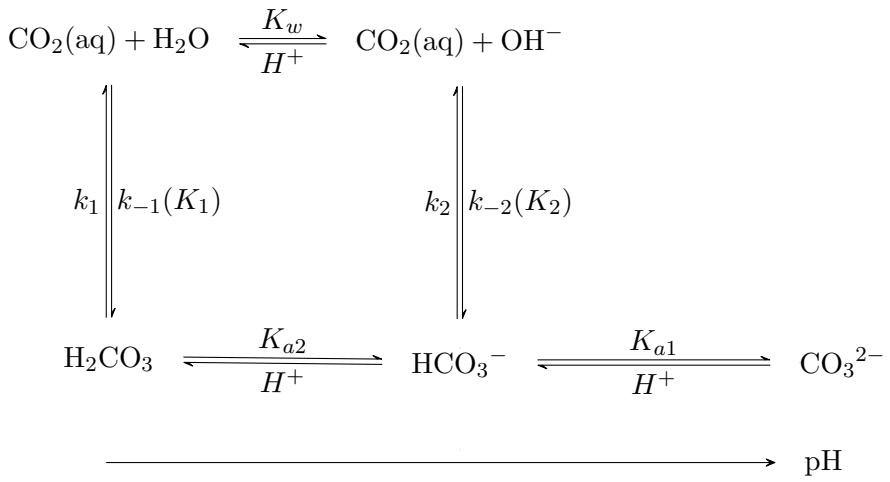

Figure 2.5: Reaction scheme of CO_2 chemistry in water.

According to the pK_a values, the CO_2/HCO_3^- equilibrium is dominant between pH values of ca. 4.3 to 8.2, while the HCO_3^-/CO_3^{2-} equilibrium is dominant between values of ca. 8.2 and 12.4 [34].

2.2.3 Electrolyte effects

As HCO_3^- is naturally in equilibirum with CO_2 in aqueous solution, it is evident that bicarbonate solutions are important electrolytes in eCO_2R. Such electrolytes serve as pH buffer for near neutral pH and can act as proton donors in the reaction mechanisms of eCO_2R. Dunwell *et al.* attributed an even more important role to bicarbonate in eCO_2R [35]. By isotope labelling and surface-enhanced Raman spectroscopy, it was proven that the primary source of eCO_2R products in an H-type cell was indeed from CO_2 from the equilibrium with HCO_3^- rather than from directly supplied gaseous CO_2.

Besides the choice of anion in the eCO_2R system, the most frequently discussed electrolyte parameters in literature were the influence of local pH at the electrode, the impact of cation size, and mass transport effects [36–38]. The local pH effect arises from the continuous consumption of H^+ at the WE, either due to eCO_2R or HER. This local pH increase affects the eCO_2R mainly in two ways. On the one hand, the solubility of CO_2 is greatly influenced, cf. equations 2.19 and 2.20 [34]. On the other hand, the reaction thermodynamics are influenced depending on whether the Rate Determining Step (RDS) in a reaction pathway is pH dependent or not. Also, the competitive HER depends on pH and can therefore be suppressed under highly alkaline local conditions. In general, increasing local pH favours the formation of C_{2+} products [36, 39–41]. Thus, not the bulk pH but the pH in electrode proximity determines the Cu-catalysed product distribution [40], and controlling the interfacial pH as well as the pH gradient in the electrolyte by engineering of the EEI is crucial in order to tailor the selectivity for desired products [12, 19, 38].

The role of metal cations was recently highlighted by the Koper group, who showed

that in the absence of metal cations, the eCO_2R was suppressed completely [42]. Until then, it was assumed that only the reaction rate was affected by the cation size [36]. A generally increased selectivity for C_{2+} products with increasing cation size was explained by electric field effects or the buffering effect of cation hydrolysis [36, 43–46]. But the findings of Monteiro *et al.* implied that partially desolvated cations stabilising the CO_2 intermediates are the most important mechanism [36, 47].

Lastly, the local reaction conditions, especially in terms of pH and reactant concentration, are also influenced by the mass transport conditions in the electrochemical cell [37]. Gupta *et al.* showed how these properties can differ locally during eCO_2R by calculating concentration gradients of H^+ and CO_2. Assuming various operating points of current density and diffusion layer thickness, it was shown that the surface pH can differ from the bulk pH by ca. 1.5 for strongly buffered 2 M $KHCO_3$ solution up to a difference of ca. 6 pH units for weakly buffered 0.05 M $KHCO_3$ solution [39]. Not only the local pH, but also the rate of the competing HER itself can be tuned by controlling the mass transport. By manipulating convection at a rotating disk electrode, it was shown that the FE could be adjusted towards eCO_2R [48]. Mass transport becomes especially important when engineering porous electrode materials such as Gas Diffusion Electrodes (GDEs). It is governed by diffusion in confined volumes, where the reaction conditions will strongly differ from the bulk electrolyte [37]. Also, the conditions in a batch cell will vary widely from conditions in a flow cell setup, and from laboratory scale to industrially relevant current densities. Therefore, research will have to focus on testing the catalytic EEI under more realistic operating condition to take the next step of eCO_2R development towards industrial application [49].

2.3 Magnetic Resonance

2.3.1 Fundamentals

Apart from mass, electric charge and nuclear magnetism, nuclei have a fourth intrinsic physical property, the so called spin. Even though it has no impact on the chemical and physical properties of a substance on a macroscopic level, its interaction with electromagnetic fields can give insight into the internal structure and chemical environment of a sample. The interactions of a spin with an external magnetic field are equivalent to those of a magnetic nucleus rotating about its own axis and result in an angular momentum. According to quantum mechanics, this angular momentum L is quantised by,

$$L = [S(S+1)]^{\frac{1}{2}}\,\hbar\,, \tag{2.21}$$

with the spin quantum number S and the reduced Planck's constant $\hbar = 1.054 \cdot 10^{-34}$Js. Protons and neutrons both have a spin S of $1/2$. Since all elemental nuclei consist of varying compositions of protons and neutrons, every isotope of an element exhibits individual ground-state spin S. A selection of important isotopes is listed in table 2.1 [50].

Isotope	Ground-state spin	Natural abundance/%	Gyromagnetic ratio $\gamma/10^6\,\mathrm{rad\,s^{-1}\,T^{-1}}$	Larmor frequency at 14.1 T $(\omega_0/2\pi)$/MHz
^{1}H	1/2	∼100	267.522	-600.000
^{2}H	1	0.015	41.066	-92.104
^{13}C	1/2	1.1	67.283	-150.870
^{19}F	1/2	∼100	251.815	-564.564
^{23}Na	3/2	100	70.808	-158.711

Table 2.1: Ground-state spin, natural abundance, gyromagnetic ratio and NMR frequency at 14.1 T of important isotopes.

When the nucleus is experiencing a magnetic field, the nuclear spin levels split according to the nuclear Zeeman splitting into $(2S+1)$ sublevels, cf. figure 2.6. The energy difference of these sublevels can be experimentally determined and is the fundamental prerequisite of NMR spectroscopy. Electromagnetic fields can deliver the energy needed to excite the spin from a low to a high energetic sublevel. For nuclei, typical frequencies are on the order of 10^8 Hz, which is in the range of Radio Frequency (RF) waves. The exact frequency, at which a specific nucleus is excited, is called the Larmor frequency ω_0,

$$\omega_0 = -\gamma \cdot B_0\,, \tag{2.22}$$

where B_0 is the strength of the permanent magnetic field and γ is the gyromagnetic ratio, which is the proportionality constant between ω_0 and B_0. Important values for γ and corresponding Larmor frequencies are given in table 2.1. The Larmor frequency furthermore corresponds to the frequency of the precession movement spins carry out when experiencing a magnetic field B_0 [50, 51].

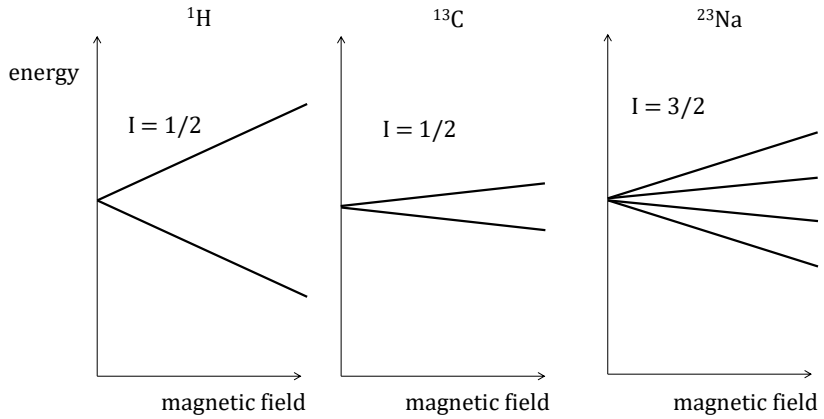

Figure 2.6: Zeeman splitting of ^{1}H, ^{13}C and ^{23}Na.

Chemical shift and rotating frame

A single spin cannot be thought of as a small bar magnet or a magnetic moment that points in one direction and is aligned with external magnetic fields. Quantum mechanical view on spins prohibits that. But in NMR experiments, a large number of nuclei is usually observed, *i.e.* on the order of 10^{20} spins. Thus, the net effect of all nuclei in the sample is detected. If a sample is exposed to an external magnetic field, the direction of the magnetic moment of a single spin cannot be determined, because its interaction with the macroscopic field is too weak to be detected individually and to be distinguished from the rest of a macroscopic sample. But it turns out that at thermal equilibrium, the overall magnetic moment of the whole sample is aligned with the magnetic field B_0. This is called the bulk magnetisation of the sample and can be represented by a classical magnetisation vector, depicted in figure 2.7. External RF fields are capable of tilting the magnetisation vector by an angle β

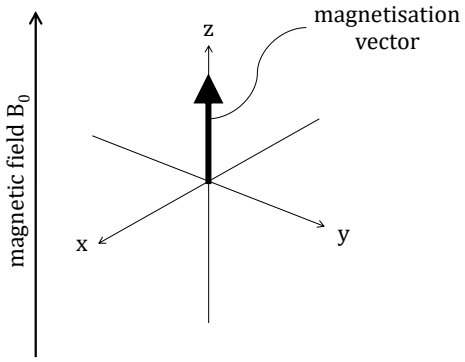

Figure 2.7: Bulk magnetisation vector aligned along magnetic field in longitudinal z-direction. x- and y-axis represent transversal directions.

from its equilibrium position. To manipulate the bulk magnetisation accordingly, external RF fields are applied by RF coils surrounding the sample. The transmitter frequency has to be resonant with the Larmor frequency, $\omega_{\mathrm{RF}} = \omega_0$. As a result, the vector is tilted away from its equilibrium and consequently precesses about the magnetic field direction z with the Larmor frequency. This precession is also the observable in NMR experiments. The RF coil detects any magnetisation in the xy-plane. The evolution of this signal as the magnetisation vector returns to its equilibrium position is called Free Induction Decay (FID) [51].

So far, only isolated nuclei without interactions with their chemical environment were considered. In fact, the Larmor frequency of a nucleus is largely influenced by nuclei and electrons in their environment. These impact the local magnetic field that the nucleus is experiencing, which can be interpreted as shielding of the nucleus. It can be described by

$$\omega = \omega_0 \cdot (1 - \sigma)\,, \tag{2.23}$$

with the shielding constant σ. This effect is useful to determine the chemical environment of nuclei, thus elucidating molecule structures and interactions between molecules. By convention, the resonance frequency of a nucleus is given relative to the resonance frequency of a reference compound ω_{ref}. This simplifies the discussion about frequency differences that are relatively small compared to the spectrometer frequency and makes it independent of the magnetic field. The so called chemical shift δ is therefore

$$\delta = \frac{\omega - \omega_{\mathrm{ref}}}{\omega_{\mathrm{ref}}}\,, \tag{2.24}$$

and is usually given in units of parts per million (ppm) [50, 51].

To simplify the rotating movement of precession, the concept of the rotating frame is introduced. The coordinate system in figure 2.7 rotates with the transmitter frequency ω_{RF}, which results in a static B_1. The difference to the Larmor frequency is called offset frequency Ω,

$$\Omega = \omega - \omega_{\mathrm{RF}}\,. \tag{2.25}$$

If ω_{RF} is also on resonance, *i.e.* $\omega_{\mathrm{RF}} = \omega$, the flip angle β, about which the magnetisation is tilted away from the z-axis, is given by

$$\beta = \omega_1 \cdot t_p\,, \tag{2.26}$$

with the duration of the RF pulse t_p and the nutation frequency ω_1 [51].

Relaxation

Relaxation describes processes, by which spins come to thermal equilibrium with their environment. When transverse magnetisation has been created by applying an RF pulse, the FID will show a decay of amplitude over time. This loss of transverse magnetisation

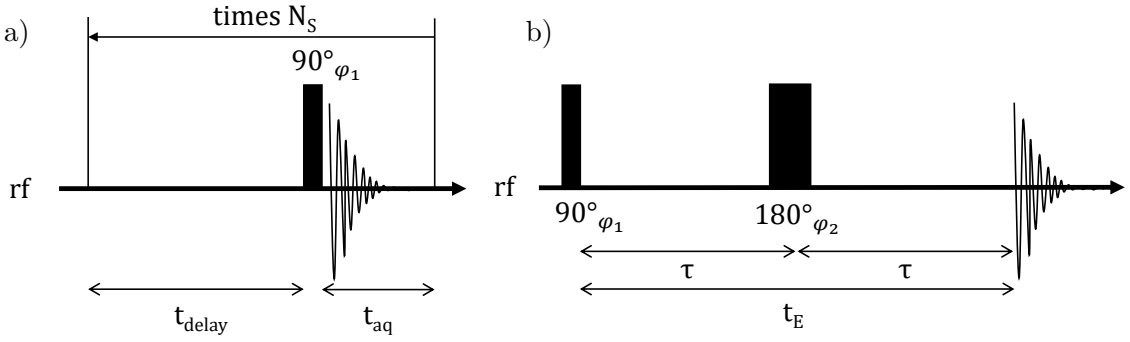

Figure 2.8: (a) Standard 90° pulse experiment and (b) spin echo experiment.

M_{xy} is called transverse relaxation and is characterised by the exponential time constant T_2,

$$|M_{xy}(t)| = |M_{xy,0}| \cdot e^{-t/T_2}\,, \tag{2.27}$$

with the initial transverse magnetisation $M_{xy,0}$. Once the magnetisation is tilted away from the z-direction, it will also return to its equilibrium state with regard to its z-magnetisation. The reestablishment of the magnetisation in z-direction M_z is called longitudinal relaxation with the exponential time constant T_1,

$$|M_z(t)| = |M_{z,0}| \cdot \left(1 - e^{-t/T_1}\right)\,, \tag{2.28}$$

with the equilibrium z-magnetisation $M_{z,0}$. Equation 2.28 is valid for a saturated spin system, *i.e.* $M_z(0) = 0$ at time $t = 0$.

NMR experiments

NMR experiments consist of three elemental parts, *i.e.* an equilibration period in order to generate z-magnetisation, generation of transverse magnetisation by application of an RF pulse and acquisition of the FID. In the simplest cast, *i.e.* the 90° experiment, the length and power of the RF pulse are chosen such that the flip angle β is 90°, which is illustrated in figure 2.8.a. This results in the maximum transverse magnetisation and therefore maximum integral of the FID. The acquisition should last until the FID is fully attenuated. Afterwards a delay time t_{delay} is integrated into the pulse sequence for the longitudinal relaxation of the magnetisation, before another 90° pulse again generates transverse magnetisation and the acquired signal is added to the previous one. This sequence is repeated N_S times until the desired signal to noise ratio is obtained. The repetition time t_r is composed of the delay time t_{delay} and the acquisition time t_{aq}.

If after the 90° pulse a 180° pulse is applied, a so called spin echo is observed after the echo time $t_E = 2\tau$, cf. figure 2.8.b. In the rotating frame, the magnetisation vector evolves a phase shift with Ωt, as depicted in figure 2.9. The 180° pulse is applied after $t = \tau$ and flips the magnetisation over one of the transversal axes. Now, the phase evolves further, so

that after $t = 2\tau$, it is exactly refocused. Therefore, the 180° pulse is also called refocusing pulse [52]. The refocusing of phase evolution is of special interest if the real transversal

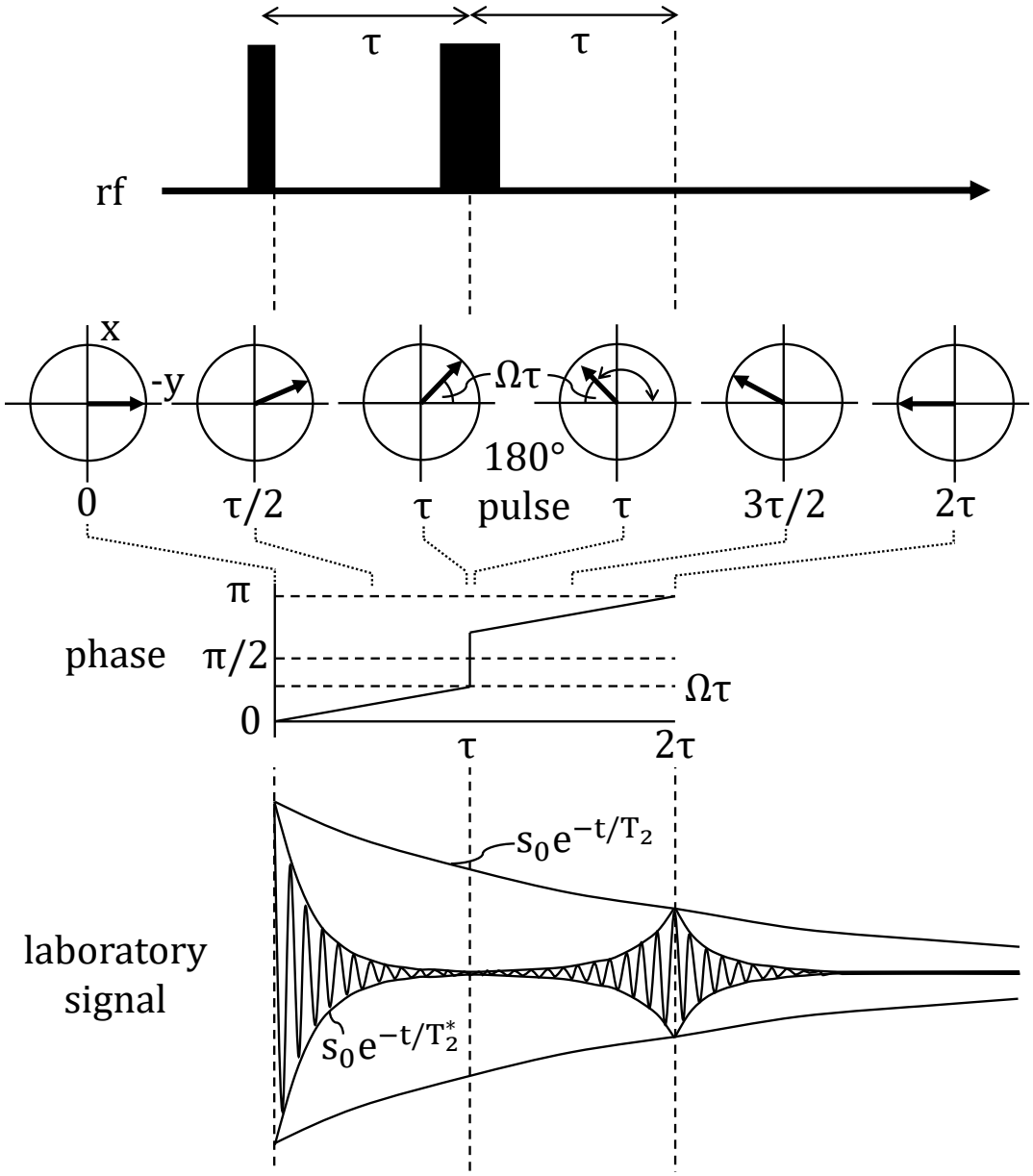

Figure 2.9: Evolution of phase during spin echo experiment. The decay of NMR signal s_0 with T_2 and T_2^* relaxation time is depicted in the lower panel.

relaxation time T_2 is to be determined. Due to magnetic field inhomogeneities, additional dephasing of transversal magnetisation occurs with time constant T_2'. The time constant by which the NMR signal of a 90° experiment decays is denoted as T_2^* and the relation with T_2 and T_2' is

$$\frac{1}{T_2^*} = \frac{1}{T_2} + \frac{1}{T_2'}\,. \tag{2.29}$$

Consequently, T_2 can be determined by using spin echo experiments, as depicted in figure 2.9.b. By applying several refocusing pulses, also called an echo train, the intensity of the echo signals decays with time constant T_2 [52].

2.3.2 Imaging techniques

An inhomogeneous magnetic field can be employed to advantage. Supposing an object is placed in a magnetic field B_0 along the z-direction that varies linearly with respect to the same axis, the top of the object experiences a slightly stronger magnetic field B_z than the middle or the bottom of the object,

$$B_z(z) = B_0 + z \cdot G_z \,, \tag{2.30}$$

with the magnetic field gradient $G_z = \partial B_z / \partial z$. This means that spins in the top exhibit a high-frequency Larmor precession $\omega(z)$, while spins at the bottom develop a lower Larmor frequency,

$$\omega(z) = \omega_0 - z \cdot \gamma G_z \,. \tag{2.31}$$

Their resonance would appear at a higher frequency in an NMR spectrum acquired during an applied magnetic field gradient. Thus, the NMR spectrum displays the spin density distribution along the axis of the magnetic field gradient. As the information about the z-position of a spin is comprised in their spatially dependent Larmor-frequency, this method is referred to as frequency-encoding. NMR techniques including magnetic field gradients are called MRI, which is well-known for its importance in medical applications. Typical gradient strengths for human-scale MRI are $\sim$10 mT/m, while for microimaging purposes gradients are on the order of 1 T/m. [50, 52].

The Fourier transform of the signal acquired while the linear magnetic field gradient is turned on corresponds to the z-dependent image space. The inverse transform of the image space is the data space, also called k-space. In the case of frequency encoding, the acquired signal is thus equivalent to the k-space. In imaging experiments, the parameter of the experiments have to be chosen such that the coverage of k-space corresponds to the desired Field of View (FOV) and resolution in the image dimension. The length of FOV in z-direction is the inverse of the resolution in k-space Δk_z. The correlation between resolution in k-space and time resolution of the acquired signal, the so called dwell time t_d is set by the gradient strength,

$$\Delta k_z = \gamma \; G_z \; t_d \,. \tag{2.32}$$

Furthermore, the spatial resolution Δz is determined by the range of k-space data, which corresponds to the bandwidth of the transmitter BW. As the dwell time t_d is the inverse

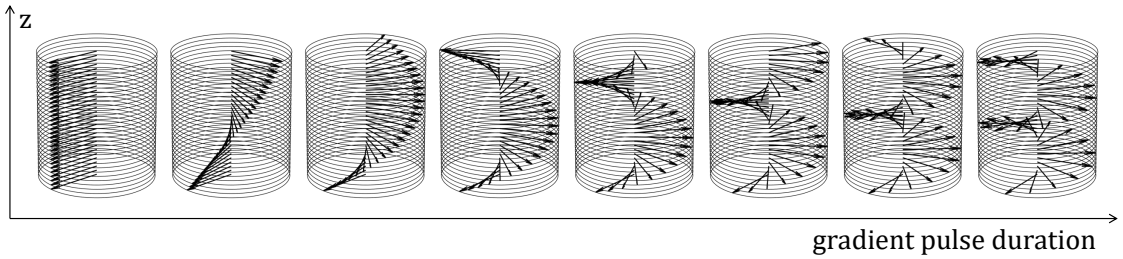

Figure 2.10: Evolution of spatially dependent phase shift during application of magnetic field gradient pulses of varying duration.

of the bandwidth BW, the required gradient strength for a given FOV and BW is [52]

$$G_z = \frac{BW}{FOV\ \gamma}\,. \tag{2.33}$$

The Fourier transform of frequency encoded signals are typically plotted in magnitude mode as chemical shift information is lost when gradients are applied during detection. In contrast, purely phase encoded techniques do not require application of gradients during acquisition and will, therefore, maintain the chemical shift information. Here, magnetic field gradient pulses are applied in a way that transverse magnetisation develops a phase shift along the gradient axis, *e.g.* the z-direction. When the gradient is shut off, the sample has a spatially dependent phase shift that defines the position of all spins on the z-axis. The spatial distribution of phase depends on the gradient strength and pulse duration, which is depicted in figure 2.10. Each of these phase distributions can be described by a spatial wave function that directly corresponds to one point in k-space given by,

$$k_z = \gamma \cdot G_z \cdot t_g\,, \tag{2.34}$$

with the gradient pulse duration t_g. Usually, the gradient strength is consecutively incremented to record a multitude of points in k-space with a constant interval Δk_z, which correlates to the inverse of the spatial FOV. With the number of points acquired in k-space N_p, the span of k-space values k_{span} can be calculated, which is inversely proportional to the spatial resolution Δz

$$k_{span} = k_{max} - k_{min} = \Delta k_z \cdot (N_p - 1)\,, \tag{2.35}$$

with the maximum and minimum values of k-space k_{max} and k_{min}, respectively [52].

As the frequency is not utilised for spatial encoding, it still holds the spectroscopic chemical shift information. Thus, purely phase encoded MRI pulse sequences enable the so called CSI. Here, an NMR spectrum can be assigned to every point along the spatial axis, as the transverse magnetisation is allowed to evolve and is fully recorded after each phase encoding step. In medical applications, this is of special interest, since it provides separated images of water, fat or lactate distribution in the body [52].

2.3.3 *In operando* NMR on electrochemical cells

Combining magnetic resonance techniques with electrochemical cells benefits from the unique spectroscopic information that can be obtained by NMR about species involved in electrochemical reactions. Electron transfer usually causes changes in redox state or molecular composition, which in turn induces changes in the magnetic resonances. However, the development of electrochemical cells operating in an NMR spectrometer, also called *in operando* NMR, is hampered by various issues. The prerequisite for all *in operando* NMR experiments is that essential components of the cell and the experimental setup, *i.e.* electronics, wires, electrodes, have to be suitable for operation at high magnetic field of several Tesla. Furthermore, electron conducting materials, usually metals, are inherently needed for electrochemical experiments [53].

To address the problems associated with introducing conductive material into the spectrometer, several measures have to be taken. First of all, if the sample is surrounded by a conductive metal, RF excitation is shielded from the sample depending on thickness and conductivity of the metal. This can be prevented by placing the metal in the centre of the sensitive NMR volume. However, there are still two main types of distortions that cannot be entirely inhibited even by a well conceived cell design. On the one hand, magnetic susceptibility differences between metal and surrounding materials cause inhomogeneities in the magnetic field B_0. On the other hand, eddy currents are induced in metals of high conductivity, which in turn modulate the strength of the RF field B_1 causing a loss in quantitativity [54].

Despite these challenges, several approaches of *in operando* NMR cells were presented over the past ∼50 years [53]. The first *in operando* NMR cell was presented by Richard *et al.* in 1975 [55]. Inside a standard 5 mm NMR tube, wires were placed outside the sensitive NMR volume serving as electrodes. The electrolyte was continuously pumped through the sensitive volume and the whole sample was rotating to improve magnetic field homogeneity and solvent mixing. More than 40 years later, this cell concept with wire electrodes places outside the NMR volume was adapted. Sample rotation was not required anymore, as the NMR hardware improved significantly over the years in terms of sensitivity and homogenisation of B_0 field. Also the mixing by external pumping was excluded, as the effect of magnetohydrodynamic (MHD) forces was utilised [56]. The MHD effect arises from the Lorentz force acting on ions in solution resulting in a convective flow that acts as an internal mixer in *in operando* NMR cells [57].

Several other types of cells with a wide variety of electrode designs were presented, such as thin film electrodes placed in the sensitive volume [58], wire electrodes placed above and under the sensitive volume [59], or carbon fibre electrodes with reduced conductivity and inert surface placed inside [60] or outside the sensitive volume [61]. Based on these cell designs employing micro-electrodes in a standard NMR tube, Jovanovic *et al.* developed the only *in operando* NMR cell for the investigation of eCO_2R to the author's knowledge. The special feature in this setup was the placement of a highly conductive Ag WE in

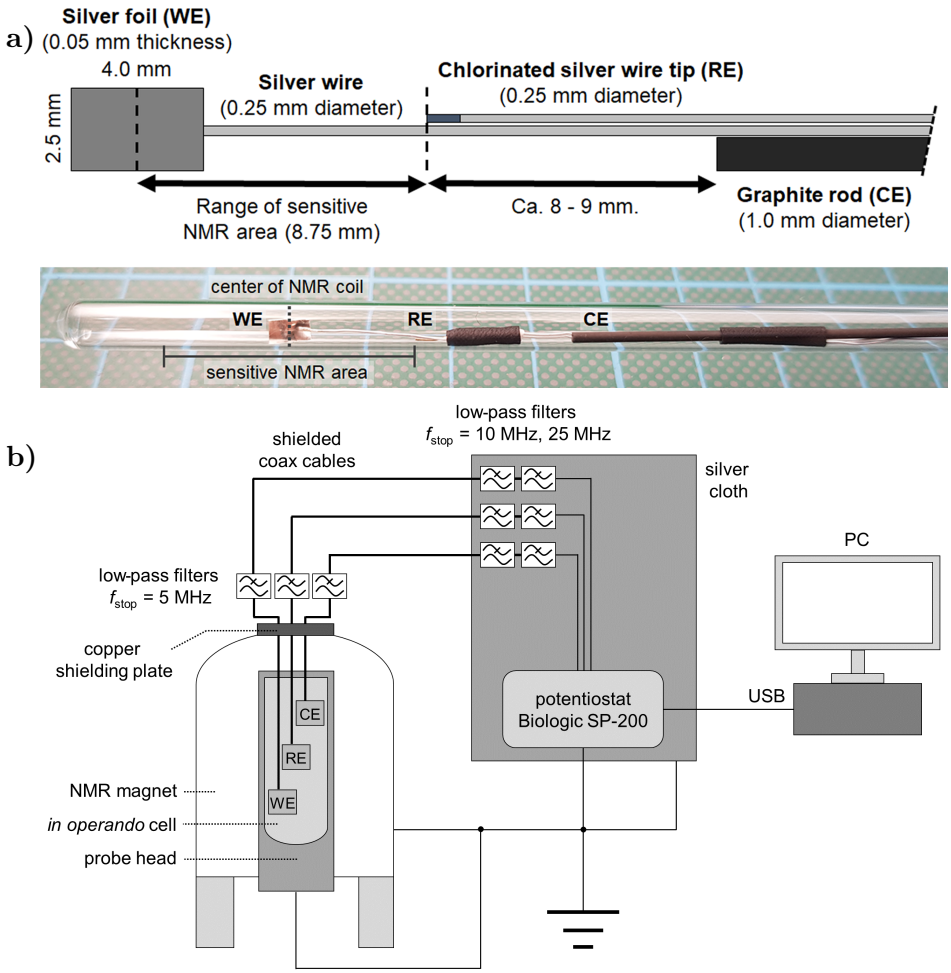

Figure 2.11: Cell design (a) and experimental setup (b) of *in operando* NMR experiments by Jovanovic *et al.* [62]. Figures are reproduced from the open access publication.

the centre of the sensitive NMR volume, as it is depicted in figure 2.11.a. The resulting distortions of the NMR signal and the additional environmental noise could be minimised by the well-conceived experimental setup that included low-pass filters, as well as thorough shielding and grounding, *cf.* figure 2.11.b.

More advanced electrode designs, such as an Membrane Electrode Assembly (MEA), were applied inside a toroidal cavity detector that served as NMR probe and CE. Another remarkable cell design is a 3D printed cell with tailored RF coil shape by cured liquid metals in 3D printed cavities [63]. Besides purely spectroscopic investigations, Britton *et al.* visualised concentration changes during electrochemical reactions at flat Zn electrodes. Placing these metal strips parallel to the applied RF field, the distortions due to eddy currents could be minimised [64].

A large number of *in operando* NMR studies were in the field of battery research [65]. As the redox reactions of important ions for battery applications such as Li^+ and Na^+ involve NMR-active nuclei, *i.e.* $^6Li/^7Li$ or ^{23}Na [66], various battery cells for *in operando* NMR were developed, *e.g.* a bag cell [67, 68], a custom-made cylindrical cell from a

polyether ether ketone (PEEK) rod [69] or a coin cell in a Swagelok inspired container [70]. Also, multiple studies of battery cells applying MRI techniques were published, *e.g.* to investigate concentration profiles [71, 72] or detect Li dendrite formation [73]. Even 3D MRI of metallic Li using fast imaging sequences was demonstrated [74]. Recently, ^{23}Na MRI was in the focus of Na-ion battery research. The dynamics of dendrite formation was imaged by T_2 weighted ^{23}Na MRI [75] or by *in operando* ^{23}Na CSI and *in situ* ^{1}H MRI [76, 77].

Chapter 3

Quantifying local pH changes in carbonate electrolyte during copper-catalysed CO_2 electroreduction using *in operando* ^{13}C NMR

3.0 Preface

This chapter is based on the open access publication [78]

Quantifying local pH changes in carbonate electrolyte during copper-catalysed CO_2 electroreduction using *in operando* ^{13}C NMR,

by Michael Schatz (corresponding author), Sven Jovanovic, Rüdiger-A. Eichel and Josef Granwehr, published in *Scientific Reports*, Volume 12, Number 1 (2022).

3.1 Introduction

First *in operando* Nuclear Magnetic Resonance (NMR) techniques for the investigation of the electrochemical Carbon Dioxide Reduction (eCO_2R) have successfully been employed [62]. This chapter presents an *in operando* NMR method for local pH determination in the vicinity of flat Cu electrodes.

In recent years, the eCO_2R has been recognised as a possible industrially applicable contribution for establishing a closed carbon cycle [79]. Driven by intermittent renewable electricity, this process has the potential to produce carbon-neutral fuels and feedstock chemicals while simultaneously stabilising the electric grid by acting as energy store [12].

In addition to electrode surface characteristics and reaction conditions, the most influential factors for eCO_2R are properties of the aqueous solution surrounding the electrode, *i.e.* local pH and HCO_3^-/CO_2 concentration values [19, 80, 81]. How these local properties are affected by applied potential and how this in turn influences product formation has not been addressed experimentally owing to a lack of suitable *in operando* methods [22].

Among metal catalysts for eCO_2R, elemental copper has the unique ability to catalyse short-chain hydrocarbon evolution. In order to optimise future copper-based electrocatalyst designs, the understanding of underlying reaction mechanisms needs to be improved [27, 31]. The first publication about Cu-catalysed eCO_2R by Hori *et al.* [27] discussed the interdependence of hydrocarbon and alcohol formation on local changes of the $KHCO_3$ buffer. In dilute $KHCO_3$ solution, the pH in cathode proximity increases due to OH^- formation as part of the reduction reaction as well as poor buffer capacity of the solution. This in turn prevents the Hydrogen Evolution Reaction (HER) and promotes the reduction of CO_2. If a potential more negative than $-1.1\,\mathrm{V}$ *vs.* Normal Hydrogen Electrode (NHE) is applied, CO stays adsorbed at the cathode and can be further reduced to C_{2+} products, *e.g.* ethylene, ethanol or even n-propanol [27]. Gupta *et al.* presented calculations investigating the interplay between local pH, buffer capacity and current density. For a bulk pH of 6.81 and a current density of $10\,\mathrm{A/m^2}$, they determined a pH of up to 9 on the electrode surface. Due to the shifted HCO_3^-/CO_2 equilibrium and simultaneous reduction of CO_2 in electrode proximity, a decrease of the local CO_2 concentration by a factor of 2.1 was predicted [39]. However, a decrease in CO_2 concentration does not translate linearly to a decrease in conversion rate. It has been shown using ^{13}C labelling that the main source of converted carbon is CO_2 from the equilibrium with HCO_3^- [82]. This led to the conclusion that the effective concentration of CO_2 in electrode vicinity is equivalent to the bulk [83]. Nonetheless, local CO_2 scarcity and basic pH dictate the reaction conditions at the electrode and must be considered for understanding the reaction mechanism of eCO_2R on copper.

Local pH effects have proven important in shifting the selectivity to desired products. A high local pH can be advantageous for reaction pathways that include a rate determining step without a proton transfer. In this case, hydrogen formation is hindered while product formation is pH-independent. This applies *e.g.* to the C–C formation step in the reaction

pathway to ethylene and ethanol [84–86]. In contrast, the formation of products such as methane that include a proton transfer in the rate determining step are inhibited [19]. Local shifts in the concentrations of CO_2 and HCO_3^- also affect the product formation. At small negative overpotential and therefore only modest changes in local pH, formate is formed in the presence of adsorbed CO_3^{2-}. More negative potentials shift the equilibrium to solution-based bicarbonate and promote CO formation [35, 87].

The effects of local conditions have been utilised in electrode engineering. Roughened or porous electrode surfaces promote high local pH, which can effectively suppress HER [86] and simultaneously favour C_{2+} product formation by confinement of intermediate products [19, 85]. However, a study using a Cu nanofoam electrode showed increased formate production over the whole potential range, suppressing the pathways to methane and ethylene almost completely [88]. This contradiction shows how important it is to understand the complex interplay between electrolyte composition, applied potential and surface morphology for electrode engineering. In order to generate a micro-environment that is suitable for the desired product formation, all of these parameters have to be considered [89]. Burdyny *et al.* even suggest considering the catalyst as combined surface and electrolyte system rather than just a metal surface [49]. To understand the catalytic performance of such a surface/electrolyte system, it is indispensable to know how local pH evolves during operation, and how the CO_2 concentration and therefore the accessibility of the reactant varies locally.

Measuring local concentrations of protons and molecules that take part in electrochemical reactions has been attempted, for example, using scanning probe techniques and various optical methods [42]. Recent studies investigating eCO_2R apply scanning electrochemical microscopy (SECM) [90], surface-enhanced infrared absorption spectroscopy (SEIRAS) [44, 91] and surface-enhanced Raman spectroscopy (SERS) [92]. SECM offers direct measurement of the proton concentration by using the pH-sensitive electrochemical response of an inert metallic material. The SEIRAS and SERS methods measure the pH by monitoring the ratio of the species composing a buffer system and are, therefore, indirect measurement methods [42]. In these experiments, typical buffer solutions for eCO_2R such as $CO_2(aq)/HCO_3^-/CO_3^{2-}$ [44, 90, 92] and $H_2PO_4^-/HPO_4^{2-}/PO_4^{3-}$ [91] were investigated.

In this study, the measurement of pH is demonstrated in an electrochemical cell and during CO_2 electrolysis by *in operando* ^{13}C NMR, which has proven capable of investigating the $CO_2(aq)/HCO_3^-/CO_3^{2-}$ equilibrium in such an environment [62]. The method takes advantage of the high spectral resolution and sensitivity afforded by this cell design even in the presence of electrically conductive material [53]. In contrast to methods that only consider either the $CO_2(aq)/HCO_3^-$ [44] or the HCO_3^-/CO_3^{2-} equilibrium [92], the presented method provides data for a wider pH range by considering both equilibria, including an overlap region in-between. The sensitive volume of *in operando* NMR measurements is not limited to a few nanometres from the electrode as for surface-enhanced optical methods, and spatial resolution can be obtained by applying magnetic resonance

imaging techniques. Furthermore, NMR spectroscopy can provide a variety of additional information, *e.g.* about sample chemistry, mobility and structure.

To calculate the pH from *in operando* ^{13}C NMR data, we utilise the buffer capability of HCO_3^-/CO_3^{2-}. Depending on the pH, either the equilibrium between HCO_3^- and H_2CO_3, or the equilibrium between HCO_3^- and CO_3^{2-} is dominant [80],

$$CO_3^{2-} + H^+ \rightleftharpoons HCO_3^- \,, \qquad pK_{a1} = 10.3 \,, \tag{3.1}$$

$$HCO_3^- + H^+ \rightleftharpoons H_2CO_3 \quad \Big(\rightleftharpoons CO_2(aq) + H_2O \Big) \,, \qquad pK_{a2} = 6.4 \,. \tag{3.2}$$

Moret *et al.* have shown that due to the fast exchange between HCO_3^- and CO_3^{2-} compared to the NMR timescale given by the chemical shift difference, the ^{13}C resonances coalesce into a single peak with a pH dependent chemical shift. Hence, the term 'carbonate' is used in the following to describe both HCO_3^- and CO_3^{2-} in solution. The respective molecular formula is used when referring to a specific species. Alternatively, Scholz *et al.* estimated the pH in near neutral conditions using the Hendersson–Hasselbalch (HH) equation [93],

$$\mathrm{pH} = pK_{a2} + \log_{10} \frac{[HCO_3^-]}{[CO_2]} \,. \tag{3.3}$$

Here, both methods are combined to assess the possibility of pH measurements over a wide range from neutral to basic environments. This technique is then applied *in operando* by varying potential and electrolyte concentration for a comparison with theoretical predictions, and to obtain new insight about the interplay between local pH, CO_2 accessibility, and buffer capacity.

3.2 Methods and materials

The *in operando* electrolysis cell and the shielding setup were constructed as depicted in figure 2.11 and published previously [62]. In the following, only changes in the cell setup and the experimental procedure are mentioned.

3.2.1 Electrochemical cell

Copper foil (GoodFellow GmbH, Hamburg, Germany) with outer dimensions of 2.5 mm · 4 mm · 0.05 mm was perforated and the stripped end of a copper wire (GoodFellow GmbH, Hamburg, Germany) with 0.15 mm diameter and 0.025 mm PTFE insulation was pulled through the hole and twisted around itself to ensure contacting. For every experiment a new Working Electrode (WE) was used. Other electrodes were rinsed with demineralised water and reused. A capillary containing ^{13}C-labelled acetonitrile (99 atom-%, $^{13}CH_3{}^{12}CN$, Sigma Aldrich, Munich, Germany) was introduced into the cell as an external NMR reference. The liquid was pulled into a 50 µL capillary pipette (Hirschmann Laborgeräte GmbH & Co. KG, Eberstadt, Germany) by capillary forces before melting both ends of the capillary. The closed capillary was placed into the NMR tube in a way that the reference liquid is equally distributed in the sensitive volume of the probe. The reference substance did not only serve as a chemical shift reference, with a ^{13}C chemical shift of 4.43 ppm *vs.* trimethylsilylpropanoic acid (TSP) at 10 °C, but it could also be used to correct for amplitude fluctuations and phase drifts that may be caused by variations of the tuning mode during an experiment. Qualitatively, it indicated line shape changes induced by bubbles as well, but since these changes are different for the electrolyte and the reference sample, a correction is challenging and has not been attempted. The temperature-dependent ^{13}C chemical shift of $^{13}CH_3{}^{12}CN$, δ_{CH_3CN}, referenced to TSP is depicted in Figure 3.1. The linear correlation,

$$\delta_{CH_3CN} = -0.0104 \frac{\text{ppm}}{\text{°C}} \cdot T + 4.5308\,\text{ppm}\,, \tag{3.4}$$

where T is the temperature in °C, is used to estimate temperature gradients in the sample due to radio frequency excitation. A schematic of the electrochemical cell and the full assembly is depicted in figure 3.2.

3.2.2 Electrolyte preparation

^{13}C-enriched stock solutions of $KHCO_3$ (98 atom-%, Sigma Aldrich Chemie GmbH, Munich, Germany) were prepared at 0.1 M and 1 M concentrations and pre-electrolysed as described by Hori *et al.* [94] in order to remove impurities such as heavy metal ions, which will otherwise negatively affect the performance of the electrolysis. 20 mL of the respective stock solution were filled into a twin-necked flask connected to a Schlenk line and degassed by three freeze–pump–thaw cycles. Using two 5 mm · 5 mm platinum mesh electrodes (GoodFellow GmbH, Hamburg, Germany) a constant current of 150 µA was applied for 20 h while stirring with ca. 250 rpm using a magnetic stirrer. 600 µL of stock solution were

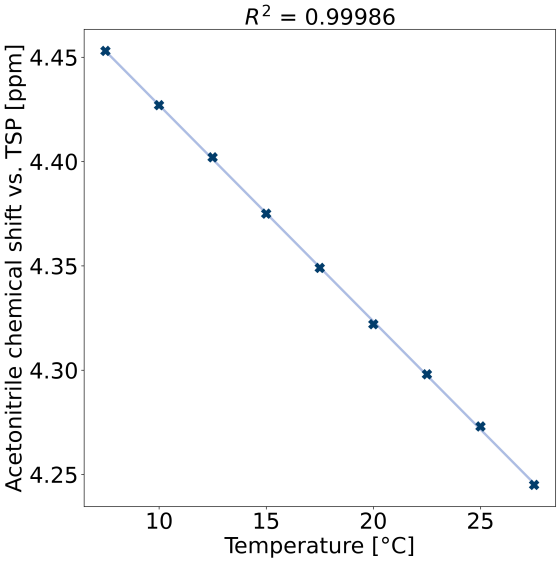

Figure 3.1: Temperature-dependent chemical shift of acetonitrile reference vs. TSP.

filled in a NMR tube and bubbled with ^{13}C-enriched CO_2 (99 atom-%, Sigma Aldrich, Munich, Germany) until saturation for ca. 20 min at a flow rate of ca. 0.3 $\frac{\text{mL}}{\text{s}}$. To maintain temperature stability, the sample was kept in a water bath at 10 °C during bubbling. The pH value was measured after CO_2 saturation and later after electrolysis using a benchtop Mettler–Toledo FiveEasy pH meter with a Mettler–Toledo InLab NMR pH electrode (Mettler–Toledo GmbH, Giessen, Germany) for direct pH measurement of the sample in the NMR tube. The three-electrode setup including the reference capillary was introduced afterwards into the NMR tube and the tube sealed with a gas tight cap. The NMR tube was mounted using a 3D-printed holder that fits onto the NMR probe and provides connectors for the electrodes to the potentiostat (figure 3.2c). The probe was pre-tempered at 10 °C to avoid degassing due to transient temperature effects during thermal equilibration.

3.2.3 Electrochemical parameters

The electrodes of the electrochemical cell were connected to a BioLogic SP-200 potentiostat (BioLogic Science Instruments, Seyssinet-Pariset, France). The employed micro RE exhibited a steady Open Circuit Voltage (OCV) of 0.115 ± 0.002 V *vs.* a commercial Ag/AgCl (3 M KCl) RE (Deutsche METROHM GmbH & Co. KG, Filderstadt, Germany) in a 1 M $KHCO_3$ solution. Potentials $E_{\text{microAg/AgCl}}$ measured with the micro RE are converted to the Standard Hydrogen Electrode (SHE) scale according to

$$E_{\text{SHE}} = E_{\text{microAg/AgCl}} + 0.205\,\text{V} - 0.73 \times 10^{-3}\,\text{V/°C} \cdot (T - 25\,\text{°C}) + 0.115\,\text{V}\,, \qquad (3.5)$$

where T is the temperature in °C [95]. Chronoamperometry (CA) measurements were conducted for 2 hours at constant potential, with seven data points in the range of

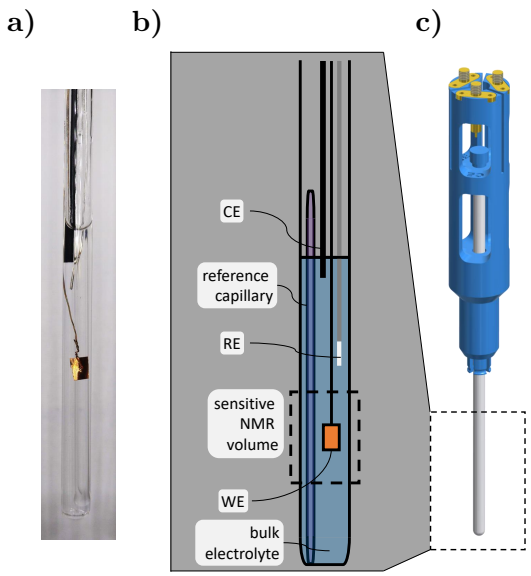

Figure 3.2: Electrochemical cell for *in operando* ^{13}C NMR. (a) Photograph and (b) schematic of the cell, including copper WE, chlorinated silver wire Reference Electrode (RE), graphite rod Counter Electrode (CE), and reference capillary. (c) Model of the 3D printed sample holder fitting onto the NMR probe.

$[-1.67\,\mathrm{V}, -1.07\,\mathrm{V}]$ *vs.* SHE and two repetitions. Results of CA measurements of 0.1 M and 1 M solutions are depicted in figure 3.3. Figures 3.3a and 3.3b show that bubble formation has an effect on the evolution of current density as well, which exhibits increasing fluctuations with more negative potential.

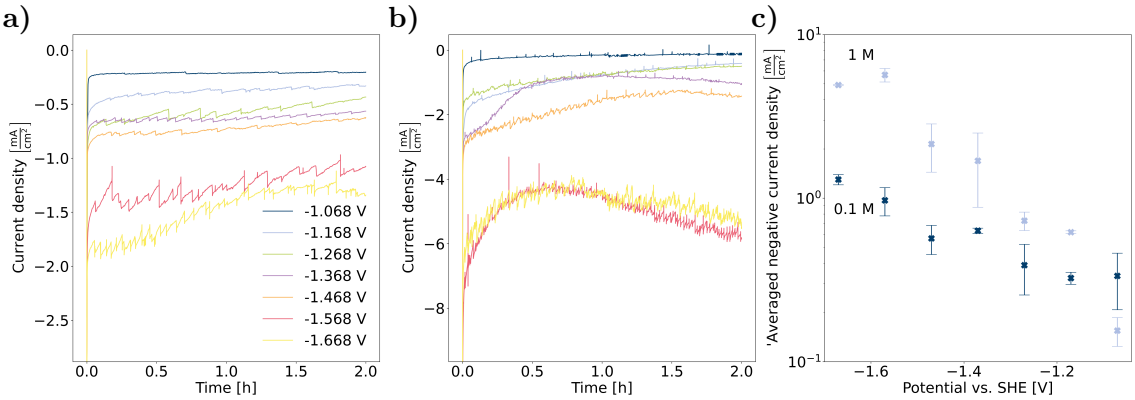

Figure 3.3: Results of CA measurements. (a) – (b) Evolution of the current density for 0.1 M and 1 M $KHCO_3$ solution, respectively. (c) Averaged negative current density during experiments with varying applied potential.

3.2.4 NMR parameters

The cell was inserted into a Bruker DiffBB broadband gradient probe on a Bruker Avance III HD spectrometer (Bruker BioSpin GmbH, Rheinstetten, Germany) with a 9.4 T wide-bore magnet, corresponding to a ^{13}C resonance frequency of 100.6 MHz. During CA, ^{13}C spectra were continuously recorded using 30°-pulses with ^{1}H decoupling (WALTZ-16 sequence with 128 repetitions every 2 s), resulting in acquisition of one spectrum every 6 min. A pulse length of 4 µs and a radio frequency power of 40.996 W was set. Spectra were processed with 1 Hz line broadening and zero-filling.

After the *in operando* experiment, electrodes and reference capillary were removed from the NMR tube and the sample was analysed *ex situ* to study the formation of liquid products. To enable quantification, a well-defined amount of the reference substance TSP was added to the sample, which resulted in a concentration of 1 mM. For higher sensitivity, ^{1}H NMR with water suppression using excitation sculpting with perfect echo was performed [96]. In addition, the sample was analysed at higher magnetic field of 18.8 T (800 MHz for ^{1}H) using a Bruker DiffBB probe. The relaxation delay was set to 5 s, and 256 scans were acquired. The pulse length was 21 µs and the pulse power was 27.58 W. The pulse length of the sine-shaped selective pulse was 800 µs and the respective pulse power was 0.21943 W. Resulting ^{1}H spectra are depicted in Figure 3.11, showing the formate resonance doublet at 8.46 ppm.

The Faradaic Efficiency (FE) of formate was calculated according to

$$\mathrm{FE} = \frac{s_{\mathrm{formate}}}{s_{\mathrm{TSP}}} \cdot 9 \cdot 2 \cdot 1 \,\frac{\mathrm{mmol}}{\mathrm{L}} \cdot 600\,\mu\mathrm{L} \cdot \frac{F}{\int_0^{2\,\mathrm{h}} I_{\mathrm{CA}}(t)\,\mathrm{d}t}, \tag{3.6}$$

where s_{formate} and s_{TSP} are the integrals of the formate and TSP resonances, respectively, F is the Faraday constant and $I_{\mathrm{CA}}(t)$ is the current as a function of time during the CA experiment. The factor 9 in equation 3.6 results from the ratio of equivalent protons in TSP and formate, and the factor 2 represents the number of electrons transferred per formate molecule formed.

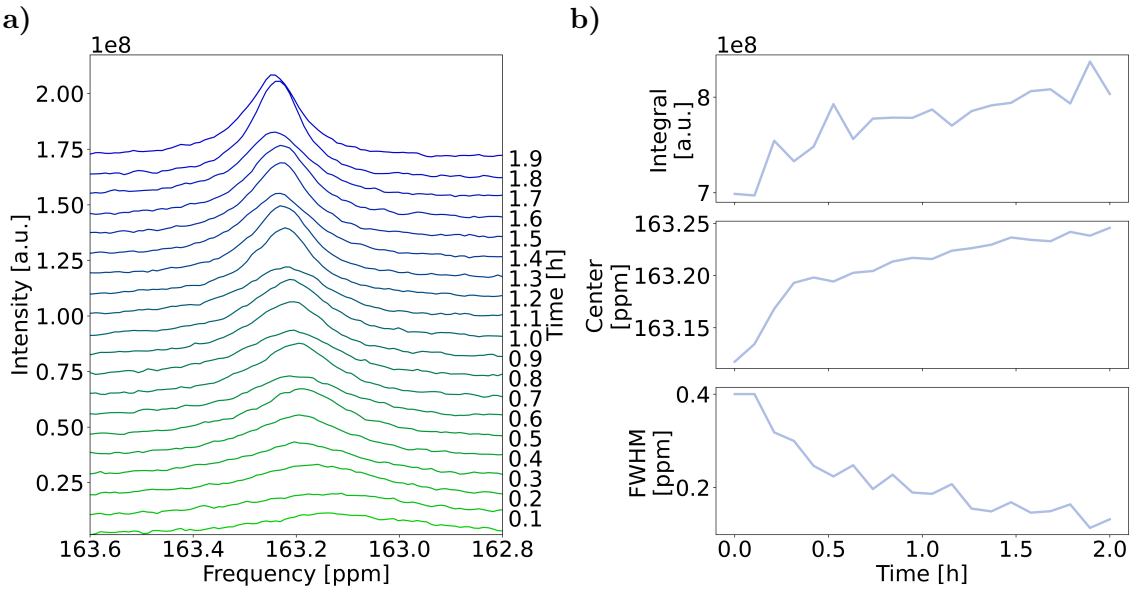

Figure 3.4: ^{13}C NMR resonance of carbonate during electrolysis at −1.47 V, with an initial $KHCO_3$ concentration of 0.1 M. (a) Evolution of the carbonate peak during 2 h of electrolysis. (b) Evolution of the integral (top), ^{13}C chemical shift (middle), and FWHM (bottom) of the Lorentzian function fitted to the carbonate peak during 2 h of electrolysis.

3.3 Results and discussion

In the ^{13}C NMR spectra, the three observed singlet resonances are assigned to the ^{13}C-labelled methyl carbon of the acetonitrile reference, to CO_2(aq), and to a coalesced resonance of HCO_3^- and CO_3^{2-} due to fast exchange between these species. The peak properties of the three ^{13}C signals, *i.e.* integral, position (chemical shift) and Full Width at Half Maximum (FWHM), were determined by peak fitting using a Lorentzian function, which provided an adequate fit. For error estimation, fluctuations of the fitted values are determined in terms of standard deviation using a 5-step moving average. Details about the error estimation are discussed in section 3.3.2. figure 3.4a shows the ^{13}C resonance of carbonate at −1.47 V as a function of time, with an initial $KHCO_3$ concentration of 0.1 M. The evolution of the fitted peak properties is shown in figure 3.4b. Further data representing experiments at different potentials and concentrations are shown in figure 3.5 and 3.6.

The carbonate chemical shift (CCS) moves downfield from an initial value of 163.12 ppm, while the integral of the carbonate peak increases. This constitutes a shift of the HCO_3^-/CO_2 equilibrium towards HCO_3^-, caused by an increasing local pH. The FWHM decreases due to faster exchange between carbonate species, which has been observed before by *in operando* NMR studies with silver WEs [62]. The fitting parameters exhibit fluctuations that can be attributed to gas bubble formation on the electrode during the electrochemical experiments. The magnetic susceptibility of gas bubbles differs markedly from the surrounding electrolyte, causing inhomogeneities in the magnetic field that are perceived as

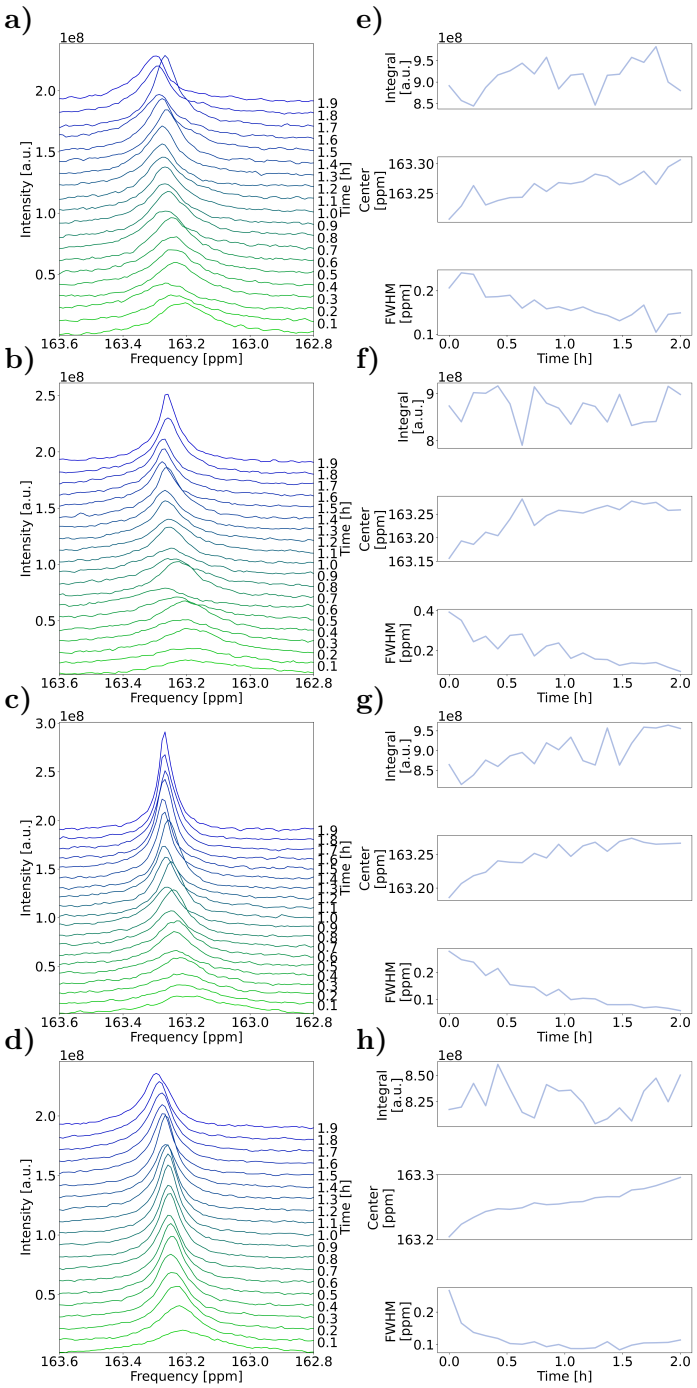

Figure 3.5: Results of *in operando* ^{13}C NMR measurements with 0.1 M initial $KHCO_3$ concentration. (a) – (d) Waterfall plots showing the change of the carbonate resonance during 2 h of electrolysis at −1.07 V, −1.27 V, −1.47 V and −1.67 V, respectively; (e) – (h) Evolution of the carbonate peak integral, chemical shift and FWHM during 2 h of electrolysis at −1.07 V, −1.27 V, −1.47 V and −1.67 V, respectively.

variations of the peak shape. Furthermore, the quality factor of the resonant circuit used for radio frequency excitation and detection changes, leading to an additional fluctuation

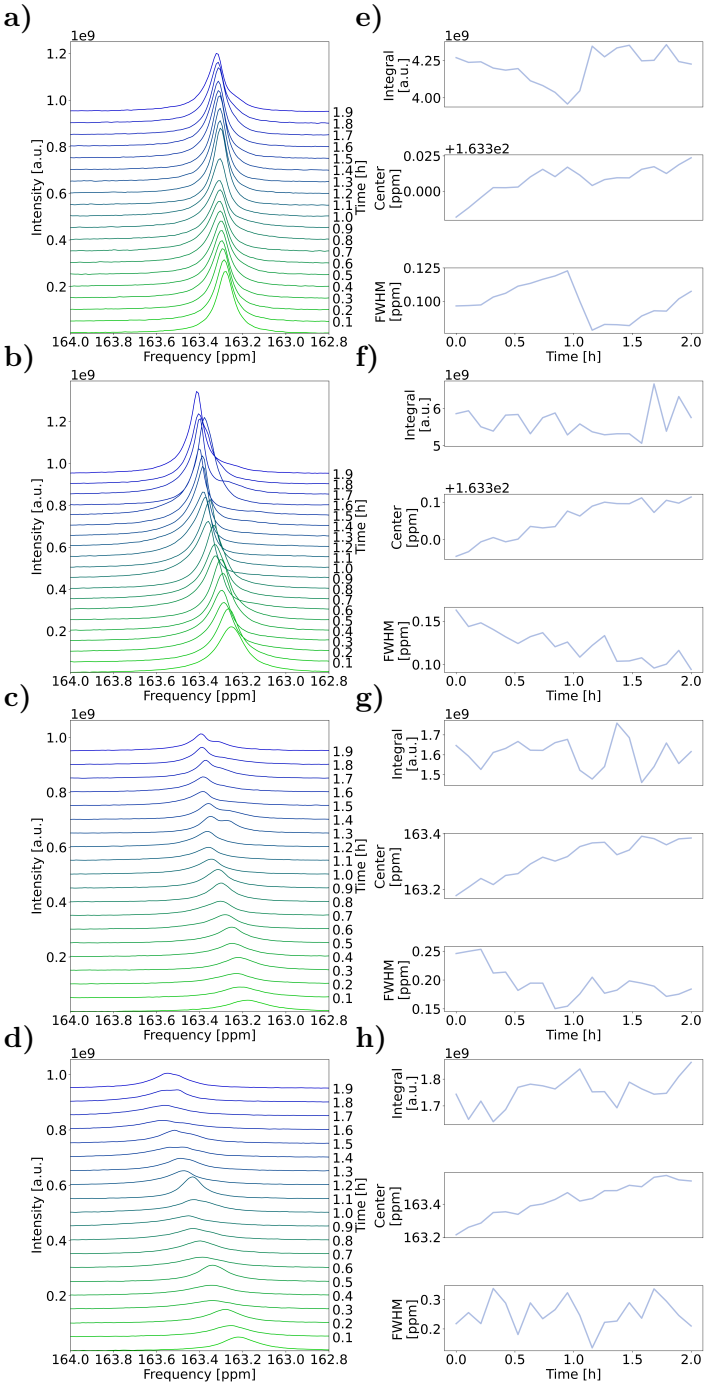

Figure 3.6: Results of *in operando* ^{13}C NMR measurements with 1 M initial $KHCO_3$ concentration. (a) – (d) Waterfall plots showing the change of the carbonate resonance during 2 h of electrolysis at −1.07 V, −1.27 V, −1.47 V and −1.67 V, respectively; (e) – (h) Evolution of the carbonate peak integral, chemical shift and FWHM during 2 h of electrolysis at −1.07 V, −1.27 V, −1.47 V and −1.67 V, respectively.

of the integral. The fluctuations of the resonance line parameters are 0.0192 ± 0.006 ppm for CCS, and 0.0281 ± 0.007 ppm for the FWHM. The fluctuations of the integral relative

to its initial value is $3.58 \pm 0.63\,\%$.

The integral of the CO_2 resonance at 127.5 ppm decreases, approaching zero during experiments with high negative potential. Relative to its initial value, the fluctuations of the integral are $7.80 \pm 0.88\,\%$. Chemical shift and width stay constant. This is expected and confirms that the origin of the aforementioned carbonate resonance shift is a variation of the HCO_3^-/CO_2 equilibrium.

Acetonitrile as reference substance is isolated by a glass capillary and consequently does not interact with other species during electrolysis. Hence, chemical shift, integral and width of its ^{13}C-labelled methyl group are unaffected by the electrolysis reaction itself. Still, the formation of gas bubbles leads to fluctuations of the line shape. Fluctuations of chemical shift and FWHM are 0.0177 ± 0.005 ppm and 0.035 ± 0.01 ppm, respectively. If these fluctuations would be exclusively caused by temperature fluctuations of the sample, the former would correspond to a change in temperature of about 0.1 °C.

To calculate the local pH from the carbonate chemical shift δ_c, a reference curve for the pH-dependence was recorded by titration of a 1 M $KHCO_3$ solution with 1 M KOH, which resulted in a typical sigmoidal curve depicted in figure 3.7a that was fitted by

$$\delta_c = \delta_{HCO_3^-} + \frac{\delta_{CO_3^{2-}} - \delta_{HCO_3^-}}{1 + 10^{pK_{a1} - pH}}\,. \tag{3.7}$$

Here, $\delta_{HCO_3^-}$ and $\delta_{CO_3^{2-}}$ represent the chemical shifts of the pure respective species and are fitted as $\delta_{HCO_3^-} = 163.267 \pm 0.036$ ppm, $\delta_{CO_3^{2-}} = 171.011 \pm 0.037$ ppm. The fitted pK_{a1} value was 9.645 ± 0.011.

This function is derived from the carbonate equilibrium. The HH equation can be applied to the equilibrium between the carbonate species HCO_3^- and CO_3^{2-},

$$pH = pK_{a1} + \log_{10}\frac{[CO_3^{2-}]}{[HCO_3^-]} \tag{3.8}$$

$$\Leftrightarrow \frac{[HCO_3^-]}{[CO_3^{2-}]} = 10^{pK_{a1} - pH}\,. \tag{3.9}$$

The measured chemical shift δ_c of the carbonate peak can be expressed as a function of the concentrations of the carbonate species,

$$\left|\frac{\delta_c - \delta_{HCO_3^-}}{\delta_{CO_3^{2-}} - \delta_{HCO_3^-}}\right| = \frac{[CO_3^{2-}]}{[CO_3^{2-}] + [HCO_3^-]} = \frac{1}{1 + \frac{[HCO_3^-]}{[CO_3^{2-}]}}\,. \tag{3.10}$$

Inserting equation 3.9 in equation 3.10 results in the function that is fitted to experimental data,

$$\delta_c = \delta_{HCO_3^-} + \frac{\delta_{CO_3^{2-}} - \delta_{HCO_3^-}}{1 + 10^{pK_{a1} - pH}}\,, \tag{3.11}$$

where the $\delta_{HCO_3^-}$ is the chemical shift of HCO_3^- and $\delta_{CO_3^{2-}}$ is the chemical shift of CO_3^{2-}. Both are predetermined by fitting of a titration curve.

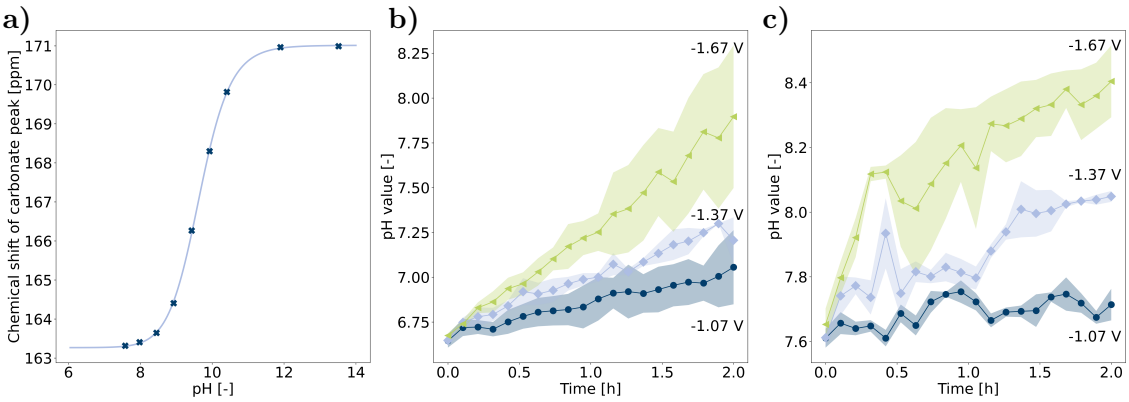

Figure 3.7: pH calculation using the CCS for pH $\geq$ 7.6 and the HH equation for pH $<$ 7.6. (a) pH dependent CCS at 10 °C. Data points are marked by crosses and the fitted sigmoidal function by a solid line. b-c) pH values as a function of time for initial electrolyte concentration of 0.1 M (b) and 1 M (c). Data points represent average value of experiments with an applied potential of −1.07 V (dark blue), −1.37 V (light blue) and −1.67 V (green). Coloured areas show minimum and maximum value of the respective data point in two repetitions of the experiments.

Equation 3.7 can be transformed to obtain an expression for the pH value,

$$\mathrm{pH} = \mathrm{p}K_{a1} + \log_{10}\left|\frac{\delta_c - \delta_{\mathrm{HCO_3^-}}}{\delta_c - \delta_{\mathrm{CO_3^{2-}}}}\right| . \tag{3.12}$$

Using the titration curve, a lower threshold of pH = 7.6 for reliable pH estimation by means

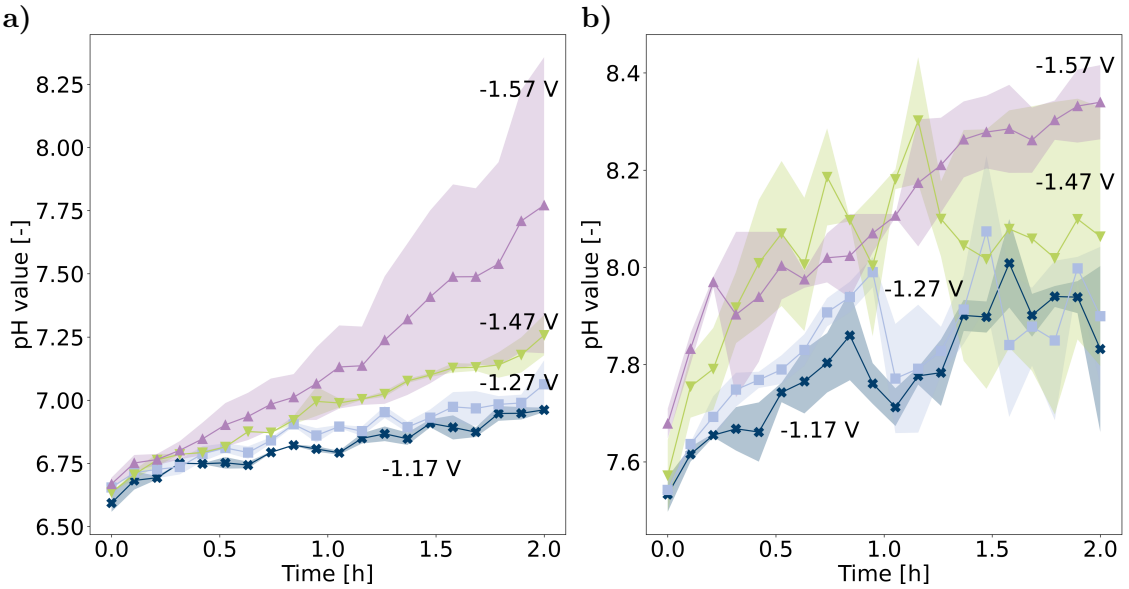

Figure 3.8: (a) – (b) Evolution of pH values as a function of time during electrolysis at various applied potentials for initial electrolyte concentrations of 0.1 M and 1 M, respectively.

of the CCS was obtained. Below this threshold, changes of the CCS are small compared to the measurement accuracy, and the equilibrium between CO_2(aq) and HCO_3^- is dominant. Therefore, the HH equation 3.3 is more accurate for the determination of the pH value below pH = 7.6. Here, the ratio of the integrals of CO_2(aq) and carbonate peak can be used equivalently to the ratio of the concentrations of the respective species [93].

The values for pK_{a1} and pK_{a2} vary from literature data, since experiments are carried out at 10 °C. Other influencing factors are the ionic strength of the electrolyte and the CO_2 concentration in the gas phase. Thus, the pK_{a2} value used for the application of equation 3.2 is determined experimentally using the HH equation 3.3 and the initial pH value in the NMR tube, which was measured with a pH meter before the experiment. Averaged over the whole data set, this resulted in a calculated pK_{a2} of 6.15 ± 0.06 and 6.02 ± 0.07 for the 0.1 M and 1 M experiments, respectively.

Figures 3.7b and 3.7c show the measured pH *vs.* time for $KHCO_3$ concentrations of 0.1 M and 1 M, respectively, and for three representative potentials. Further data representing experiments at other potentials are depicted in figure 3.8. A more negative potential results in an accelerated pH increase in both cases. In 0.1 M solution the increase is almost linear, while in 1 M solution a fast increase is observed at the beginning of the experiment, followed by a deceleration of this development. In curves that pass the threshold of pH 7.6 no discontinuity is found, which indicates that the used methods are compatible. For experiments with an initial $KHCO_3$ concentration of 0.1 M, the measured pH was mostly below the threshold pH 7.6. The data range shown in figure 3.7b is therefore larger than in 3.7c, where primarily the CCS function was used for pH determination. Increased fluctuations are explained by a larger impact of bubble formation on signal integrals compared to the effect on chemical shifts. For the highest applied potential, the highest rate of bubble formation is observed, which results in increased uncertainties in the pH value for both electrolyte concentrations. The error propagation in the HH (equation 3.3) and CCS method (equation 3.12) is discussed in section 3.3.1. The impact of the fluctuations in CCS and the integral of CO_2 and HCO_3^- on the error propagation is presented in section 3.3.2. It was found that the standard error of the pH value is mainly influenced by errors in the determination of the pK_{a1} and pK_{a2} values. Only when applying the CCS function in the limiting case near pH = 7.6, values of the pH standard error are up to 0.15 for 0.1 M solution and 0.29 for 1 M solution. These values are on the same order of magnitude as depicted in Figures 3.7b and 3.7c.

The evolution of the pH value is in accordance with pH values measured before and after electrolysis using a pH meter, *cf.* figure 3.9. All curves start at the expected pH value for CO_2-saturated $KHCO_3$ solution, *i.e.* at pH 6.7 for 0.1 M and at pH 7.6 for 1 M. Final pH values at the end of the electrolysis experiment are larger than the values measured with the pH meter. This could be a manifestation of non-equilibrium between carbon species in solution and CO_2 in the atmosphere caused by electrolysis, or it could be a local pH effect. Since the liquid–gas interface in the NMR tube is small and the distance between the surface and the WE is sizeable, $CO_2(g) \leftrightarrow CO_2(aq)$ exchange as well as

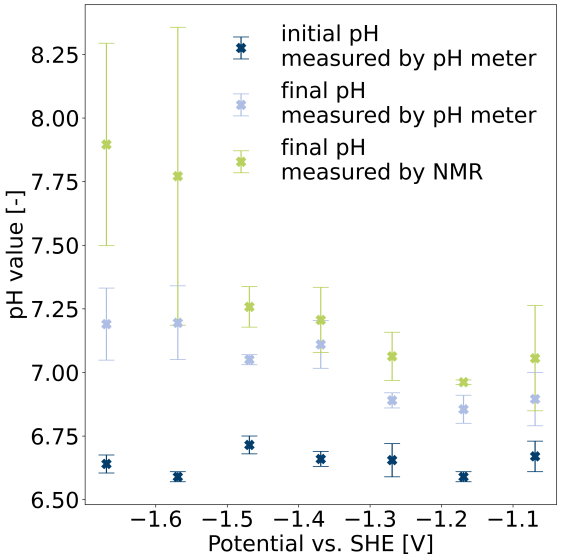

Figure 3.9: pH values measured by pH meter in the NMR tube before and after the electrolysis operation using 0.1 M initial $KHCO_3$ concentration in comparison with final values determined by *in operando* NMR.

CO_2 diffusion may not be fast enough to keep the electrolyte at the WE, which is in the region of the sample that is measured by NMR, in a quasi-equilibrium. After operation, the concentration equilibrates between gas and liquid phase as well as between bulk and WE proximity. Therefore, the pH measured by the pH meter after electrolysis is lower than the final pH measured by *in operando* NMR. The NMR measurements represent a statistical average over the whole NMR sensitive volume around the electrode, which means that even higher pH near the electrode surface could be expected. Since the line width of the carbonate peak is small, no substantial spatial distribution of pH is indicated. Therefore, the equilibration of the pH value inside the sensitive NMR volume is faster than the change of the pH. Such an equilibration would not be expected on the timescale of the experiment if only self-diffusion in aqueous media would be considered. It may be facilitated by diffusion caused by a concentration gradient due to electrolysis at the electrode, or by convection due to Joule heating. Only minor temperature differences can cause sufficient motion in the sample to achieve such an averaging at the employed low current densities. At the same time, as postulated by Varela *et al.*, the local pH of a dilute $KHCO_3$ solution might even exhibit the local pH of a more concentrated solution [40]. The data in figure 3.7b and 3.7c show larger difference between measured and initial pH for the more dilute solution, thus confirming such a hypothesis.

The potential-dependent local pH can be qualitatively compared to the calculations by Gupta *et al.* [39]. Figure 3.10a depicts the final pH value determined by *in operando* NMR as a measure for the pH in the vicinity of the electrode as well as the final CO_2

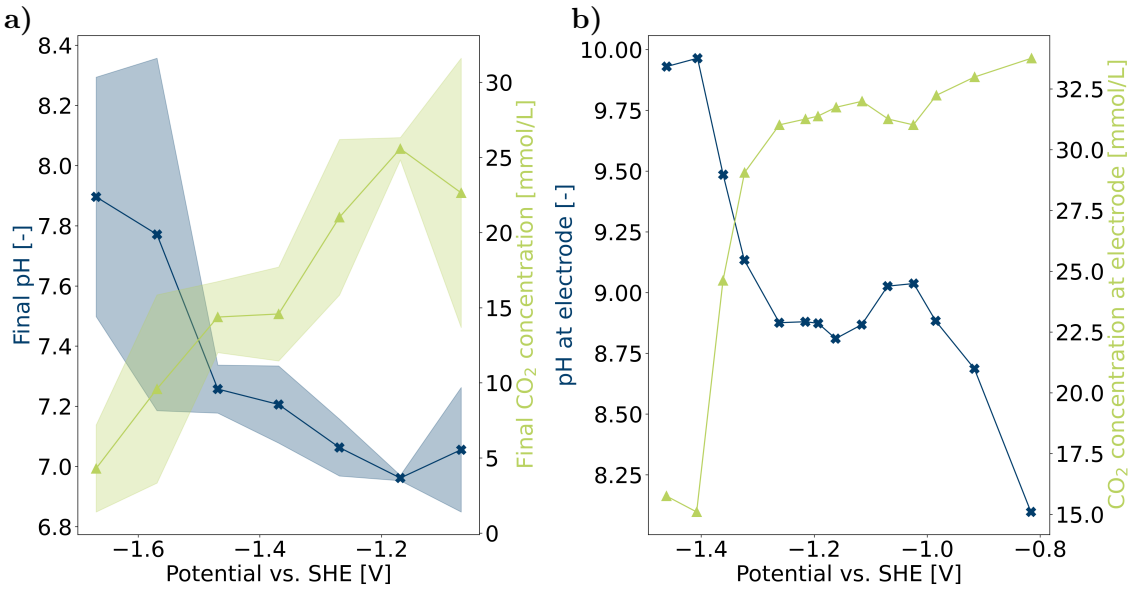

Figure 3.10: Comparison of experimental and theoretical potential-dependent pH and CO_2 concentration. (a) pH (·) and CO_2 concentration (△) values determined by ^{13}C NMR at the end of a potential step, recorded at potentials between −1.07 V and −1.67 V; (b) Calculated pH (·) and CO_2 concentration (△) at the electrode. Values are taken from Figure 8 in Gupta *et al.* [39]. Since final values of the measured average over a volume surrounding the electrode from a batch experiment are compared with steady state values in direct electrode proximity from a computer calculation, this depiction serves as a qualitative comparison only.

concentration $[CO_2]_{final}$. It was determined using

$$[CO_2]_{final} = \frac{s_{CO_2,final}}{s_{CO_2,initial}} \cdot [CO_2]_{sat}, \tag{3.13}$$

where an initial saturation concentration $[CO_2]_{sat}$ of 52.7 mM at 10 °C is assumed [62], and $s_{CO_2,final}$ and $s_{CO_2,initial}$ are the final and initial integrals of the CO_2 resonance, respectively. Final pH values and CO_2 concentrations show an opposing course, *i.e.* low pH and high CO_2 concentration for low potentials and vice versa for high potentials. A plateau between −1.1 V and −1.4 V is followed by an abrupt increase in pH and therefore decrease in CO_2 concentration at more negative potential. This course can also be observed in the data of Gupta *et al.*, shifted by approximately 100 mV to higher potentials, as depicted in figure 3.10b. Such a shift may be caused by the absence of an iR drop in the theoretical study. Katsounaras *et al.* attribute this plateau to inhibition of the HER in the specific local pH region resulting from the applied potentials [97].

After electrolysis, the electrodes are removed from the electrolyte. The liquid solution is then analysed *ex situ* to detect liquid products that have formed during electrolysis. Reference compound TSP is added to obtain a concentration of 1 mM and the sample is investigated by ^{1}H NMR with water suppression at a magnetic field of 18.8 T (800 MHz for

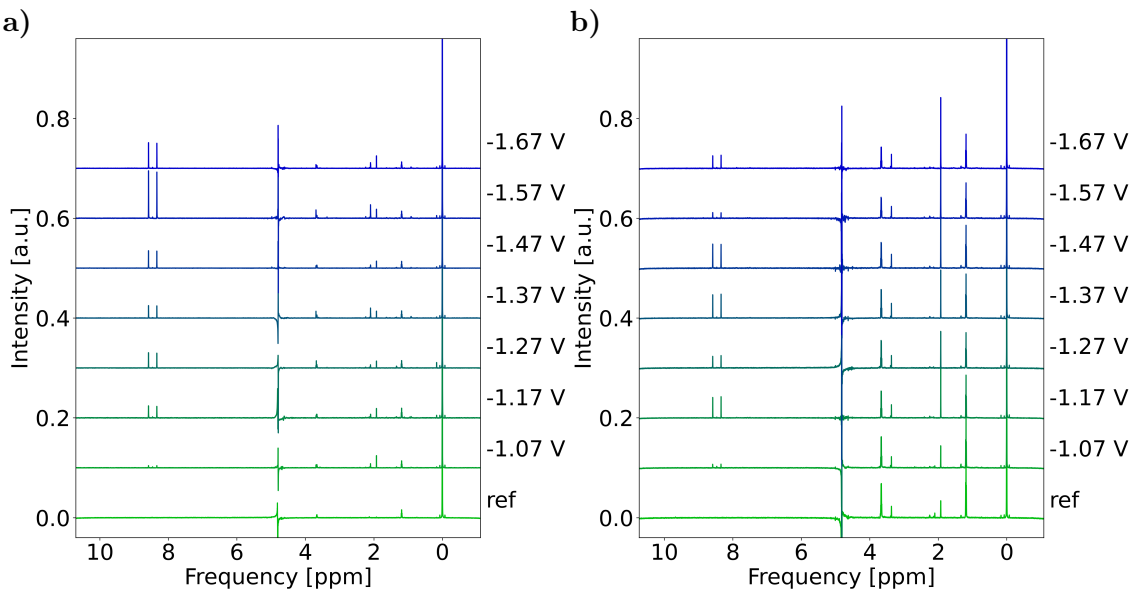

Figure 3.11: ^{1}H *ex situ* NMR spectra of the electrolyte solution after electrolysis with varying potential for initial electrolyte concentration of 0.1 M (a) and 1 M (b), respectively. Spectra marked with "ref" represent measurements of a sample of the respective stock solution without any potential applied to distinguish between impurities and reaction products.

^{1}H). Formate is the major liquid product in Cu-catalysed eCO_2R at the employed current densities [31]. Other ^{13}C-labelled molecules could not be identified in our experiments, *cf.* figure 3.11 for the ^{1}H spectra.

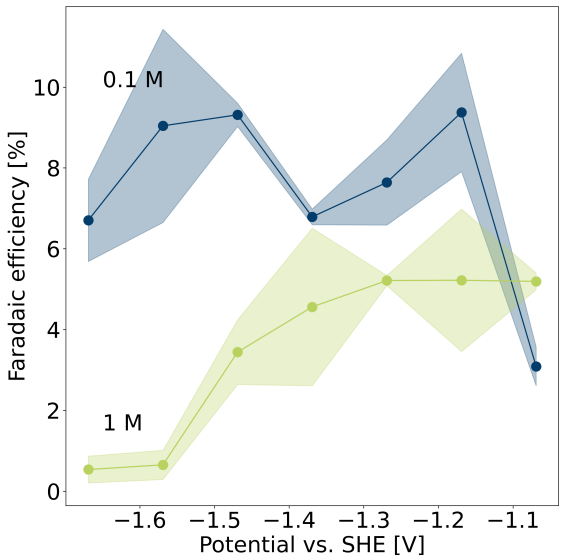

Figure 3.12: Potential-dependent Faradaic efficiencies of formate production in 1 M (green) and 0.1 M (blue) $KHCO_3$ solution.

Low selectivity for these products, a polycrystalline and untreated Cu surface, or even

contamination by Ag^+ ions from the RE could be possible reasons [98]. However, potential-dependent FE of formate, depicted in figure 3.12, show varying selectivity for this reaction pathway for the initial carbonate concentrations in consideration. The reaction pathway to formate is reported as a "dead-end road", as it is not further reduced on a Cu electrode [80], although others suggest a possible pathway to methanol [13]. However, it competes with the pathway to CO and its further reduction products, *i.e.* methane, ethylene and other short-chain hydrocarbons. Therefore, the formation of formate is used to distinguish the favoured reaction pathway under varying conditions [41]. Since anode and cathode are not separated by a membrane in the electrochemical cell, it also cannot be ruled out that products formed at the WE are subsequently oxidised at the CE. This will not influence the local pH measurements at the WE, but may explain why the measured values are lower compared to literature [31]. In general, FE for formate is lower over the whole potential range for the more concentrated solution. At high potentials, the FE approaches zero. This is expected, as at high potential and/or strongly basic local conditions formate formation was found to be suppressed due to progressing desorption of bicarbonate [87]. Simultaneously, high FE for HER were reported for these conditions [31]. The strong suppression of formate formation at the most negative potentials could also be caused by the dynamic change of surface pH: figure 3.7c shows a rapid increase in local pH in the first minutes of operation, inhibiting any further formate formation during electrolysis.

The suppression of formate formation is less pronounced in 0.1 M solution as the pH value at the beginning of the experiment is lower compared to the 1 M solution. Only towards the end of the experiment the increase in local pH inhibits formate formation. In the investigated potential range, the formate formation in the diluted solution is therefore almost potential-independent.

3.3.1 Propagation of uncertainty

An estimate for the error of the described pH quantification method can be obtained using a simplified error propagation discussion that assumes uncorrelated errors for the different experimental parameters. Both the CCS method as well as the HH method share the same functional form,

$$\mathrm{pH} = \mathrm{p}K_a + \log\frac{\alpha}{\beta}\,, \tag{3.14}$$

where α represents $[HCO_3^-]$ for the HH and $(\delta_c - \delta_{HCO_3^-})$ for CCS method, and β represents $[CO_2]$ for the HH and $(\delta_{CO_3^{2-}} - \delta_c)$ for the CCS method. The standard error of the pH, $\varepsilon_{\mathrm{pH}}$, can be estimated as

$$\begin{aligned}\varepsilon_{\mathrm{pH}} &= \sqrt{\left(\frac{\partial \mathrm{pH}}{\partial \mathrm{p}K_a}\right)^2 \varepsilon^2_{\mathrm{p}K_a} + \left(\frac{\partial \mathrm{pH}}{\partial \alpha}\right)^2 \varepsilon^2_{\alpha} + \left(\frac{\partial \mathrm{pH}}{\partial \beta}\right)^2 \varepsilon^2_{\beta}} \\ &= \sqrt{\varepsilon^2_{\mathrm{p}K_a} + \left(\frac{\varepsilon_\alpha}{\ln(10)\alpha}\right)^2 + \left(\frac{\varepsilon_\beta}{\ln(10)\beta}\right)^2}\,,\end{aligned} \tag{3.15}$$

where $\varepsilon_{\mathrm{p}}K_a$, ε_α and ε_β represent the standard errors of pK_a, α and β, respectively. In other words, the standard error of the pH value combines the standard error of pK_a with the relative errors of α and β. Even though logarithmic functions with an argument far away from 1 are not particularly well suited for a linear approximation as used by equation 3.15, the result is qualitatively plausible. Any pH detection method that relies on the determination of a ratio of protonated and deprotonated species becomes inaccurate once only one species is present in detectable quantities.

Using Equation 3.15, the standard error for the HH method can be written as

$$\varepsilon_{\mathrm{pH}} = \sqrt{\varepsilon^2_{\mathrm{p}K_{a2}} + 0.189\left(\frac{\varepsilon_{[\mathrm{HCO_3}^-]}}{[\mathrm{HCO_3}^-]}\right)^2 + 0.189\left(\frac{\varepsilon_{[\mathrm{CO_2}]}}{[\mathrm{CO_2(aq)}]}\right)^2}, \tag{3.16}$$

where $\varepsilon_{[\mathrm{CO_2}]}$ and $\varepsilon_{[\mathrm{HCO_3}^-]}$ are the standard error of $[\mathrm{CO_2}]$ and $[\mathrm{HCO_3}^-]$, respectively. For the CCS method,

$$\varepsilon_{\mathrm{pH}} = \sqrt{\varepsilon^2_{\mathrm{p}K_{a1}} + 0.189\left(\frac{\varepsilon_{\delta_c-\delta_{\mathrm{HCO_3}^-}}}{\delta_c-\delta_{\mathrm{HCO_3}^-}}\right)^2 + 0.189\left(\frac{\varepsilon_{\delta_{\mathrm{CO_3}^{2-}}-\delta_c}}{\delta_{\mathrm{CO_3}^{2-}}-\delta_c}\right)^2}, \tag{3.17}$$

where $\varepsilon_{\delta_c-\delta_{\mathrm{HCO_3}^-}}$ and $\varepsilon_{\delta_{\mathrm{CO_3}^{2-}}-\delta_c}$ are the standard error of $\delta_c-\delta_{\mathrm{HCO_3}^-}$ and $\delta_{\mathrm{CO_3}^{2-}}-\delta_c$, respectively. Alternatively, equation 3.17 can be rewritten in terms of the individual standard errors ε_{δ_c}, $\varepsilon_{\delta_{\mathrm{HCO_3}^-}}$ and $\varepsilon_{\delta_{\mathrm{CO_3}^{2-}}}$ of δ_c, $\delta_{\mathrm{HCO_3}^-}$ and $\delta_{\mathrm{CO_3}^{2-}}$, respectively, as

$$\varepsilon_{\mathrm{pH}} = \sqrt{\varepsilon^2_{\mathrm{p}K_{a1}} + 0.189\left(\frac{\varepsilon_{\delta_c}}{\delta_c-\delta_{\mathrm{HCO_3}^-}} + \frac{\varepsilon_{\delta_c}}{\delta_{\mathrm{CO_3}^{2-}}-\delta_c}\right)^2 + 0.189\left(\frac{\varepsilon_{\delta_{\mathrm{HCO_3}^-}}}{\delta_{\mathrm{HCO_3}^-}-\delta_c}\right)^2 + 0.189\left(\frac{\varepsilon_{\delta_{\mathrm{CO_3}^{2-}}}}{\delta_c-\delta_{\mathrm{CO_3}^{2-}}}\right)^2}. \tag{3.18}$$

Here the partial derivatives

$$\frac{\partial \mathrm{pH}}{\partial \delta_c} = \left[\frac{1}{\delta_c-\delta_{\mathrm{HCO_3}^-}} + \frac{1}{\delta_{\mathrm{CO_3}^{2-}}-\delta_c}\right] \Big/ \ln(10) \tag{3.19}$$

$$\frac{\partial \mathrm{pH}}{\partial \delta_{\mathrm{HCO_3}^-}} = \frac{1}{\ln(10)(\delta_{\mathrm{HCO_3}^-}-\delta_c)} \tag{3.20}$$

$$\frac{\partial \mathrm{pH}}{\partial \delta_{\mathrm{CO_3}^{2-}}} = \frac{1}{\ln(10)(\delta_c-\delta_{\mathrm{HCO_3}^-})} \tag{3.21}$$

have been used.

It is apparent from the equations for the standard error of a pH value that at the fringes of the validity range of a particular technique the error starts to diverge. The farther the pH from a pK_a value, the larger $\varepsilon_{\mathrm{pH}}$ becomes, even if the error of a measured chemical shift or concentration value remains constant. This is particularly relevant if bubbles increase the uncertainty of the measured values relative to the error of the pK_a.

Since the pK_a value used for data analysis is typically only determined once for a particular set of measurements, its error appears as a systematic error. If it cannot be neglected compared to the other errors, it needs to be added manually to the error obtained from experiment repetitions.

3.3.2 Error estimation

To estimate the errors caused by bubble formation at the electrode, the fluctuation of the fitted peak properties, *i.e.* integral, chemical shift and FWHM, are determined in terms of standard deviation of the measured values from a 5-step moving average. The resulting errors are plotted in figure 3.13. The integral fluctuations are referenced to their initial value. To assess the uncertainties in the measurement of the CCS, the fluctuations of chemical shift and FWHM of carbonate and reference peak are referenced to the total change of CCS during the experiment. High error values of the CO_2 peak can be attributed to the depletion of CO_2 during the experiment and therefore poor signal-to-noise ratio.

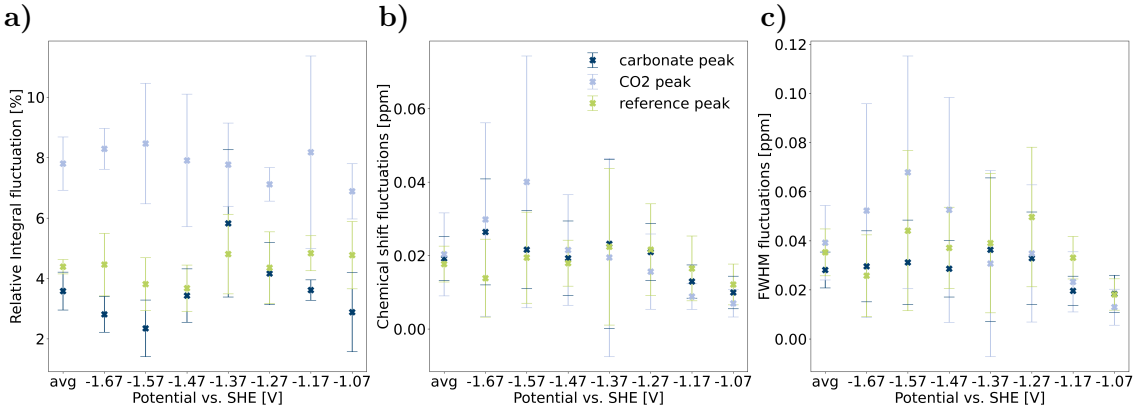

Figure 3.13: Estimation of errors due to bubble formation. (a) – (c) Fluctuations of carbonate, CO_2 and reference peak in terms of integral, chemical shift and FWHM, respectively. Fluctuation values are determined as standard deviation between measured values and a 5-step moving average. The fluctuations in the integral values are given relative to their initial value.

To quantify the maximum errors resulting from the error propagation due to bubble formation, the presented fluctuation values are used as standard errors in equation 3.16 and 3.18. For the estimation of the standard error of the pH value calculated using the HH equation, the values in table 3.1 are inserted into equation 3.16. The errors of pK_{a2} result from statistical averaging.

For the determination of $\varepsilon_{\mathrm{pH}}$ of the CCS method, it is assumed that the terms in equation 3.18 including $\varepsilon_{\delta_{\mathrm{HCO_3^-}}}$ and $\varepsilon_{\delta_{\mathrm{CO_3^{2-}}}}$ can be neglected. These errors originate exclusively from fitting of the titration function of equation 3.11 to experimental data, which resulted in a coefficient of determination $R^2 = 0.999$. The remaining variables to be inserted into equation 3.18 are noted in table 3.2. The best and the worst case for δ_c

	0.1 M	1 M
$\varepsilon_{\mathrm{p}K_{a2}}$	0.06	0.07
$\frac{\varepsilon_{[\mathrm{HCO_3}^-]}}{[\mathrm{HCO_3}^-]}$	0.0344	0.0379
$\frac{\varepsilon_{[\mathrm{CO_2}]}}{[\mathrm{CO_2(aq)}]}$	0.0663	0.0901
$\varepsilon_{\mathrm{pH}}$	0.0682	0.0819

Table 3.1: Error values for the determination of $\varepsilon_{\mathrm{pH}}$ according to the error propagation described in equation 3.16.

are both considered, *i.e.* $\delta_c(\mathrm{pH} = \mathrm{p}K_{a1} = 9.645) = 167.14$ and $\delta_c(\mathrm{pH} = 7.6) = 163.31$, respectively. The standard errors for peak integral and chemical shift in table 3.1 and 3.2 are values averaged over the whole data set.

	0.1 M		1 M	
	$\mathrm{pH} = \mathrm{p}K_{a1}$	$\mathrm{pH} = 7.6$	$\mathrm{pH} = \mathrm{p}K_{a1}$	$\mathrm{pH} = 7.6$
$\varepsilon_{\mathrm{p}K_{a2}}$	0.011		0.011	
ε_{δ_c}	0.0137		0.0262	
$\delta_c - \delta_{\mathrm{HCO_3}^-}$	3.874	0.039	3.874	0.039
$\mathrm{CO_3}^{2-} - \delta_c$	3.871	7.705	3.871	7.705
$\varepsilon_{\mathrm{pH}}$	0.011	0.154	0.011	0.291

Table 3.2: Error values for the determination of $\varepsilon_{\mathrm{pH}}$ according to the error propagation described in equation 3.18.

3.4 Conclusion

In operando determination of pH in electrode proximity in a bicarbonate/carbonate electrolyte system using ^{13}C NMR spectroscopy is demonstrated. In a pH range between approximately 4 to 12, a combination of titration curve of the carbonate chemical shift and the Hendersson–Hasselbalch equation has proven to be robust even when the system is disturbed by the formation of gas bubbles. The potential dependent changes of local pH and CO_2 concentration are in qualitative accordance with simulated data from literature. The experiments demonstrate a significant increase in local pH, emphasising that the bulk pH cannot be assumed to correctly describe reaction conditions in direct electrode vicinity. Dilute electrolytes with a low bulk pH but also low buffer capacity might even result in higher local pH than found in a concentrated electrolyte. *Ex situ* product analysis indicates that the formate production is consistent with such a dependence on the local pH, influenced by the applied potential and the buffer capacity of the electrolyte.

3.5 Postface

The main part of this chapter was performed and researched by the author of the thesis, in particular:

1. The development and construction of the *in operando* electrolysis setup and cell.
2. The conduction of the *in operando* NMR experiments of CO_2 electrolysis at Cu WE.
3. The processing and analysis of all electrochemical experiments.
4. The processing and analysis of all NMR experiments

Minor parts of this chapter were performed with assistance of the following co-worker:

1. The development and construction of the *in operando* electrolysis setup and cell was assisted by Sven Jovanovic (IEK-9, Forschungszentrum Jülich GmbH, Germany).

Chapter 4

Advancement of the *in operando* NMR setup in terms of reproducibility, product analysis and application of MRI techniques

4.0 Preface

In this chapter, the presented cell is adjusted to fit the requirements of MRI. The new cell designs are evaluated with regard to reproducibility of electrochemical and catalytic properties. The sections 4.2.2 and 4.2.3 of this chapter are based on the open access publication

Interplay of local pH and cation hydrolysis during electrochemical CO_2 reduction visualized by *in operando* chemical shift resolved Magnetic Resonance Imaging,

by Michael Schatz (corresponding author), Johannes Kochs, Sven Jovanovic, Rüdiger-A. Eichel and Josef Granwehr, published in *ChemRxiv*, DOI: 10.26434/chemrxiv-2023-q80nz (2023).

4.1 Introduction

The presented pH determination method has proven capable of elucidating the local pH value at a Cu electrode during electrochemical Carbon Dioxide Reduction (eCO_2R). These measurements can be described as "local", because the Working Electrode (WE) is placed in the middle of the sensitive Nuclear Magnetic Resonance (NMR) volume and the acquired signal therefore originates from electrolyte in close proximity to the WE. However, the volume close to the WE, where the actual reaction takes place, is small compared to the sensitive volume. By applying Magnetic Resonance Imaging (MRI) techniques, the sensitive volume, and consequently the electrolyte in electrode vicinity, can be investigated with higher spatial resolution.

In this chapter, the adjustments made to the electrochemical cell and experimental procedures to enable MRI measurements that can be reproducibly conducted multiple times, are presented and validated. The setup for noise reduction by filtering, shielding, and grounding, based on previous work [62], was adopted, while other parts were adjusted. On the one hand, the cell design had to be compatible with the one-dimensional magnetic field gradient of the utilised probe. Distortions of B_0 and B_1 field in the adjusted cell due to introducing electrically conductive material were estimated experimentally and supported by simulations.

On the other hand, the experimental procedure had to be improved to ensure safe and reproducible measurement series for a potential dependent study. In the course of data interpretation in chapter 3, large error bars were given for individual data points, which required extensive discussion of error propagation in the experiments. Hence, various measures were taken to improve reproducibility of the electrochemical conditions at the WE and, therefore, product distribution of eCO_2R. These alterations of the experiments were first evaluated by conducting electrolysis outside the NMR spectrometer, before the improved experimental procedure is applied in the *in operando* measurements presented in the following chapter.

During the development of the electrochemical cell for MRI applications, it was noted that increased bubble attachment near the electrode was distorting the electrochemical experiments as well as MRI measurements. The influence of these effects on the potential and the imaging experiments are shown and their inhibition by well-conceived cell design is presented.

While the WE and Counter Electrode (CE) were not separated by a membrane in the established cell setup, a way to integrate a Nafion membrane in the confined space of the NMR tube is presented. Here, a tubular ion exchange membrane was placed around the cylinder-shaped CE to prevent reduction products formed at the WE being reoxidised at the CE.

Finally, all adjustments are validated and evaluated by comparing the electrochemical performance as well as the product distributions of eCO_2R of the most important cell configurations.

4.2 Adjustment of *in operando* experiments

4.2.1 Experimental setup

When planning a large number of experiments, easy assembly of the electrochemical cell and safe insertion into the probe has to be ensured. The practical usage of standard NMR tubes was maintained, since it allows for the usage of standard NMR probes. Also, the cell can easily be assembled by simply introducing the electrodes and sealing the NMR tube with a standard tube cap and Parafilm. This also enables easy handling of the electrolyte for product analysis after *in operando* experiments.

To use the sample lift for safe transfer of the cell into the probe, the holder of the cell was adjusted to fit the outer dimensions of an NMR tube in a standard spinner, depicted in figure 4.1.a. The main body was 3D printed from polylactide (PLA) filament (Filamentworld, Neu-Ulm, Germany) and equipped with SMA connectors to provide contact to the potentiostat. Wires that contact the three electrodes in the cell were soldered to these connectors. The shielded cables were attached using screw fixings, which allowed for easy lowering of the cell into the probe and removal from the probe by simply pulling out the cables. The holder with NMR tube is illustrated in figure 4.1.b.

Due to the narrower opening at the top of the sample lift, a redesign of the shielding cap was necessary that was previously tailored to the wide bore of the magnet without the sample lift inserted. The cap has to be made of a highly conductive material with good shielding properties, such as brass in this case, and must fit exactly into the opening of the sample lift, leaving no gaps to guarantee proper shielding from Radio Frequency (RF) radiation. The cap designed for this purpose is depicted in figure 4.1.c and the technical drawings in figure 4.1.d and 4.1.e. It consisted of two lathe-turned parts that are connected via a clearance fit. The lower part fitted into the opening of the sample lift, while the upper part provided the electrical connection to the potentiostat. In the latter, two SMA flanges were fastened by screws on each side of three through-holes, respectively, as depicted in the sectional view in figure 4.1.e. The recess inside of the cap was used to stow away excess wire for the connection to the cell holder.

4.2.2 Electrochemical cells

The electrochemical cell in a 5 mm outer diameter NMR tube was adjusted to meet the requirements for MRI. The Bruker DiffBB broadband gradient probe, operated on a Bruker Avance III HD spectrometer (Bruker BioSpin GmbH, Rheinstetten, Germany) with a 14.1 T wide-bore magnet, offers magnetic field gradients along the longitudinal axis of the NMR tube. Placing the Cu WE perpendicularly to the direction of these gradients as depicted in figure 4.2.a-c, enables profiling in a single dimension as a function of distance from the WE due to rotational symmetry about the z-axis. The position of the WE is fixed by a holder made of chemically inert polyether ether ketone (PEEK). Different types of WE and CE configurations were tested using the exact same PEEK holder. Firstly, a

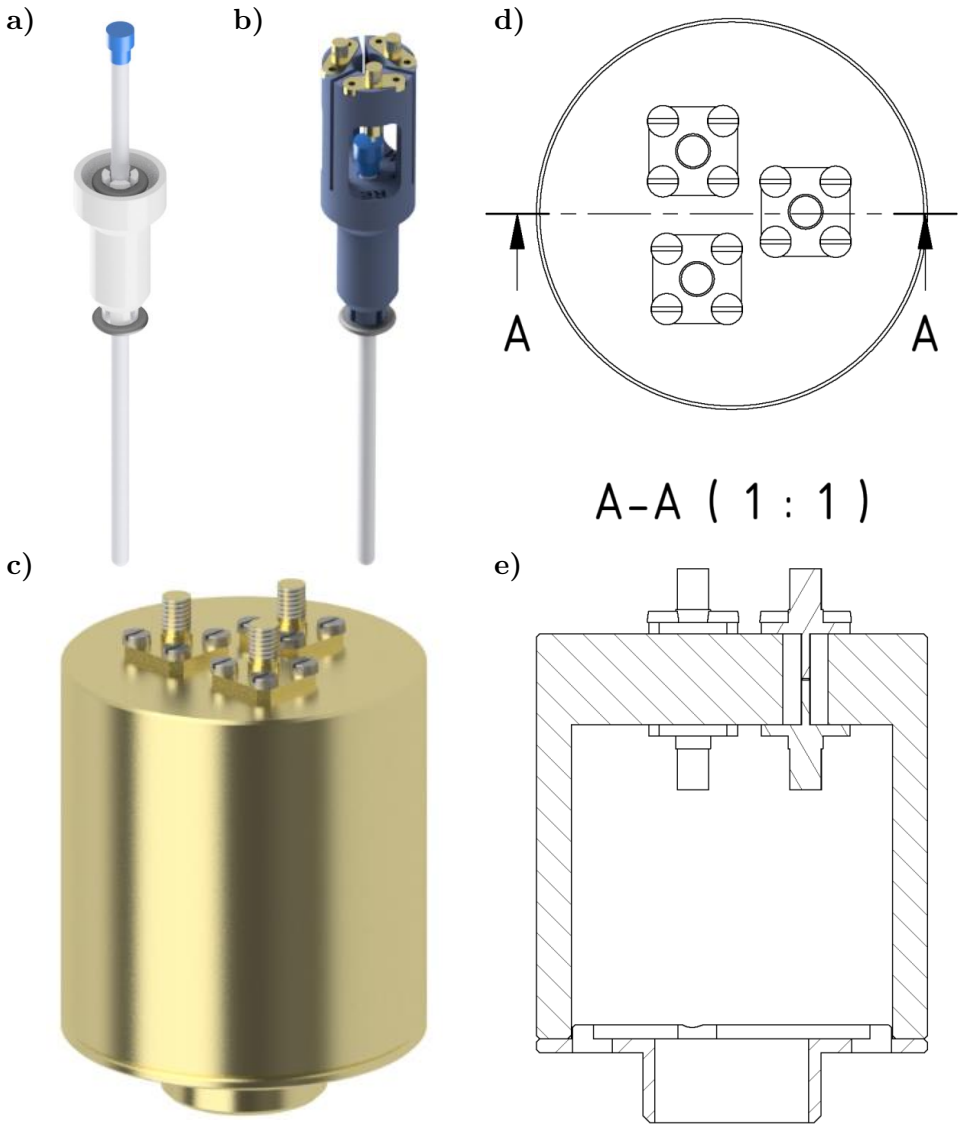

Figure 4.1: (a) Standard NMR tube in spinner. (b) 3D-printed holder for NMR tube containing the electrochemical cell. SMA connectors provide contact between the electrodes of the cell with a potentiostat. (c) Brass cap for shielding of the spectrometer.)d) Top view on the shielding cap with SMA flange connectors. (e) Sectional view of the shielding cap, showing the upper lathe-turned part for electrical connection to the electrodes and the lower part for fixation of the cap on top bore of the spectrometer.

3 mm Cu foil was precisely fitted into a 3 mm notch of the holder, *cf.* figure 4.2.a. The stripped end of an insulated Cu wire is introduced trough an eyelet to contact the Cu electrode from underneath. In the following, this cell setup is called setup A. To avoid the contact of PEEK with the electrolyte, a 4 mm WE is placed on top of the holder to fit exactly into the 4mm inner diameter of the standard NMR tube, *cf.* figure 4.2.b and 4.2.d. In the following, this cell setup is called setup B. The stripped end of an insulated Cu wire (GoodFellow GmbH, Hamburg, Germany) secures the WE on the holder and

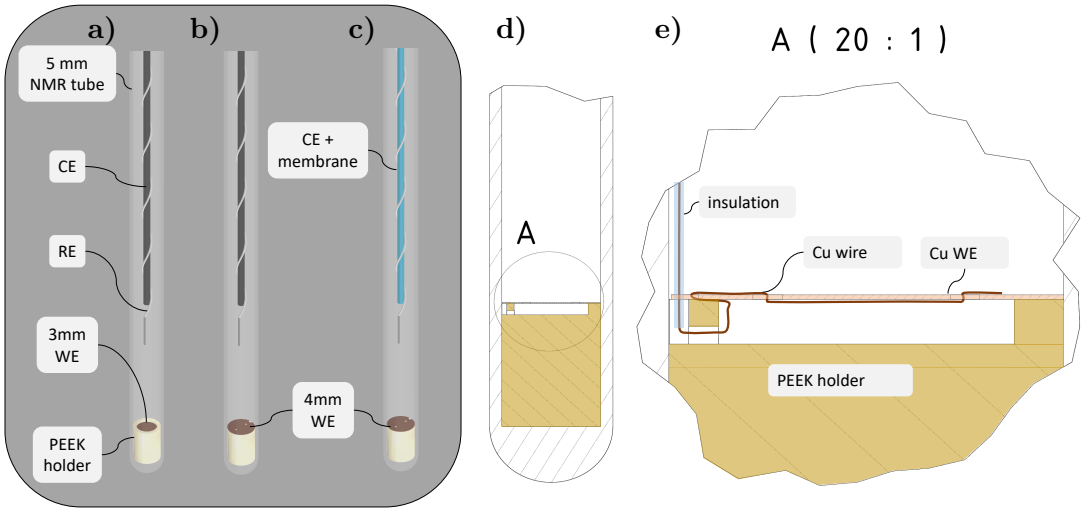

Figure 4.2: (a) – (c) Three cell setups under investigation with 3 mm WE without membrane (setup A), 4 mm WE without membrane (setup B) and 4 mm WE with membrane (setup C), respectively. (d) Section view of the PEEK holder depicting the notch and cavity below the WE for electrical contacting. (e) Detailed view of this section illustrating the wire routing for contacting the WE.

simultaneously contacts it electrically, by being led through two holes in the Cu foil as depicted in the sectional view of the technical drawing in figure 4.2.e. Lastly, the CE is separated in a third cell configuration by a tubular Nafion membrane (Fuel Cell Store, Bryan, USA). This is a typical element in an electrochemical cell with the purpose of preventing products reduced at the WE being reoxidised at the CE. The Nafion tube is sealed using Teflon tape at its open end. In the following, this cell setup is called setup C. To ensure that the 4 mm outer diameter holder fits precisely inside standard NMR tubes, the tapering at the top was removed by shortening the NMR tubes to ca. 130 mm total length. Advantageously, the adjusted position of the WE is parallel to the exciting RF field, which minimises distortions due to eddy currents induced in the conductive WE [62, 67, 74].

4.2.3 Pulse sequences

The pulse sequences for frequency encoded intensity profiles and purely phase encoded Chemical Shift Imaging (CSI) are depicted in figure 4.3.a and 4.3.b, respectively. The frequency encoded imaging pulse sequence is optimised for application on electrochemical cells by using a composite pulse instead of a 180° pulse, consisting of a 90° and a 270° pulse with inverted phase [71]. Gradient length and strength were $t_g = 1.5\,\text{ms}$ and $G = 11.7\,\text{G/cm}$, the echo time was $\tau = 3.7\,\text{ms}$.

To maintain spectroscopic information about the ^{13}C and ^{23}Na resonances, a pure phase encoded CSI pulse sequence using spin echoes and single-point imaging is employed.

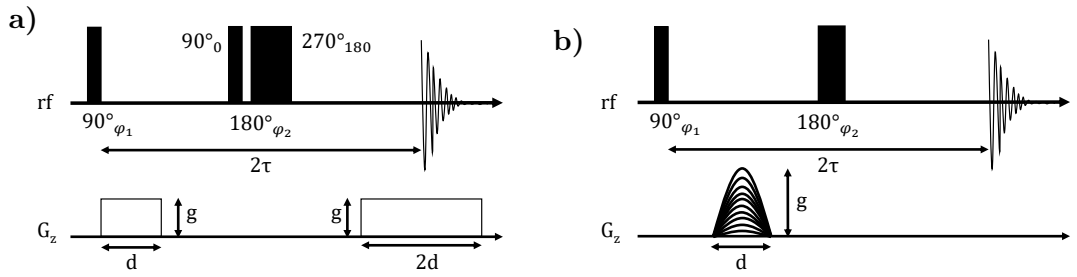

Figure 4.3: Pulse sequences for (a) frequency encoded profile imaging and (b) purely phase encoded CSI.

	d / ms	$t_{g,eff}$ / ms	τ / ms	G_{max} / $\frac{G}{cm}$	ΔG / $\frac{G}{cm}$	t_r / s	t_{aq} / min:s
^{1}H	0.39	0.25	0.65	7.51	0.48	5	10:40
^{13}C	0.12	0.07	0.36	106.73	6.89	9	19:12
^{23}Na	0.39	0.25	0.66	29.88	1.93	0.19	0:48

Table 4.1: Imaging parameters of ^{1}H, ^{13}C and ^{23}Na CSI measurements.

Magnetic susceptibility artefacts can be reduced by applying phase encoded rather than frequency encoded imaging techniques, as well as by increased spatial encoding gradient strengths. Despite its increased acquisition time, single point imaging is advised for short T_2 relaxation times [54]. By using spin echoes, phase errors due to magnetic field inhomogeneities are refocused. Also, the transversal magnetisation relaxes with time constant $T_2 > T_2^*$. However, due to the low sensitivity of ^{13}C measurements, echo times were kept as short as hardware limitations permitted, resulting in minimum echo time and therefore short gradient pulses. This in turn had the advantageous effect of maximising the gradient strength and thus minimising magnetic field artefacts.

A shaped gradient pulse is varied in gradient strength corresponding to 32 points in k-space. Maximum gradient strengths G_{max} and gradient strength differences ΔG were chosen to result in a field of view of 20 mm, cf. table 4.1. The gradient duration for ^{13}C images was $t_g = 0.12$ ms corresponding to an effective duration of $t_{g,\text{eff}} = 0.07$ ms. The echo time was $\tau = 0.36$ ms. The parameter of other nuclei are given in Table 4.1 as well as repetition time t_r and total acquisition time t_{aq}. To set the gradient list, the 'diff' package (version 5) of the software Bruker TopSpin (version 3.6.1, Bruker BioSpin GmbH, Rheinstetten, Germany) was employed.

Binary data from CSI measurements were imported and processed using the Python package 'nmrglue' [99]. All Free Induction Decays (FIDs) were processed with line broadening of 1.5 Hz. Zero filling was applied in the spectral and the spatial dimension to double data points in each dimension. After applying two-dimensional Fast Fourier Transform, the spectra were phase corrected. Here, every individual spectrum of the first image of the experiment of each respective nucleus was manually corrected. The determined phase correction parameter were then applied to all following images of the same nucleus of this

experiment. Peak fitting of the ^{1}H peak of water, the ^{13}C peaks of carbonate and CO_2 and the ^{23}Na peak of Na^+ was performed using Lorentzian shaped functions. In addition to chemical shift, the integral und the Full Width at Half Maximum (FWHM) of each peak at every position on the z-axis, the maximum relative fit error was output. This error was used to identify and remove outliers using a threshold value depending on the quality of the respective signal. The threshold value was 10 % for the ^{23}Na resonance of Na^+, 15 % for the ^{13}C resonance of carbonate and 50 % for the ^{13}C resonance of CO_2.

4.2.4 Validation of adjusted cell designs

In order to investigate the impact of the Cu WE on the B_0 field, ^{1}H, ^{13}C, and ^{23}Na CSI is carried out on cell setup B filled with aqueous 1 M $NaH^{13}CO_3$, both without and with the Cu WE, as depicted in figure 4.4.a and 4.4.b, respectively.

Initially, the ^{23}Na resonance of Na^+ is studied, and the sample without Cu foil is manually shimmed to obtain a relatively narrow Na^+ resonance of ca. 10 Hz. ^{23}Na was chosen as nucleus under investigation, because the broadband coil is optimised in terms of homogeneous B_0 and B_1 field and ^{23}Na offers higher receptivity compared to ^{13}C. Solely introducing the PEEK holder without conductive material resulted in distortions of the magnetic field due to the susceptibility differences. This effect could be mostly corrected by shimming. The resulting spatially resolved ^{23}Na spectra are displayed in figure 4.4.c. Consequently, the maximum variation of chemical shift was limited to approximately 0.05 ppm along the electrolyte-filled volume from -5 to 10 mm. While the shim and position of the PEEK holder and NMR tube relative to the NMR sensitive volume were maintained, the Cu foil was added. As a result, local changes in the water chemical shift were observed, *cf.* figure 4.4.d. figure 4.4.e is a magnification of the same data set representing spectra with $z = [0, 2]\, mm$. In proximity to the electrode, the resonance developed a downfield shifted and an upfield shifted feature. The downfield peak was shifted by ca. 3.5 ppm, while the upfield peak was shifted by ca. 0.5 ppm. With increasing distance to the electrode, the two features converged again to result in the bulk ^{23}Na resonance at approximately 0.45 ppm. Peak splitting and shifting of the same order of magnitude were observed for ^{1}H and ^{13}C measurements of H_2O and carbonate resonances, respectively, indicating that this effect is nucleus independent and can be attributed to magnetic field effects.

FEM simulations using the FEMM software (Version 4.2, David Meeker) were used to confirm this observation. The geometry shown in figure 4.4.b was placed in a homogeneous magnetic field, and the resulting magnetic field distortions were simulated in three dimensions. To compare the results to spatially resolved NMR spectra as presented in figure 4.4.e, histograms were calculated for all voxels in slices of 100 µm thickness in z-direction. These histograms are plotted in figure 4.4.f for $z = [0, 2]\, mm$. Qualitatively, the simulations showed the same local distribution of magnetic field distortions. A splitting of the two features of ca. 4 ppm was determined that decreased to zero within 2 mm along the z-axis. This is in quantitative accordance with experiments. However, the upfield

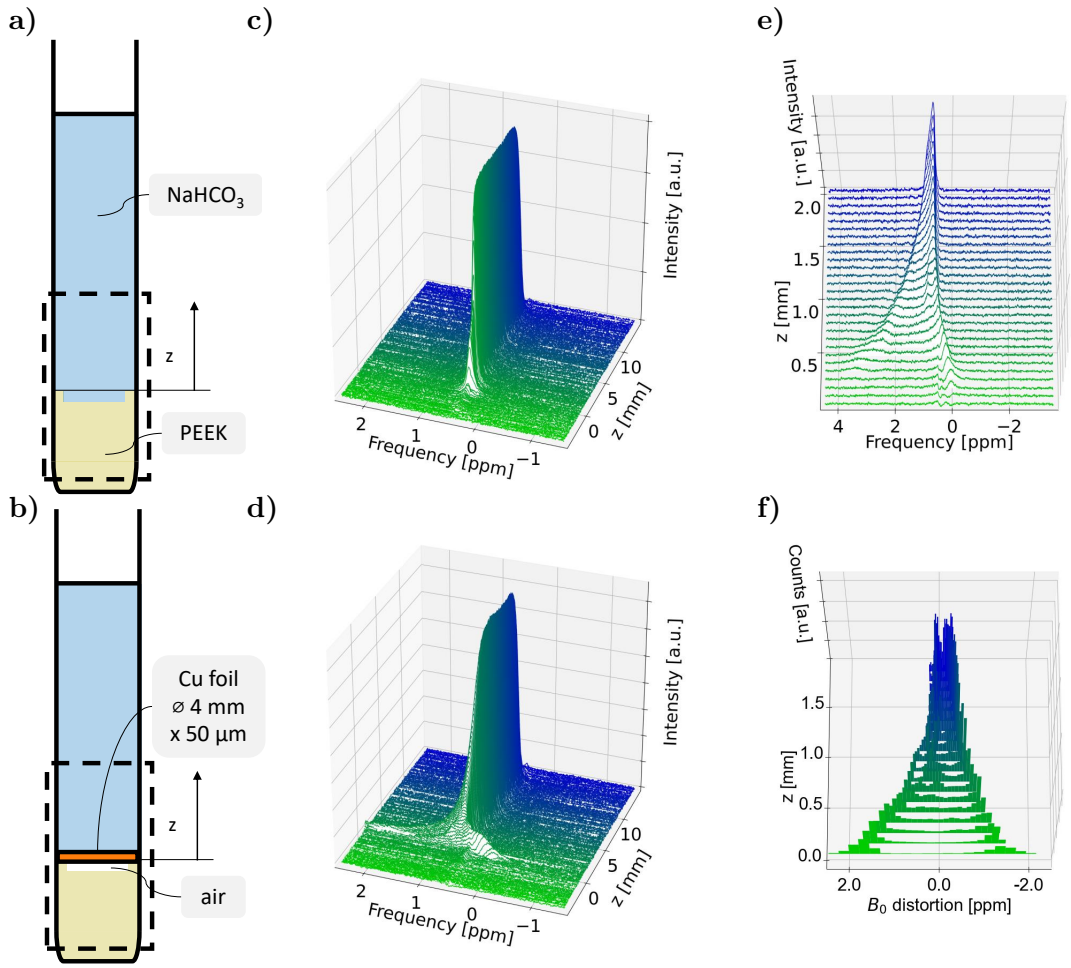

Figure 4.4: Combined experiments and simulations determined the extent of B_0 field distortions due to introduction of a conductive WE into the sensitve NMR volume. (a) – (b) Schematic of the investigated sample with and without Cu WE, respectively, based on cell setup B. (c) – (d) Spatially resolved spectra of the ^{23}Na resonance of Na^+ for samples displayed in a) and b), respectively. (e) Magnification of (d) in the interval $z = [0, 2]\,mm$. (f) Spatially resolved histograms in the interval $z = [0, 2]\,mm$ from Finite Element Method (FEM) simulations of the sample displayed in (b).

peak predicted by simulations was shifted by ca. 2 ppm, while the downfield peak was shifted by ca. 1.9 ppm. Still, this showed that the conducted experiments were capable of demonstrating the influence of the Cu WE on the magnetic field. Remaining discrepancies between experiment and simulation could be explained by additional B_0 distortions due to the air pocket below the Cu foil or imperfect positioning of the WE. Also, the FEM calculations were shown to be suitable to predict magnetic field distortions at conductive material in the NMR sensitive volume and their spatial distribution.

The results from combined experiments and simulations indicated that a conductive electrode in the NMR sensitive volume will induce a systematic error in imaging experiments. By thorough shimming after inserting the full cell setup including all electrodes and

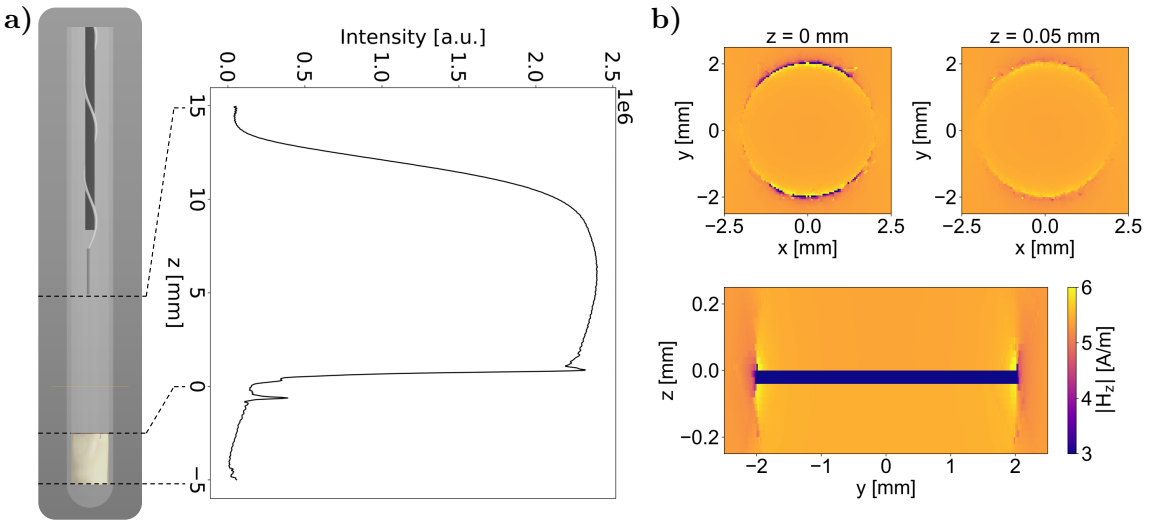

Figure 4.5: Eddy currents induced in the Cu electrode lead to B_1 field distortions. (a) ^{1}H density profile along z-axis recorded using frequency encoded imaging. (b) Top view and sectional view on the B_1 field in terms of the magnitude of RF strength in z-direction around a Cu disc simulated using EMpro.

wires, this error has to be minimised. However, it can not be ruled out that a alteration of chemical shift near the electrode remains. Before every measurement during electrolysis, this initial change of chemical shift has to be determined and, subsequently, be corrected.

Frequency encoded ^{1}H profiles were used to estimate the effect on the B_1 field. The total intensity of ^{1}H density is plotted over the z-axis in figure 4.5.a. A local increase in B_1 field intensity would result in an increased flip angle. Thus, such a locally increased B_1 field was detectable as peak in the ^{1}H profiles if excitation was conducted using a flip angle of less than 90° for the bulk electrolyte. figure 4.5.a shows an exemplary profile of such an image, which additionally illustrates the placement of the cell components relative to the z-axis and the NMR sensitive volume. Here, a pulse length of 16.5 µs was used, while the pulse duration for a 90° magnetisation flip was determined to be 18.5 µs. Close to the electrode at $z = 0\,mm$, an intensity peak was observed. Towards positive z-values the ^{1}H density approaches zero at $z = 15\,mm$, which marks the upper boundary of the sensitive volume. Towards negative z-values low ^{1}H density indicates the position of the PEEK holder that does not yield a comparably high ^{1}H signal intensity as the liquid electrolyte. Residual ^{1}H signal and the peak at ca. $z = -1\,mm$ result from thin films of electrolyte. In figure 4.5.b, the results of three-dimensional B_1 field simulations using EMpro (Version 2020, Keysight Technologies) are illustrated. A Cu disc of 4 mm in diameter and 50 µm thickness, representing the dimensions of the Cu electrode used in the experiments, was placed between two Helmholtz coils for RF excitation. The resulting B_1 field intensities are illustrated in top view on the Cu disc, exactly on top and 50 µm above the surface, as well as in a sectional view through the centre of the disc. On the upper and lower surface of

the Cu disc, B_1 was increased at the edges of the WE about 20 % compared to voxels with larger distance to the disc. This confirms that the increased intensity near the electrode in ^{1}H profiles can be assigned to increased B_1 field in electrode proximity that are caused by eddy currents induced in the electrode. Simultaneously, the distortions in B_1 field extend less than 50 µm into the z-direction and are limited to volumes near the edges of the electrode. This effect has to be considered when experiments are evaluated quantitatively. However, the error due to B_1 field distortions can be estimated to be relatively small.

4.3 Reproducibility measures

To increase reproducibility and comparability to literature studies, preparation of the WE and of the electrolyte were matched with experimental protocol of these studies [27, 31]. Stock solutions of $KHCO_3$ (98 atom-%, Sigma Aldrich Chemie GmbH, Munich, Germany) were treated by preelectrolysis using two Pt mesh electrodes as WE and CE at 0.25 mA/cm² over 16 h under N_2 atmosphere [94], as described in section 3.2.2. Cu WEs were first polished mechanically with 1000-grit sandpaper and rinsed with de-ionised water. After fixing the Cu foil on the PEEK holder, it was electrochemically polished in 85 % concentrated phosphoric acid [100]. For that, the Cu foil was immersed in the acid and used as WE, while a glassy carbon rod was used as CE and Reference Electrode (RE). Cyclovoltammetry (CV) in the oxidative region up to a measured potential of 3 V showed a minimum in the potential region between 2 and 3 V. At this overpotential, a Cu oxide layer forms, which is simultaneously dissolved in the acid. This generates a reproducibly clean and pure Cu surface.

Another error source identified was the use of a pseudo Ag/AgCl RE, which was addressed by determining its potential *vs.* a commercially available Ag/AgCl RE exactly. This potential difference could reproducibly be averaged to 0.1998 V at $T = 10\,°C$. In the following, potentials measured by the pseudo Ag/AgCl RE are converted to Standard Hydrogen Electrode (SHE) or Reversed Hydrogen Electrode (RHE) scale by

$$\begin{aligned} E_{\mathrm{SHE}} &= E_{\mathrm{pseudo-Ag/AgCl}} + 0.4113\,\mathrm{V}\ \text{and,} \\ E_{\mathrm{RHE}} &= E_{\mathrm{pseudo-Ag/AgCl}} + 0.4113\,\mathrm{V} + 0.059 \times \mathrm{pH}, \end{aligned} \tag{4.1}$$

respectively. Moreover, deactivation of polycrystalline Cu electrodes by Ag contamination of the Ag/AgCl RE was reported [98]. Here, a single-junction Ag/AgCl electrode resulted in Ag^+ concentrations in the order of 35 – 50 ppb. It was shown that only 10 ppb Ag^+ ions, which corresponds to 92.7 nM, was enough to severely influence the product selectivity on Cu WE. With a double junction RE this effect could be prevented. However, it was also shown that this has only a significant effect on the product selectivity for long term operations of ca. twelve hours. For less than two hours operation, the influence of single *vs.* double junction RE was not significant and is therefore not further considered in this study, in which the electrolysis duration was 1 h.

A constant potential in the cell presented in chapter 3 was controlled by measuring the potential *vs.* the pseudo-RE and adjusting the applied current, but this approach resulted in poor reproducibility of the resulting evolution of current, as shown by the large error bars in figure 4.6.a. By including the electropolishing preparation step and controlling the current instead of the potential, error bars in the current–voltage characteristics were minimised, as depicted in figure 4.6.b. Additionally, the resulting product distribution, as analysed by ^{1}H NMR, *cf.* figure 4.6.c, showed a clear trend in product selectivity and small error bars, *cf.* figure 4.6.d.

Further preparatory electrochemical experiments were included in the experimental

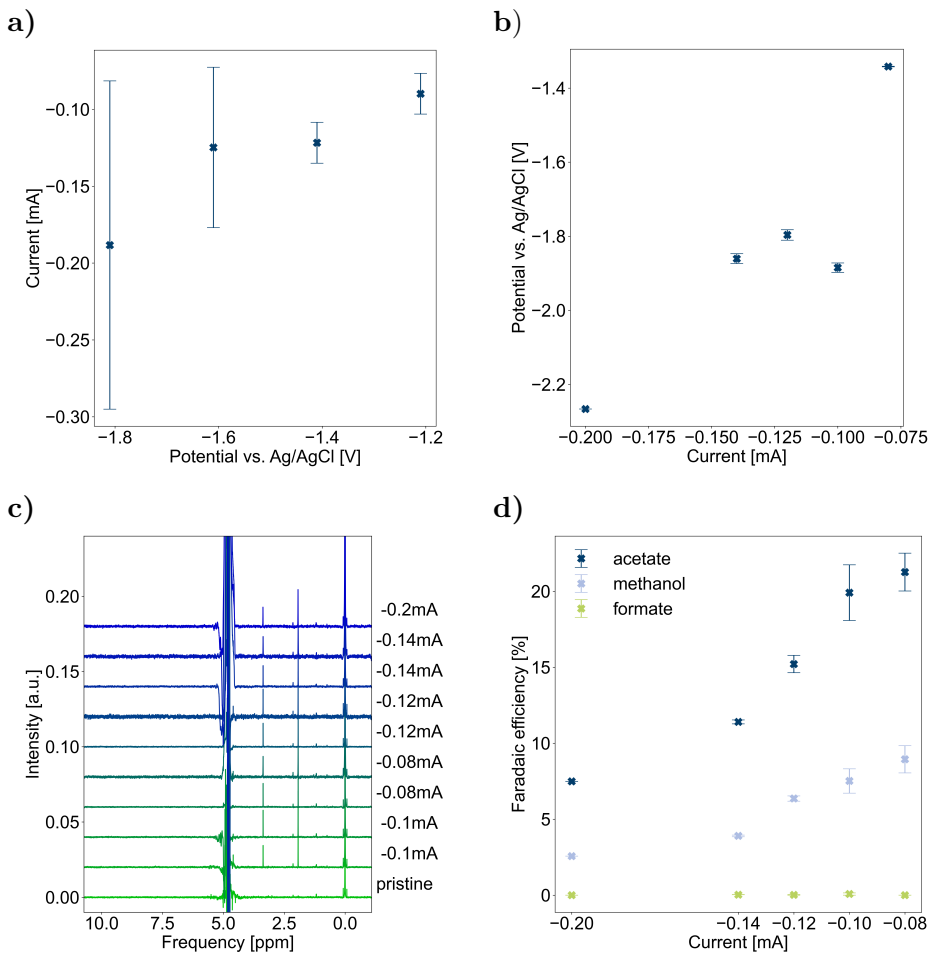

Figure 4.6: Comparison of reproducibility of current–voltage characteristics and product distributions with varying process control and preparation steps. (a) Steady state current measured during electrolysis with controlled potential (Chronoamperometry (CA)) without electropolishing of WE. (b) Steady state potential measured during electrolysis with controlled current (Chronopotentiometry (CP)) with electropolished WE. (c) ^{1}H spectra measured *ex situ* after CP with electropolished WE. (d) Faradaic Efficiencys (FEs) of acetate, methanol and formate formation of CP with electropolished WE. All error bars represent the standard deviations from statistical mean values from repeated experiments.

protocol before and during the *in operando* measurements. Preliminary electrochemical measurements included impedance spectroscopy and CV in the potential range [-0.1,-1.6] V *vs.* RHE for WE surface cleaning, followed by three additional CV cycles in the potential range [-0.1,-1.4] V *vs.* RHE to determine the current–voltage characteristics. From the last CV cycle, the appropriate current for CP under electrolysis conditions was chosen. In between measurements, underpotential CA was applied at -0.1 V *vs.* RHE to maintain the WE under negative potential and prevent Cu surface reoxidation [101]. The entire experimental protocol is depicted in figure 4.7.

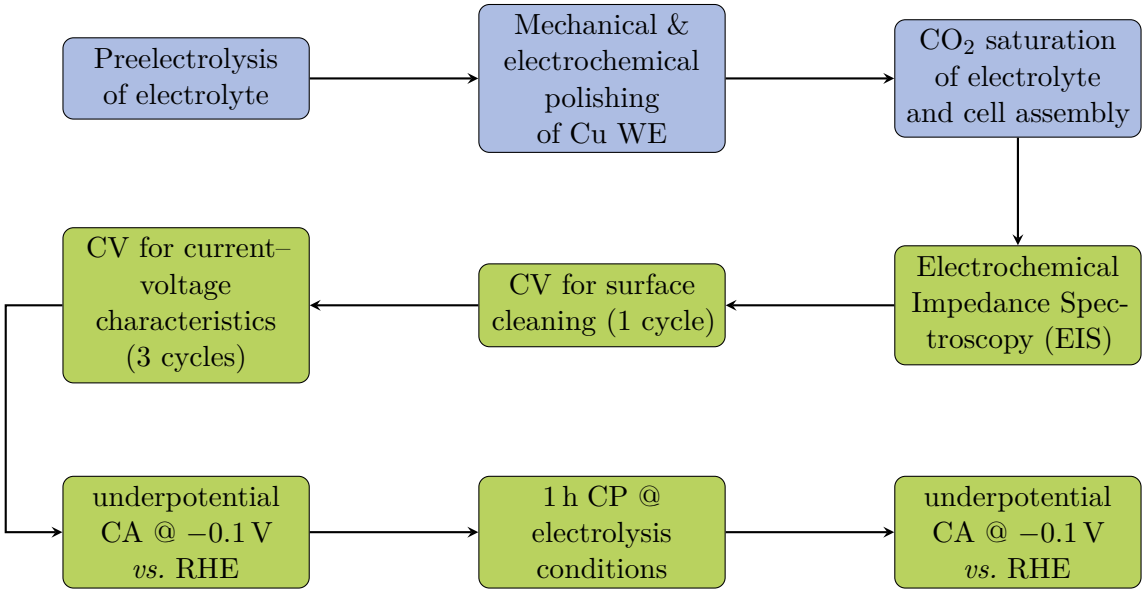

Figure 4.7: Experimental protocol including all preparation steps, represented by blue colour, and the electrochemical experiments, represented by green colour.

4.4 Enhancing bubble detachment

As the majority of products in the presented electrochemical cell is gaseous, either as a result of eCO_2R or Hydrogen Evolution Reaction (HER), gas bubble formation is inevitable. While this can cause distortions in NMR spectra, it was shown in chapter 3 that meaningful information can still be acquired. However, in the adjusted cell setup A, increased bubble attachment was observed in the close electrode proximity. Visual inspection through the glass of the NMR tube during electrolysis revealed that bubbles tend to stay attached at the interface between PEEK holder, glass tube, and electrolyte, as depicted in figure 4.8.a. This was confirmed by frequency encoded ^{1}H profiles acquired during *in operando* measurements, *cf.* figure 4.8.b. Bubbles that were attached to the PEEK/glass interface or to the Polytetrafluoroethylene (PTFE) insulation of the contacting wire were responsible for the intensity drops with round bubble-like shapes. If these bubbles detach shortly after forming, growing and coalescing, they would not significantly impact the NMR measurements that are typically acquired over several minutes. However, the bubbles in this experiment stayed attached for a longer period, so their influence was noticeable in the ^{13}C CSI, *cf.* figure 4.8.c, where the spatial profile of the carbonate resonance integral showed a decreasing course exactly at the described position. Interestingly, attached bubbles also led to decreased chemical shift at these positions, which is unusual since the pH is expected to increase during electrolysis and, therefore, cause an increase in chemical shift. This could be assigned to an additional local B_0 field distortion caused by the large difference in magnetic susceptibility of gas and electrolyte.

Consequently, bubble attachment near the electrode had to be compulsively inhibited. The highly hydrophobic and, therefore, aerophilic surface of the PEEK polymer was

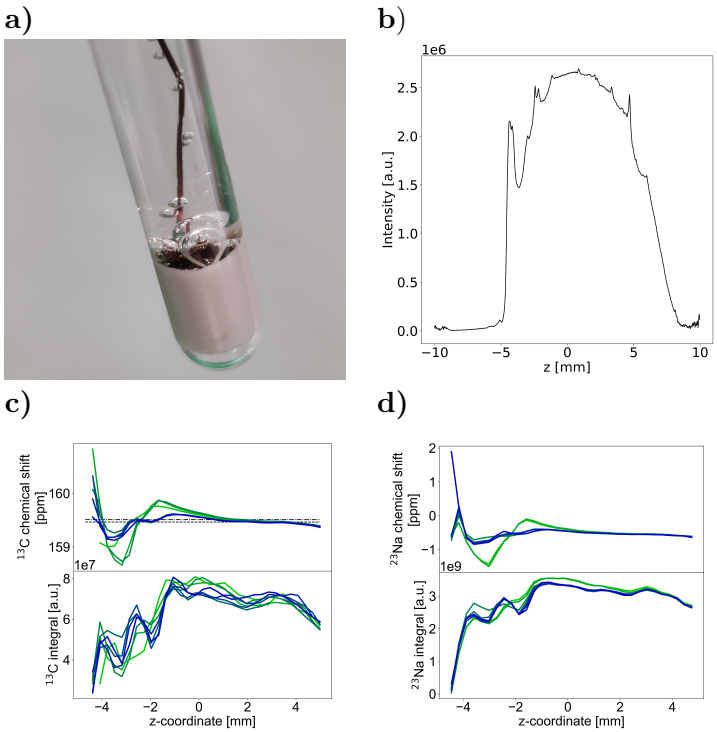

Figure 4.8: (a) Photograph of bubbles attached to the interface between PEEK holder and electrolyte. (b) ^{1}H intensity profile along z-axis recorded by frequency encoded imaging after electrolysis. (c) Chemical shift and integral of ^{13}C resonance of carbonate as a function of z recorded by phase encoded CSI after electrolysis. (d) Chemical shift and integral of ^{23}Na resonance of Na^{+} as a function of z recorded by phase encoded CSI after electrolysis.

accountable for the increased bubble attachment. By manipulating the surface of the holder by, for example, sulphonating the PEEK surface, bubble detachment could be improved [102]. Other methods such as the application of ultrasonic vibration, a supergravity field, or a strong magnetic field inducing magnetohydrodynamic (MHD) effects could also be used and enhance bubble detachment [103]. The latter is an integral part of *in operando* NMR measurements anyway, which can not be turned off. Still, bubbles were observed *in operando* despite this effect.

While all these measures only mitigate the bubble attachment, they can not completely inhibit this effect. Consequently, the contact of the PEEK holder with the electrolyte was entirely prevented by increasing the electrode surface to 4 mm in diameter and placing the electrode on top of the holder, *cf.* cell setup B in figure 4.2.b. The missing fixation inside the PEEK holder was solved by the wire contacting displayed in figure 4.2.e. The improved bubble detachment is illustrated by the evolution of potential during CP, where the potential during electrolysis with cell setup A, depicted in figure 4.9, showed regular sudden jumps to less negative values, indicating the detachment of bubbles covering a large surface of the working electrode. In contrast, potential jumps were not observed with cell setup B anymore. Instead, only noise of smaller extent is noted in the potential transient,

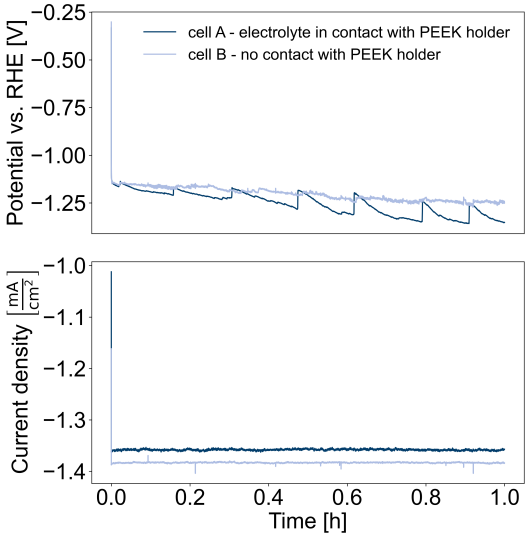

Figure 4.9: Comparison of potential *vs.* RHE and current density during CP under electrolytic conditions with cell setup A, where the electrolyte is in contact with the PEEK holder and, therefore, bubbles stay attached, and cell setup B, where this contact is inhibted. A constant current was chosen to approximate a potential of $-1.2\,\mathrm{V}$ *vs.* RHE.

indicating smaller bubbles that detach more easily. This way, the desired potential of $-1.2\,\mathrm{V}$ *vs.* RHE could be achieved more steadily with cell setup B. The current density could be controlled constantly in both cases. The required current density to result in the desired potential was ca. $-1.35\,\frac{\mathrm{mA}}{\mathrm{cm}^2}$.

4.5 Application of an ion exchange membrane

Effective separation of the CE compartment from the rest of the cell was addressed by the approaches depicted in figure 4.10. The first approach in figure 4.10.a was a carbon rod CE spray coated with Nafion suspension. During the drying process, the Nafion layer cracked open and did not cover the graphite rod completely anymore. Thus, this approach is not investigated further.

Another approach involved a platinum wire inside a glass capillary, *cf.* figure 4.10.b. Here, a flat cation exchange membrane was applied to one end of the capillary by heating the capillary with a heat gun and then pressing the flat membrane against the heated glass. This resulted in plastic deformation of the membrane, sealing the capillary tightly. Inside the capillary, $KHCO_3$ electrolyte was introduced by a syringe, and the Pt wire was wrapped into the capillary to maximise the electrochemically active area. The membrane was additionally fixed by PTFE tape. However, electrochemical measurements were interrupted shortly after the start, possibly due to gas bubbles that could not rise up the electrolyte due to confined space or because the exchange area of the membrane was small compared to the WE. Therefore, this CE approach was also not further investigated.

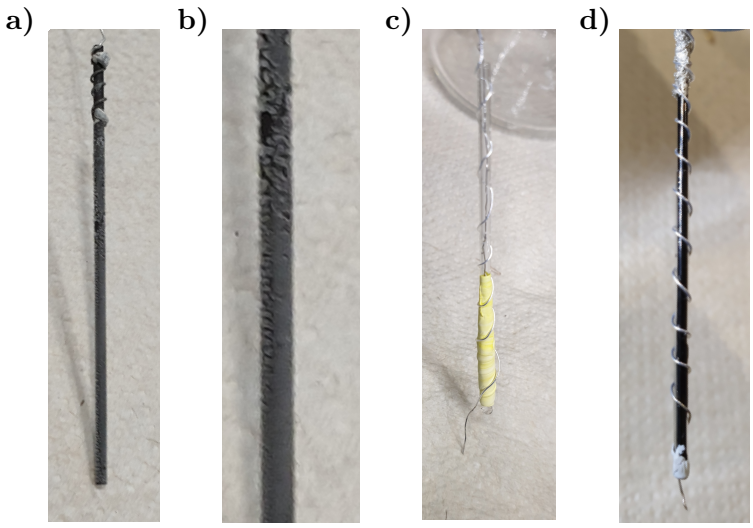

Figure 4.10: Various approaches of implementing a membrane in the electrochemical cell. (a) Graphite rod coated with Nafion suspension. (b) Magnified view of Nafion-coated graphite rod shows exfoliation of the coating after drying. (c) Pt wire CE in a capillary separated by planar ion exchange membrane. (d) Glassy carbon rod in a tubular Nafion membrane, sealed with PTFE tape.

Lastly, a tubular shaped Nafion membrane that fitted precisely on a 1 mm outer diameter glassy carbon rod was tested. No gap or liquid electrolyte was left between the membrane and CE. The open end of the membrane at the bottom of the electrode could be sealed by PTFE tape. With this configuration, electrolysis could be carried out without interruptions and resulted in a stable potential. The results of this CE/membrane combination will be evaluated in the following regarding product distribution during eCO_2R as part of cell setup C.

4.6 Evaluation of reproducibility measures

In order to test the reproducibility of electrochemical experiments and the product outcome of eCO_2R, a potential study was carried out using 0.1 M $KH^{12}CO_3$ and comparing cell setups A, B, and C. The experimental protocol used in the experiment are depicted in figure 4.7. The current–voltage characteristics of the CV experiments were used to determine the current required to result in the potential range $E_{pseudo-Ag/AgCl} = [-1.2, -1.4, -1.6, -1.8, -2.0, -2.2]$ V or $E_{RHE} = [-0.4, -0.6, -0.8, -1.0, -1.2, -1.4]$ V, respectively.

The resulting CP transients for the three respective cell setups A, B and C are depicted in figure 4.11.a, 4.11.c and 4.11.e, respectively. The potentials of each measurement were averaged and plotted against current density for the three measurement series in in figure 4.11.b, 4.11.d and 4.11.f, respectively. Stable courses of potentials were recorded in all cases with various extents of fluctuations. The current–voltage plots confirm the

exponential characteristic measured by CV experiments. The three measurement series are quantitatively in accordance. Therefore, the plot in figure 4.11.g depicts the averaged data of the three measurement series. figure 4.11.h shows the averaged values considering all experiments, which resulted in error bars smaller than ca. 0.3 $\frac{mA}{cm^2}$ or ca. 0.15 V, respectively.

The formation of products in these electrolysis experiments was analysed using ^{1}H NMR with water suppression, as described in chapter 3. The resulting concentration and FEs of liquid products, such as ethanol, acetate, acetone, methanol and formate, as well as dissolved methane are depicted in figure 4.12.a-c and 4.12.d-f, respectively. In general, FE in all cell setups was highest for all products at potentials below -1 V *vs.* RHE. Overall, the highest FEs were found for acetate and formate, while acetate and acetone dominated in setup A, acetate and formate in cell setup B, and formate in cell setup C. Comparing cells B and C with and without membrane, respectively, the proposed increase in anionic products, *i.e.* formate and acetate, was not observed. The acetate FE was even lower for setup C, and formate was almost equal, except at the lowest measured potential. This points towards the fact that the anionic species were not reoxidised at the CE without a membrane. Still, cell setup C is proven to be suitable for the eCO_2R, and the product distribution does not differ largely from cell setup B without a membrane.

Results are only partly in accordance with literature. The same liquid species as presented by Kuhl *et al.* could be identified [31]. But the FE for ethanol was lower, while for acetate, acetone, and acetaldehyde it was higher compared to literature. Also, the potential dependence is shifted towards lower potentials. The reasons for these disparities were mainly due to significant differences in the cell configurations. The presented *in operando* NMR cell was tailored for application in a standard NMR probe and was not optimised for electrolysis operation in the first place. Especially the mass transport conditions vary widely from the flow cell that was used by Kuhl *et al.* [31]. If CO_2 is not continuously supplied to the electrode/electrolyte interface (EEI), a scarcity in the reactant could occur and alter the reaction environment at the WE. For a system that is apparently depending largely on local reaction conditions, such as the eCO_2R, a variation of product distribution in the *in operando* NMR cell compared to an electrolysis cell was therefore expected. While a flow cell setup would describe a real electrolysis application more precisely, the presented static approach is sufficient to determine mechanistic processes and kinetics.

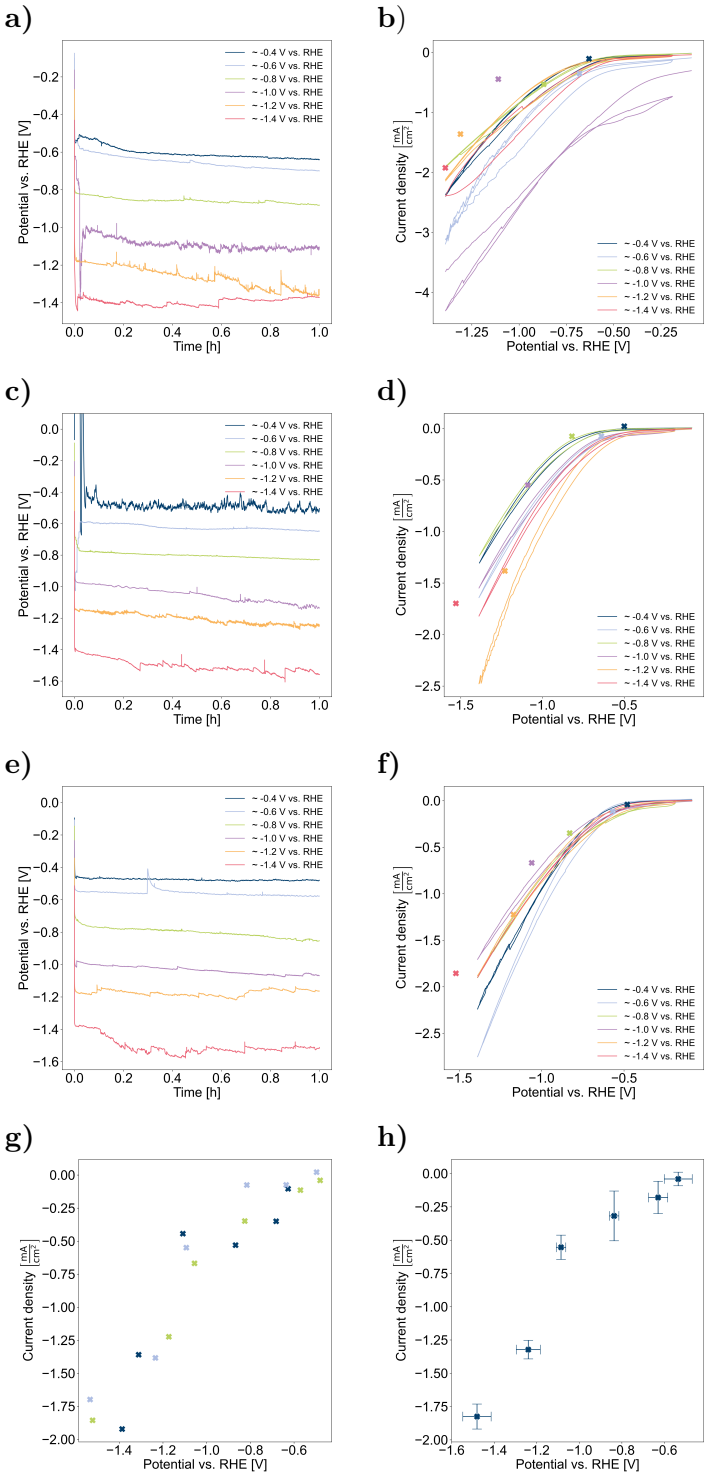

Figure 4.11: Continued on next page.

Figure 4.11: Overview of electrochemical performance of cell setups A, B and C. The evolution of potential during CP experiments resulting approximately in the potential interval $E_{RHE} = [-0.4, -0.6, -0.8, -1.0, -1.2, -1.4]\,\mathrm{V}$ are depicted in (a), (c) and (e) for cell setups A, B and C, respectively. The CVs recorded before the respective CP experiments are depicted in (b), (d) and (f) for cell setups A, B and C, respectively. The average potential during the subsequent CP at constant current density is depicted by a cross symbol of the respective colour. (g) Overview of current–voltage characteristics of CP experiments with cell setups A, B and C are represented by dark blue, light blue and green colour, respectively. (h) Current–voltage characteristic considering measurements with all three cell setups are averaged and error bars are given for potential and current density.

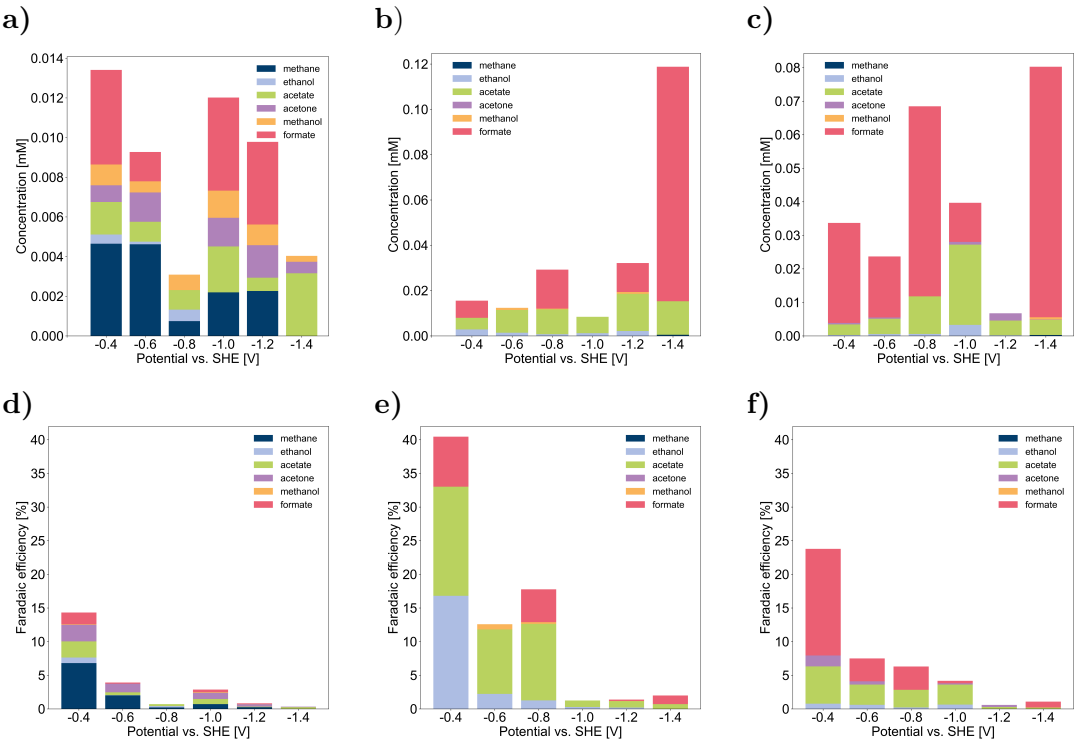

Figure 4.12: Overview of *ex situ* product analysis after CP in the potential interval $E_{RHE} = [-0.4, -0.6, -0.8, -1.0, -1.2, -1.4]\,\mathrm{V}$ using cell setup A, B and C. The liquid products ethanol, acetate, acetone, methanol and formate as well as dissolved methane were considered. The measured concentration for these products are depicted in (a), (b) and (c) for cell setups A, B and C, respectively. The FEs these products are depicted in (d), (e) and (f) for cell setups A, B and C, respectively.

4.7 Conclusion

In this chapter, various electrochemical cell components and methods were presented and evaluated that enable the measurement of spatially resolved CSI experiments on eCO_2R. By using CSI and frequency encoded 1D profiling, it was possible to visualise the impact of the cell setup on B_0 and B_1 field distortions and classify their extent as relatively small or capable of being minimised with good shimming. Additionally, a protocol for electrochemical experiments was introduced and found to be effective in preparing *in operando* electrolysis experiments. The WE setup of cell B was determined to be the most advantageous for inhibiting bubble attachment in electrode proximity, and all three cell setups were shown to exhibit similar and reproducible electrochemical behaviour during potential-dependent measurement series. Even though the product distributions between the measurement series varied slightly, the tubular membrane was proved to work reliably and eCO_2R is not severely influenced by introducing an ion conductive membrane into the cell. Overall, these findings provide a foundation for further spatially resolved NMR investigations on eCO_2R.

4.8 Postface

The main part of this work was performed and researched by the author of the thesis, in particular:

1. The development and construction of the *in operando* cell holder, the cell setup and the shielding cap.
2. The implementation and testing of imaging pulse sequences.
3. The conduction of CO_2 electrolysis experiments *ex situ* and *in operando*.
4. The processing and analysis of all electrochemical experiments.
5. The processing and analysis of all NMR experiments

Minor parts of this work were performed with assistance of the following co-workers:

1. The conduction of CO_2 electrolysis experiments and construction of CEs separated by a membrane were assisted by Johannes Kochs (IEK-9, Forschungszentrum Jülich GmbH, Germany).

Minor parts of this work were performed by the following co-worker:

1. The simulations of B_0 and B_1 field were conducted by Matthias Streun (ZEA-2, Forschungszentrum Jülich GmbH, Germany).

Chapter 5

Interplay of local pH and cation hydrolysis during electrochemical CO_2 reduction visualised by *in operando* chemical shift resolved Magnetic Resonance Imaging

5.0 Preface

This chapter is based on the open access publication

Interplay of local pH and cation hydrolysis during electrochemical CO_2 reduction visualized by *in operando* chemical shift resolved Magnetic Resonance Imaging,

by Michael Schatz (corresponding author), Johannes Kochs, Sven Jovanovic, Rüdiger-A. Eichel and Josef Granwehr, published in *The Journal of Physical Chemistry C* (2023), Volume 127, Number 38 (2023).

5.1 Introduction

The evaluation of the three cell setups presented in figure 4.2 has shown that all setups could be utilised for spatially resolved Chemical Shift Imaging (CSI) measurements despite distortions of B_0 and B_1 field, while setup B minimises attachment of gas bubbles in the sensitive Nuclear Magnetic Resonance (NMR) volume. In this chapter, *in operando* measurements will consequently be conducted on cell setup B to investigate various electrolytes and their impact on electrochemical Carbon Dioxide Reduction (eCO_2R).

The eCO_2R by elemental copper shows the unique capability to catalyse the formation of short-chain hydrocarbons that can be utilised as fuels or base chemicals [29, 31]. As industrial application of this process may foster the storage of intermittent renewably generated power, intense research efforts over the last decade aimed to improve catalyst materials in terms of activity and product selectivity. However, recent studies state that local reaction conditions at the electrode/electrolyte interface (EEI) play a decisive role in optimising catalysis of eCO_2R and, therefore, highlight the importance of engineering not only the electrode but also the electrolyte [36–38, 104, 105].

The influence of local pH in electrode-proximity has been demonstrated in the course of the pioneering work of Hori *et al.* [106]. In general, increased local pH induced by consumption of H^+ at the electrode shifts selectivity towards C_{2+} products [11]. On the one hand, the rate limiting step in the reaction pathway to C_{2+} products, *i.e.* the C–C bonding reaction, is pH independent, which advantages these pathways over the formation of products that include a proton transfer in their rate limiting step, such as methane [11, 106]. At the same time, the competing Hydrogen Evolution Reaction (HER) is suppressed under proton depletion [36, 107]. As a consequence of increased pH near the Working Electrode (WE), the solubility of the reactant CO_2 is decreased [29]. Here, the importance of bicarbonate electrolytes in eCO_2R becomes evident. The conversion of CO_2 to HCO_3^- is inhibited if bicarbonate is already present in the electrolyte [108]. At the same time, bicarbonate acts as CO_2 storage. Dunwell *et al.* proved that for a H-type electrolysis cell, the primary carbon source of eCO_2R was not from direct supply of gaseous CO_2 but rather from the accelerated equilibrium between HCO_3^- and dissolved CO_2(aq) [35].

Besides local pH effects, the impact of metal cations has been discussed recently as an integral part of the Electrical Double Layer under negative potential [36, 109, 110]. Generally, improved activity and selectivity for multi-carbon products of eCO_2R were observed with increasing cation size [43, 45, 111]. This was first explained by an increased potential at the outer Helmholtz plane due to enhanced specific adsorption and steric effects of larger cations [43]. However, these findings could not explain the improved eCO_2R performance to the extent observed experimentally [36]. Another mechanism was proposed by Resasco *et al.* who combined Density Functional Theory (DFT) calculations with electrolysis experiments under exclusion of mass transport limitation. They discovered that crucial surface intermediates of C_{2+} products are stabilised by the electrostatic field of these hydrated cations in the outer Helmholtz plane [45]. A more recent study by Koper

et al. attributes an even more substantial role to this stabilising effect of metal cations by showing that the eCO_2R was entirely suppressed in the absence of metal cations [42]. Singh *et al.* bridged between cation induced effects and impact of local pH by suggesting a buffering effect of cation hydrolysis [111]. The hydration shell of a metal cation, M^+, is dehydrated according to the buffer reaction,

$$\left[M^+ (H_2O)_n\right] + H_2O \rightleftharpoons \left[MOH (H_2O)_{n-1}\right] + H_3O^+ . \tag{5.1}$$

With increasing cation size, the pK_a value of the reaction in equation 5.1 decreases due to increased electrostatic interaction between the cation hydration shell and the cathode and, therefore, increases the buffer capacity in the near-neutral pH region [111]. This effect was confirmed experimentally by local pH measurements using *in operando* methods, *i.e.* measurements performed under true catalytic conditions [44, 110]. The magnitude of the buffering effect proposed by Singh *et al.* was found to be overestimated [44]. Here, increasing local pH values could be correlated with increasing cation size. The actual transformation of the hydration shell of metal cations has not been directly demonstrated. Also, there is a point of contention raised by Malkani *et al.* who measured decreasing local CO_2 concentrations with increasing cation size by using *in operando* infrared spectroscopy. This contradicts the assumption of enhanced buffer capacity [112].

To gain insight into the contribution of the proposed mechanisms on the cation effects promoting eCO_2R, advanced *in operando* methods are needed to investigate the EEI more profoundly, especially in terms of the formation of valuable C_{2+} products [36, 38]. However, investigating the impact of a single variable in this system is challenging, as variables interact with each other. [38] An *in operando* method is required that is capable of simultaneously measuring the local pH, the local CO_2 concentration, and the state of hydration of metal cations.

Spatially resolved or surface sensitive pH measurements in electrochemical cells for eCO_2R have been approached by various *in operando* techniques [42]. Voltammetric microelectrodes [113, 114] can obtain a high spatial resolution and fast response in a large pH region, but have to be positioned close to the electrode and therefore influence the local reaction environment. Optical methods, such as Raman and infrared spectroscopy, are powerful non-invasive techniques for investigations of small sample volumes [91, 92]. Especially, surface-enhanced Raman spectroscopy can be useful to determine the pH at the EEI based on the HCO_3^-/CO_3^{2-} equilibrium. However, this technique can be limited in spatial resolution and the detectable pH region [42]. Fluorescence microscopy can achieve an extremely high spatial resolution, enabling pH measurements in cracks within a Gas Diffusion Electrode (GDE) for eCO_2R [115]. A fluorescent agent has to be added to the electrolyte, though, which is an additional variable influencing the local environment. Lu *et al.* presented the only study to the authors' knowledge that measured local pH gradients as a function of distance to the WE, which was a GDE in a flow cell that is optically accessible from one side [116]. Micro-area Raman spectroscopy is applied to determine the

HCO_3^-/CO_3^{2-} equilibrium in a 1 M KOH electrolyte that is used to determine the local pH profile. However, the measurements showed poor quality in close electrode-proximity, so the data was extrapolated to this area. Also, the amount of dissolved CO_2(aq) could not be determined, and was, therefore, calculated using theoretical considerations.

In this chapter, a method is presented that addresses these challenges by employing *in operando* NMR and Magnetic Resonance Imaging (MRI) techniques. Hereby the ^{13}C and ^{23}Na resonances of bicarbonate electrolyte are assessed in terms of the local chemical environment at a Cu WE. The pH determination method presented in chapter 3 is extended by the application of MRI pulse sequences while maintaining spectroscopic information. The ^{13}C measurements are thereby spatially resolved, enabling to observe the evolution of the concentration profiles of the HCO_3^-/CO_3^{2-} equilibrium as well as of dissolved CO_2(aq), which are then utilised to determine the local pH profiles. ^{23}Na images are acquired alternatingly with ^{13}C when using $NaHCO_3$ electrolytes to study changes in the chemical environment of Na^+ cations. By comparing $NaHCO_3$ with $KHCO_3$ electrolyte of varying concentrations, the influence of buffer capacity and cation size are discriminated.

5.2 Experimental Methods

The experimental *in operando* NMR setup including shielding, grounding and filters were used as depicted in figure 2.11. The electrochemical cell in a 5 mm NMR tube was setup B that was presented and discussed in chapter 4. It is depicted in figure 5.1.a with its cell holder, which was tailored for application in a Bruker DiffBB broadband gradient probe utilised on a Bruker Avance III HD spectrometer (Bruker BioSpin GmbH, Rheinstetten, Germany). It is operated within a 14.1 T wide-bore magnet and allows for the generation of magnetic field gradients along the longitudinal axis of the NMR tube. The holder of the Cu WE made of polyether ether ketone (PEEK) is illustrated as technical drawing in figure 5.1.b, which also shows the routing of the contacting wire. This cell design was proven to inhibit contact of the aerophilic PEEK surface with the electrolyte that would otherwise favour bubble adhesion in the sensitive NMR volume.

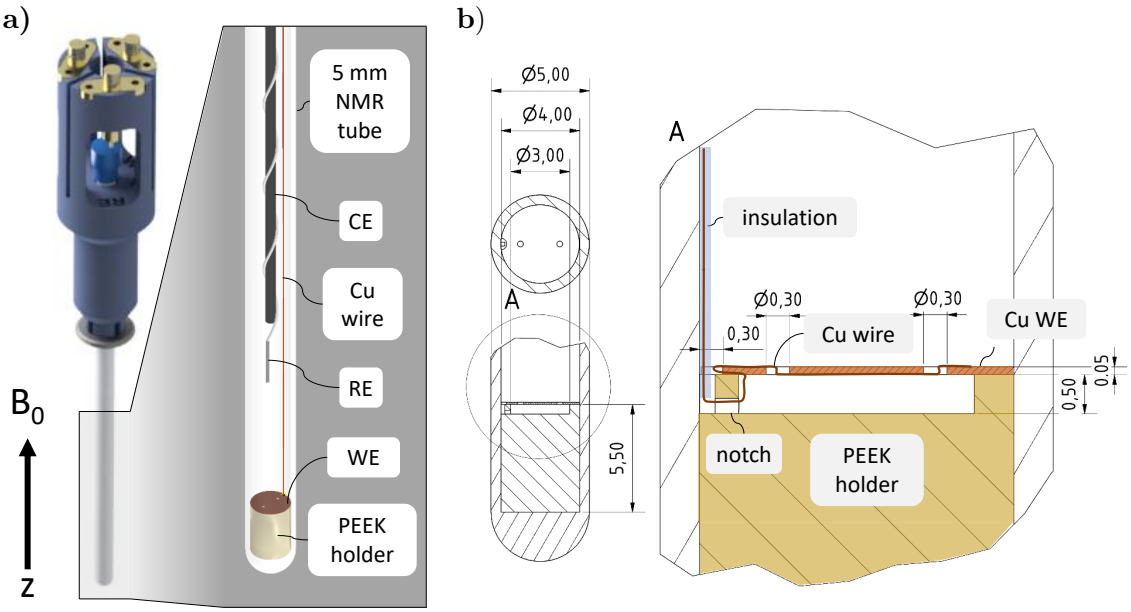

Figure 5.1: Electrochemical cell in a standard 5 mm NMR tube. (a) 3D model of NMR tube in 3D-printed sample holder with detail view of the inside of the cell, including WE, Reference Electrode (RE) and Counter Electrode (CE); (b) Technical drawing of the sectional top and side view of the PEEK holder for the WE with a detail view showing the route of the contacting Cu wire.

1 M stock solutions of ^{13}C enriched $NaHCO_3$ and $KHCO_3$ (98 atom-%, Sigma Aldrich Chemie GmbH, Munich, Germany) were treated by preelectrolysis [94] and electrodes were polished mechanically and electrochemically [100], as described in section 4.3. These treatments conformed with relevant studies in this field [27, 31] and were demonstrated to improve reproducibility of electrolysis experiments in the *in operando* NMR cell, as shown in chapter 4. The WE was inserted into the NMR tube, then 500 µL of electrolyte diluted to the desired concentration of 1 M, 0.5 M and 0.1 M were filled in. The solution was

then bubble saturated at 10 °C with ^{13}C enriched CO_2 (> 97 atom-%, CortecNet, Les Ulis, France). A glassy carbon rod (HTW GmbH, Thierhaupten, Germany) was introduced as CE and a chlorinated silver wire served as RE. CE and RE were placed in the tube above the NMR-sensitive volume in order to minimise distortions of the Radio Frequency (RF) pulse. The tube is closed with a PE cap and sealed with Parafilm. The contacting wires were connected to the respective electrode of the potentiostat via SMA connectors at the top of a dedicated sample tube holder. Finally, the cell was introduced into the NMR probe that was pre-chilled at 10 °C. The tube was placed that the WE was located 5 mm below the centre of the sensitive volume of the detection coil in the probe.

The protocol used for electrochemical experiments before and during the *in operando* measurements is illustrated in Figure 5.2. Initial electrochemical treatments impedance spectroscopy, Cyclovoltammetry (CV) for surface cleaning of the WE and three additional CV cycles to determine the current–voltage characteristics, as described in chapter 4.3. Reading the last CV cycle, the current strength that is applied during Chronopotentiometry (CP) is selected to result in electrolysis condition at ca. −2.2 V *vs.* Ag/AgCl, *i.e.* ca. −1.4 V *vs.* Reversed Hydrogen Electrode (RHE). In between each measurement, underpotential Chronoamperometry (CA) was applied at −0.9 V *vs.* Ag/AgCl, corresponding to ca. −0.1 V *vs.* RHE. This was implemented to maintain the WE at a negative potential and, consequently, prevent the re-oxidation of the Cu surface [101].

Before shimming, ^{1}H profiles were recorded using a frequency encoded pulse sequence optimised for imaging of electrochemical cells [71] to check whether the sensitive volume is bubble-free. To acquire spatially resolved ^{13}C and ^{23}Na NMR spectra, purely phase encoded CSI along one spatial dimension was applied. Details on these pulse sequences are provided in section 4.2.3. The full code of the CSI pulse sequence for Bruker Topspin is available in section A of the appendix.

Long T_1 relaxation times of the ^{13}C resonance of CO_2 on the order of 10 to 20 s led to a trade-off between experiment time and CO_2 sensitivity. As CO_2 was consumed during the reaction, the signal intensity decreased below the detection limit. Complete relaxation would have required a repetition time of 50 to 100 s, resulting in total experiment duration for the ^{13}C image on the order of hours. As such experiment duration would rule out observations of dynamic changes in the electrolyte, the repetition time was set to 9 s, hence the experiment time with 32 k-space points and a four-step phase cycle was 19 min.

To correct for intensity errors of the CO_2 and coalesced HCO_3^-/CO_3^{2-} resonances, T_1 was measured before each step in the *in operando* measurements, *cf.* Figure 5.2, and corrected accordingly for the pH evaluation. The ratio of acquired signal s to maximum signal s_0 can be described by repetition time t_r and relaxation time T_1,

$$\frac{s}{s_0} = 1 - e^{-\frac{T_r}{T1}} . \tag{5.2}$$

Therefore, the measured integrals s_{measured} for the carbonate and CO_2 peaks can be

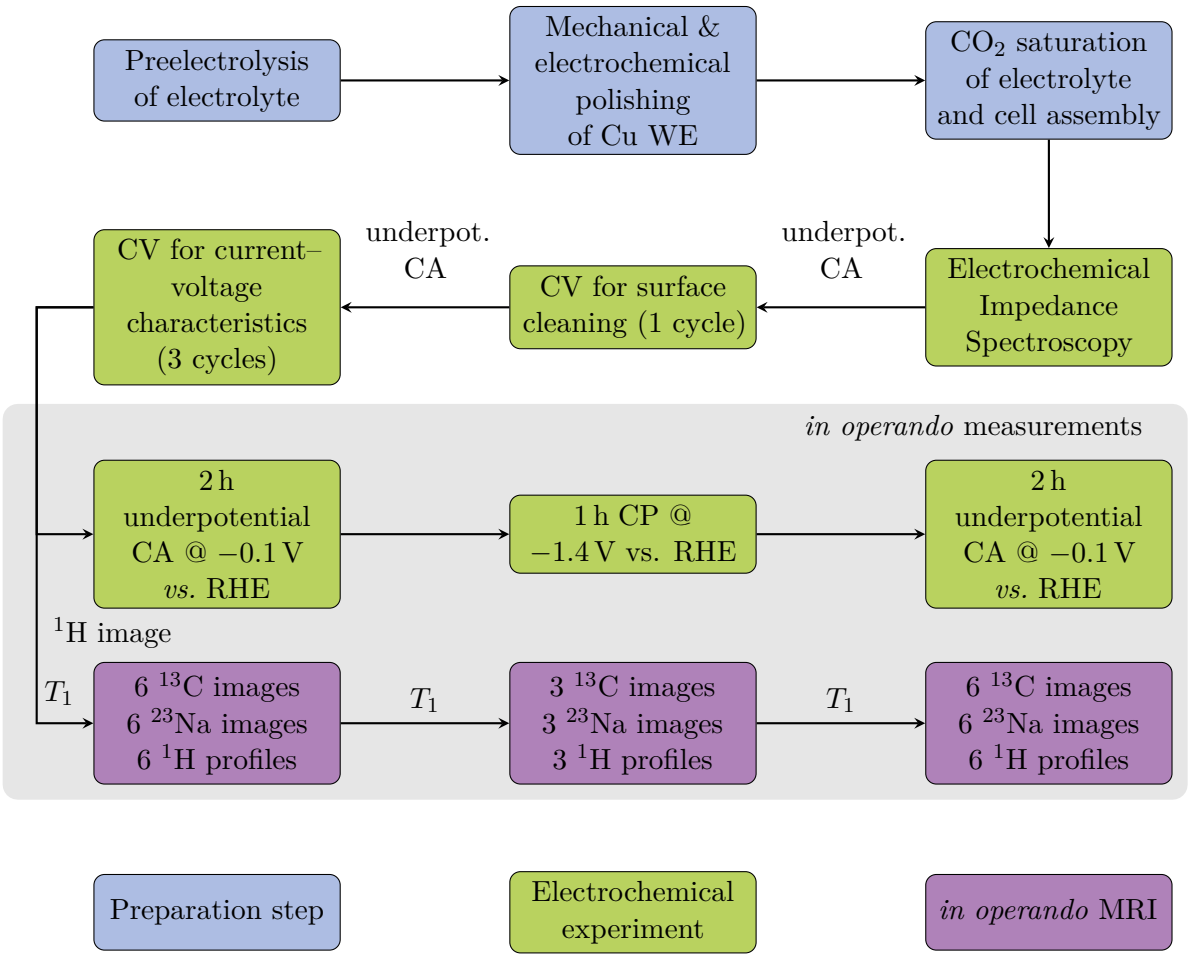

Figure 5.2: Experimental protocol including all preparation steps, the electrochemical experiments conducted before and during *in operando* measurements as well as all NMR and MRI experiments. Electrical Impedance Spectroscopy measurements were utilised to inspect electrical connections within the setup. ^{1}H images were acquired at the beginning of *in operando* measurements. "T_1" marks T_1 measurements of the ^{13}C resonances in the experimental protocol that were used to correct ^{13}C signal intensities.

corrected with this factor,

$$s_{\text{corrected}} = \frac{s_{\text{measured}}}{1 - e^{-\frac{T_r}{T1}}} \,. \tag{5.3}$$

The T_1 relaxation was measured during the *in operando* measurements. An overview about the values are given in table 5.1.

The ^{23}Na nucleus typically relaxes significantly faster. Repetition times of less than 0.2 s were sufficient and a ^{23}Na image was acquired within 48 s. Therefore, the combined experiment duration of a ^{13}C and a ^{23}Na image was approximately 20 min, concerning varying duration of the automatic tuning and matching that was typically conducted within ca. 30 s.

After setting up all NMR parameters and a bubble-free sensitive volume was ensured, a ^{1}H CSI image was acquired as reference. The *in operando* measurements started with 2 h

		Before CA		Before electrolysis		After electrolysis		After CA	
	cation	carb.	CO_2	carb.	CO_2	carb.	CO_2	carb.	CO_2
0.1 M	Na^+	9.3	21.19	10.62	17.66	14.19	–	14.45	13.4
0.5 M	Na^+	6.82	19.19	7.31	12.6	7.1	–	7.05	–
1 M	Na^+	2.43	9.19	3.3	2.83	3.94	–	3.85	–
0.1 M	K^+	11.81	25.14	13.1	22.52	16.92	22.31	16.22	22.86
0.5 M	K^+	2.43	13.99	2.66	10.94	3.57	–	3.91	–
1 M	K^+	10.32	9.5	12.27	9.45	13.2	–	12.19	–

Table 5.1: T_1 relaxation times of the ^{13}C carbonate and CO_2 resonances measured before underpotential CA at the beginning of the *in operando* measurements, before and after the electrolysis, and after underpotential CA at the end of the *in operando* measurements for all investigated electrolytes. All values are given in seconds.

of underpotential CA at $-0.1\,V$ *vs.* RHE, during which six ^{13}C images were acquired. In case of $NaHCO_3$ electrolyte, additional six ^{23}Na images were recorded alternately. Between these measurements on varying nuclei using the same broadband channel of the probe, the resonator circuit was automatically tuned and matched to the Larmor frequency of the respective nucleus. Additionally, before every ^{13}C image, a frequency encoded ^1H profile was acquired to estimate the influence of bubbles on the CSI measurements.

The raw data was processed as described in section 4.2.3. The spatially resolved ^1H resonances of water, ^{13}C resonances of CO_2 and coalesced HCO_3^-/CO_3^{2-}, as well as ^{23}Na resonances of Na^+ were fitted using Lorentzian functions, providing their respective chemical shift, integral and Full Width at Half Maximum (FWHM) for further evaluation.

As previously described in chapter 3, the pH evaluation was performed based on the acquired chemical shift of the coalesced HCO_3^-/CO_3^{2-} resonance, which will be denoted as carbonate chemical shift (CCS), as well as the fitted integrals of the CO_2 and HCO_3^-/CO_3^{2-} resonances. Below the threshold value pH = 7.4, the Hendersson–Hasselbalch (HH) equation is used, *cf.* equation 3.3. The pK_{a2} value for the equilibrium reaction between CO_2 and HCO_3^- was determined to 6.467 for a temperature of 10 °C using literature data [117]. Above the threshold pH, a modulation of the HH equation describing the equilibrium reaction between HCO_3^- and CO_3^{2-} that is based on the CCS was applied, *cf.* equation 3.12. Here, pK_{a1} was experimentally determined to 9.645 and the chemical shift of pure HCO_3^- $\delta_{HCO_3^-}$ and CO_3^{2-} $\delta_{CO_3^{2-}}$ were 163.27 ppm and 171.01 ppm, respectively, where an NMR reference was used to define the chemical shift axis. As no NMR reference is used in the adjusted cell setup to ensure maximum sensitivity of measurements, the function describing the correlation of CCS and pH value had to be calibrated to match initial CCS with initial pH value in the sample. The pH value in the electrolyte after CO_2 saturation was determined using a benchtop Mettler–Toledo FiveEasy F20 pH meter with standard probe (Mettler–Toledo GmbH, Giessen, Germany). The measured pH averaged to 6.71 ± 0.04 for 0.1 M, 7.25 ± 0.07 for 0.5 M, and 7.58 ± 0.03 for 1 M $NaHCO_3$ and $KHCO_3$ solutions, respectively.

After the *in operando* measurements were conducted, electrodes were removed and the deuterated NMR reference trimethylsilylpropanoic acid (TSP) is added to the NMR tube to result in a concentration of 1 mM. The product analysis was performed using ^{1}H NMR with water suppression [96], as described in section 3.2.4.

5.3 Results and discussion

5.3.1 Electrochemical measurements

The results of CP and CV measurements of *in operando* experiments are given in figure 5.3 for 0.1 M, 0.5 M and 1 M $NaHCO_3$ and $KHCO_3$ electrolyte. The current density was chosen to result in a potential of $-1.4\,V$ *vs.* RHE. Figure 5.3.a shows the potential over time. The applied current density is plotted over the mean potential during CP in figure 5.3.b. Additionally, the third cycle of CV before *in operando* measurements is plotted to complete the overview over the current–voltage characteristics of the cell with varying electrolytes.

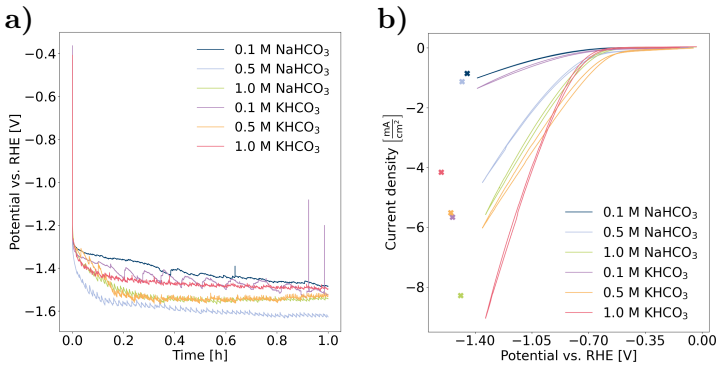

Figure 5.3: (a) Evolution of potential during CP in *in operando* experiments with 0.1 M, 0.5 M and 1 M $NaHCO_3$ and $KHCO_3$ electrolyte. (b) Current–voltage characteristics of *in operando* cell. The third cycles of CV before electrolysis are plotted for 0.1 M, 0.5 M and 1 M $NaHCO_3$ and $KHCO_3$ electrolyte. Additionally, the current density over mean potential during CP for the respective electrolyte is plotted as single cross.

5.3.2 Correction of chemical shift profiles

Figure 5.4.a represents an exemplary frequency encoded ^{1}H profile of the electrochemical cell. The placement of the cell relative to the NMR sensitive volume is shown in figure 5.4.b, where the origin of the z-axis is set to the centre of the sensitive volume. The electrode was accordingly placed at $z = -5$ mm. Thus, the sharp increase in intensity above $z = -5$ mm corresponds to the high proton density of the aqueous electrolyte. The decrease of intensity at $z > 5$ mm is due to sensitivity loss of the probe towards the boundaries of the sensitive volume. Therefore, the volume investigated in the following discussion is restricted to ca. 10 mm above the WE on the z-axis, where the excitation is approximately homogeneous. This intrinsic field inhomogeneity of the sensitive volume is due to the BBO version of the DiffBB probe used in this study. Here, the ^{1}H coil encloses the broadband coil, hence it is not optimised for ^{1}H but instead for broadband nucleus field homogeneity.

The resulting images of CSI measurements of the ^{1}H resonance of water, the ^{13}C carbonate resonance and the ^{23}Na resonance of Na^+ in 1 M $NaHCO_3$ electrolyte are depicted

in figure 5.4.c to 5.4.e, respectively. The corresponding chemical shift and integral profiles over the z-axis are depicted in figure 5.4.f to 5.4.h, respectively. In all experiments, an initially increased CCS was observed in electrode-proximity on the order of ca. 0.5 ppm. This effect was also observed in the ^{23}Na images and in the ^{1}H images recorded as reference before the *in operando* measurements, *cf.* figure 5.4.c and 5.4.e, respectively. Therefore, this nucleus independent chemical shift was assigned to magnetic field effects as a result of inhomogeneities induced by the conductive WE and imperfect magnetic field homogenisation by shimming. As the CCS is crucial for pH determination, a correction was required, which assumes a uniform spatial distribution of the pH value, and therefore also of the CCS, along the z-axis measured in CO_2 saturated electrolyte. The uncorrected CCS profiles in figure 5.4.i during underpotential CA before electrolysis are compared to corrected CCS profiles using the ^{1}H chemical shift profile of water, the initial ^{13}C CCS profile, and the ^{23}Na chemical shift profile of Na^+, depicted in figures 5.4.j to 5.4.l, respectively. The CCS was evenly distributed in all corrected profiles at the beginning of measurements as expected, if no external field is applied. An increase in CCS near the electrode evolved over 2 h of underpotential CA before electrolysis. All following ^{13}C CCS profiles were, therefore, corrected with the initially acquired ^{13}C image, all ^{23}Na profiles accordingly with the initially acquired ^{23}Na image.

5.3.3 ^{13}C and ^{23}Na images under underpotential and electrolytic conditions

The evolution over time of the frequency encoded ^{1}H profiles, as well as ^{13}C and ^{23}Na images at -1.4 V vs. RHE is depicted for 1 M $NaHCO_3$ electrolyte in Figure 5.5. During the underpotential CA before electrolysis, no significant changes in ^{1}H profiles were observed. An initially decreased intensity in the profile at ca. $z = 3$ mm was attributed to a single bubble attached to the insulated Cu wire. The profile peaks at the position of the electrode, which is assumed to be an effect of magnetic field distortions in proximity of conductive components. Both the ^{13}C and ^{23}Na images develop towards an equilibrium state. During 1 h under electrolysis conditions, ^{1}H profiles indicate large bubbles forming in the sensitive volume. These findings can be interpreted as snapshots of the cell as the experiment time is short with ca. 10 s. Similarly severe disruptions of the ^{13}C profiles were not observed, as errors induced by bubbles in the sensitive volume averaged out over the relatively long experiment time. Still, uncertainties in the course of the profiles could not be entirely precluded. ^{23}Na images were rather prone to distortions as a result of bubble formation and adhesion due to their shorter experiment time. The quality of the data had to be assessed individually by comparing ^{23}Na profiles with ^{1}H profiles.

Carbonate and Na^+ showed a general trend of increasing chemical shifts along the whole z-axis during electrolysis, with increased gradient towards the electrode. The maximum changes after 1 h electrolysis in ^{13}C and ^{23}Na shift were on the order of 0.5 ppm and 0.2 ppm, respectively. This rules out a magnetic field induced change of chemical shift, which would

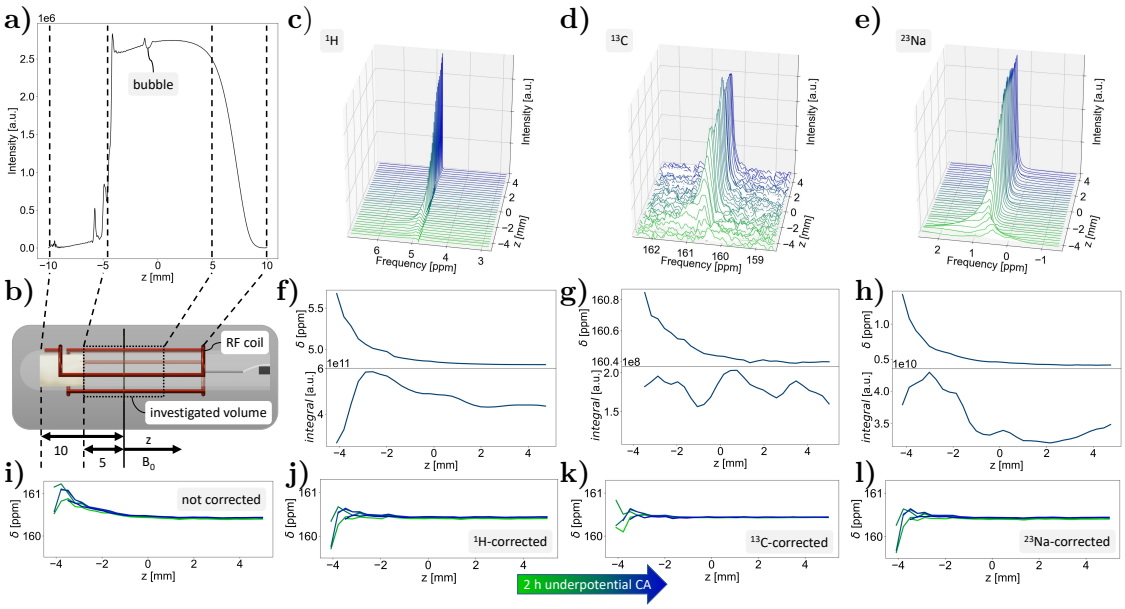

Figure 5.4: CSI profiles of 1 M $NaHCO_3$ electrolyte in the *in operando* cell illustrate nucleus independent chemical shift due to magnetic field distortions. (a) Frequency encoded ^{1}H image shows intensity profile along z-axis in the sensitive volume depicted in schematic b). The location of the electrode is shown relative to the sensitive volume and the z-axis. The volume with uniform excitation above the WE investigated in the following measurements corresponds to a length of ca. 10 mm on the z-axis. (c) – (e) Spatially resolved CSI spectra of the ^{1}H resonance of water (c), the ^{13}C resonance of carbonate (d), and the ^{23}Na resonance of Na^+ (e). (f) – (h) Chemical shift and integral as a function of z of the fitted peaks depicted in (c) – (e), respectively. (i) – (k) Evolution of the CCS during underpotential CA before electrolysis without correction (i) and corrected using the chemical shift profiles in (f) – (h), respectively.

otherwise result in quantitatively equal changes of chemical shift of various nuclei. The increase in CCS could be attributed to an increase in local pH. Notably, the largest change in CCS occurred at the start of the electrolysis. Towards the end, chemical shift profiles run into an upper limit, which suggests a mixing of the volume in electrode-proximity with the bulk electrolyte. This finding suggests that a convective flow is induced in the cell due to magnetohydrodynamic (MHD) forces [57] or local heating. Such a flow would also enhance the detachment of bubbles in the sensitive volume [118]. Lastly, it is noted that the CO_2 signal intensity decreased below the detection limit in WE proximity during electrolysis.

After electrolysis, the cell was operated under underpotential CA, where in consent with the previous CA phase only minor changes in the profiles were observed. However, there is a persisting difference between the profiles before electrolysis, indicated by bright green colour, and after electrolysis, indicated by dark green to blue colour. This depicts an overall increase in pH of the cell. Increasing integrals of the carbonate resonances may

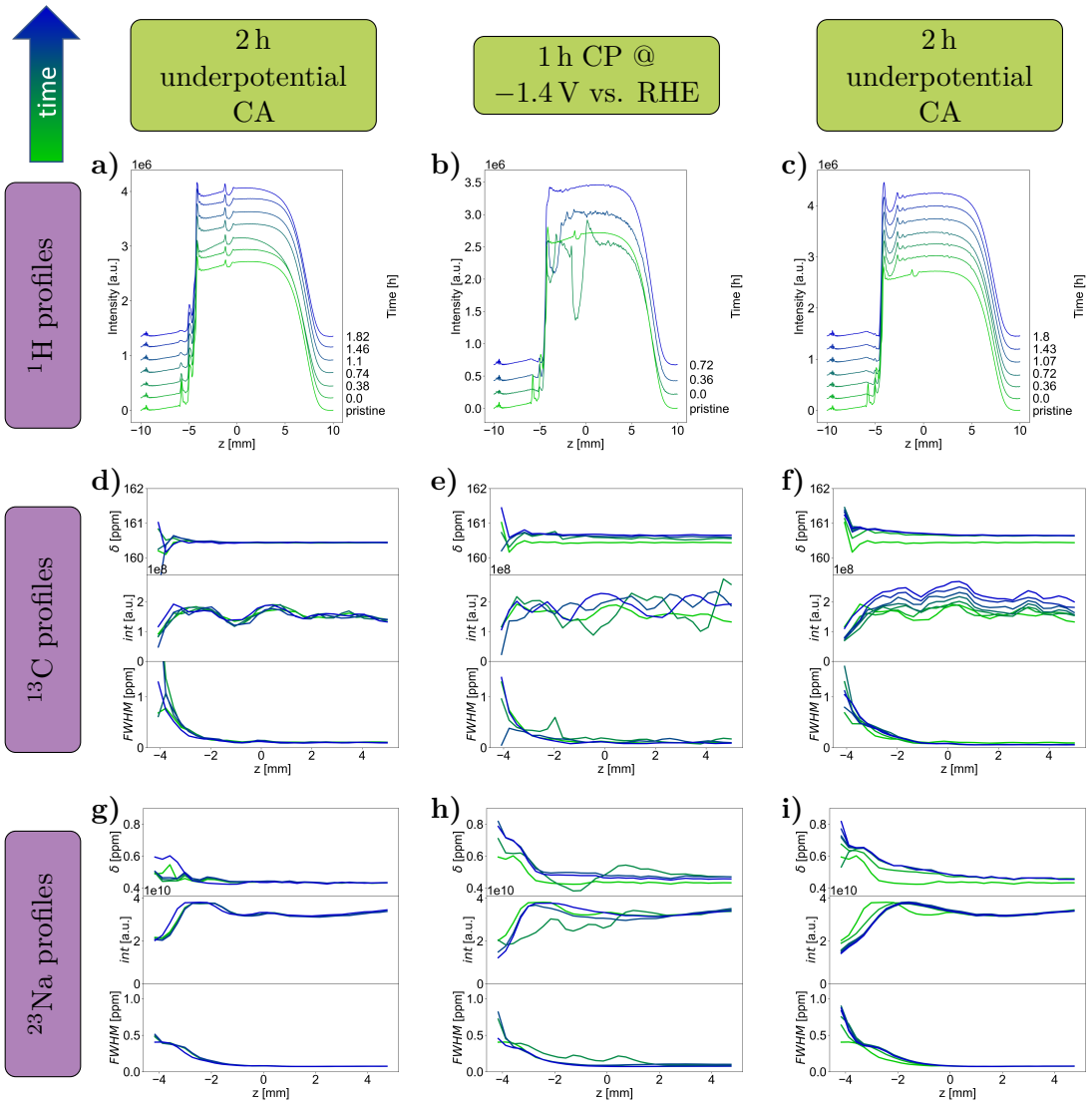

Figure 5.5: Exemplary *in operando* CSI with 1 M $NaHCO_3$. (a) – (c) Evolution of frequency encoded ^{1}H profiles before (a), during (b) and after (c) electrolysis, respectively. (d) – (f) Evolution of phase encoded ^{13}C CSI images before (d), during (e) and after (f) electrolysis, respectively. (g) – (i) Evolution of phase encoded ^{23}Na CSI images before (g), during (h) and after (i) electrolysis, respectively. Evolution of profiles over time is represented by the shift from green to blue colour. For reference, the last profiles acquired before electrolysis (a), (d) and (g) are repeated as first profiles in bright green in the plots representing the measurements during electrolysis (b), (e), (h) and after electrolysis (c), (f), (i), respectively.

also be affected by decreased T_1 relaxation times.

Figure 5.6 compares the fitting parameters of ^{13}C and ^{23}Na images of experiments with 0.1 M, 0.5 M and 1 M $NaHCO_3$ electrolyte during electrolysis. For the discussion of errors in CSI measurements, systematical and statistical errors were distinguished. In the interest of clarity of figures, systematical errors resulting from peak broadening and

peak fitting are presented in figures 5.9 to 5.12 in section 5.3.5, supplementing figure 5.6. Standard deviations from statistical averaging from three repeated experiments are given in the results of pH profile determination, *cf.* figure 5.7.

In the exemplary experiments presented in figure 5.6, increase of the chemical shifts and integrals of carbonate, as well as simultaneous decrease in CO_2 integral imply increased local pH in all cases, but varying in their extent. The ^{23}Na images show increased chemical shifts while integral and width remain unaltered except for outliers due to bubbles in the sensitive volume. The ^{23}Na shift of Na^+ cations was found to be concentration dependent [119]. However, the integral profiles in the presented experiments remained essentially constant during electrolysis and could, therefore, not account for this effect. In contrast, the buffering effect of cation hydrolysis proposed by Singh *et al.* offers an explanation for these observations. A fully hydrated Na^+ cation is accompanied by four H_2O molecules in its hydration shell. DFT calculations showed that the dehydration of $Na^+(H_2O)_n$ clusters, where n represents the hydration number, leads to a downfield shift of the ^{23}Na resonance of Na^+ [120]. In particular, the chemical shift difference between $n = 4$ and $n = 3$ was calculated to 7.1 ppm. Here, we observe a downfield shift on the order of 0.1–0.2 ppm. According to equation 5.1, this could be explained by a small amount of $Na^+(H_2O)_3$ formed by dehydration in fast chemical equilibrium with $Na^+(H_2O)_4$. Therefore, only one coalesced resonance is observed that is the weighted average of the Na^+ signals with hydration numbers $n = 3$ and $n = 4$, which range between 0 and 7.1 ppm.

Figure 5.7 depicts the evolution of pH profiles during electrolysis at -1.4 V vs. RHE, determined from chemical shifts and integrals of carbonate, as well as CO_2 integrals. This figure contrasts results of experiments with $NaHCO_3$ and $KHCO_3$ electrolyte of 0.1 M, 0.5 M and 1 M concentrations. Additionally, standard deviations of the pH profiles from statistical averaging of three repeated experiments are given in the figure. In all experiments a significant increase in local pH was detected. The largest pH changes were observed for the least buffered 0.1 M electrolytes, ranging from roughly 6.6 to 8.5. The 1 M electrolytes spanned a pH range from 7.6 to 8.5. Error bars in figure 5.7 were relatively small, especially for 0.5 M and 1 M initial concentration, confirming statistical significance of the presented experiments. For all three concentrations, the local pH values measured for the $NaHCO_3$ electrolyte were higher than for $KHCO_3$. Also, the experiments with Na^+ cations evolved a higher pH gradient than those with K^+. The additional buffering capacity due to decreased pK_a of cation hydrolysis of K^+ compared to the smaller Na^+ cations may also account for this effect. Singh *et al.* reported a cathode pH of 8.5 for 0.1 M $NaHCO_3$, which is in accordance with the present study, while the pH reported for 0.1 M $KHCO_3$ was 7.3, which is lower than our measured pH of approximately 8. Our study rather agrees with the findings of Ayemoba *et al.* [44], who measured local pH values of ca. 8.7 for $NaHCO_3$ and ca. 8 for $KHCO_3$, confirming the overestimation of the buffering effect of K^+ by Singh *et al.*

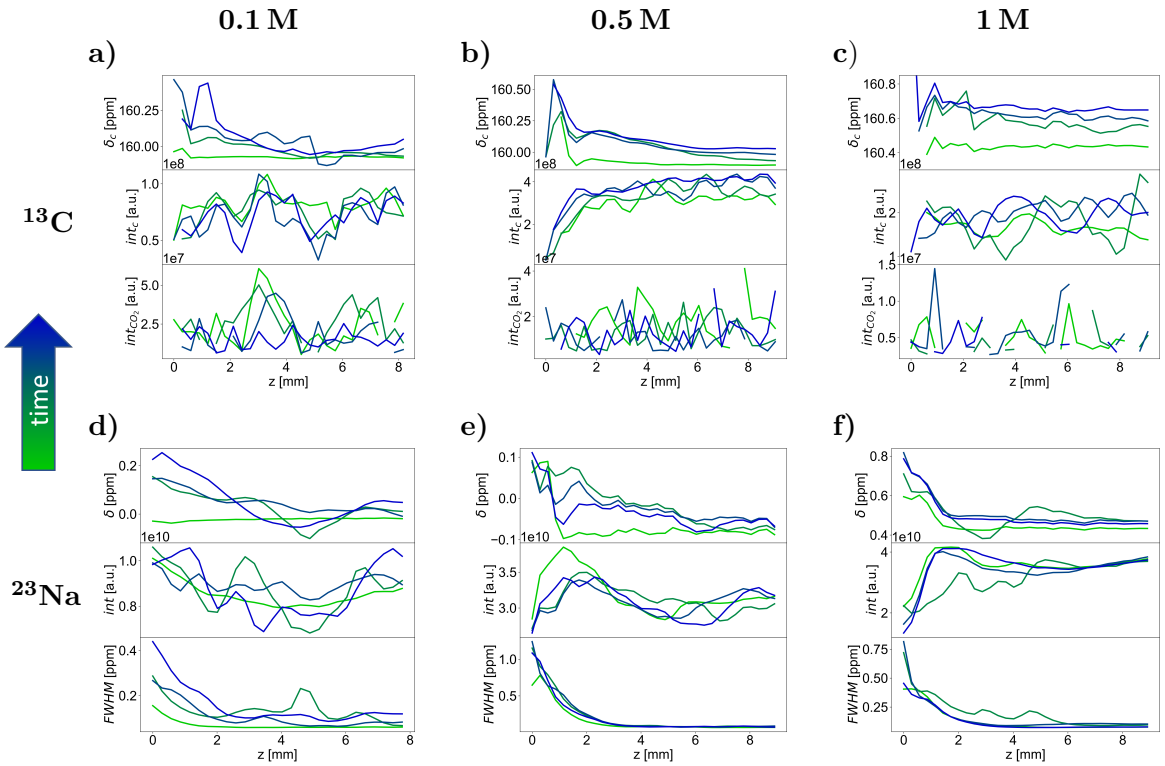

Figure 5.6: Results of ^{13}C and ^{23}Na CSI measurements during electrolysis at ca. $-1.4\,V$ *vs.* RHE with 0.1 M, 0.5 M and 1 M $NaHCO_3$ electrolyte. (a) – (c) Chemical shift and integral of ^{13}C carbonate resonance and integral of ^{13}C CO_2 resonance as a function of distance to electrode for 0.1 M (a), 0.5 M (b) and 1 M (c) initial $NaHCO_3$ concentration, respectively. (d) – (f) Chemical shift integral and FWHM of ^{23}Na resonance of Na^+ as a function of distance to electrode for 0.1 M (d), 0.5 M (e) and 1 M (f) initial $NaHCO_3$ concentration, respectively. The origin of the z-axis is set at the position of the WE. Evolution of profiles over time is represented by the shift from green to blue colour.

5.3.4 Product analysis

The effect of cation variation on product selectivity is manifested in the *ex situ* analysis of liquid products formed during the *in operando* experiments. Figure 5.8.a and 5.8.b show the product analysis in terms of concentration and Faradaic Efficiency (FE), respectively. The concentrations of impurities detected in pristine 1 M stock solutions of $NaHCO_3$ and $KHCO_3$ electrolytes are shown for comparison. For the calculations of FE of the formed liquid products, residuals of impurities in the pristine solutions were subtracted from the product concentrations as described in section 3.2.4. In general, formate, acetate, dissolved methane and acetaldehyde were detected in all samples. The most pronounced difference between product distributions with $NaHCO_3$ and $KHCO_3$ electrolytes was that alcohols, *i.e.* ethanol and, to a lower extent, methanol, were found only in $KHCO_3$ electrolytes, while the FE for acetate was larger for $NaHCO_3$ electrolytes. Increased FE of ethanol and formate for larger metal cations in bicarbonate electrolytes was also confirmed in earlier

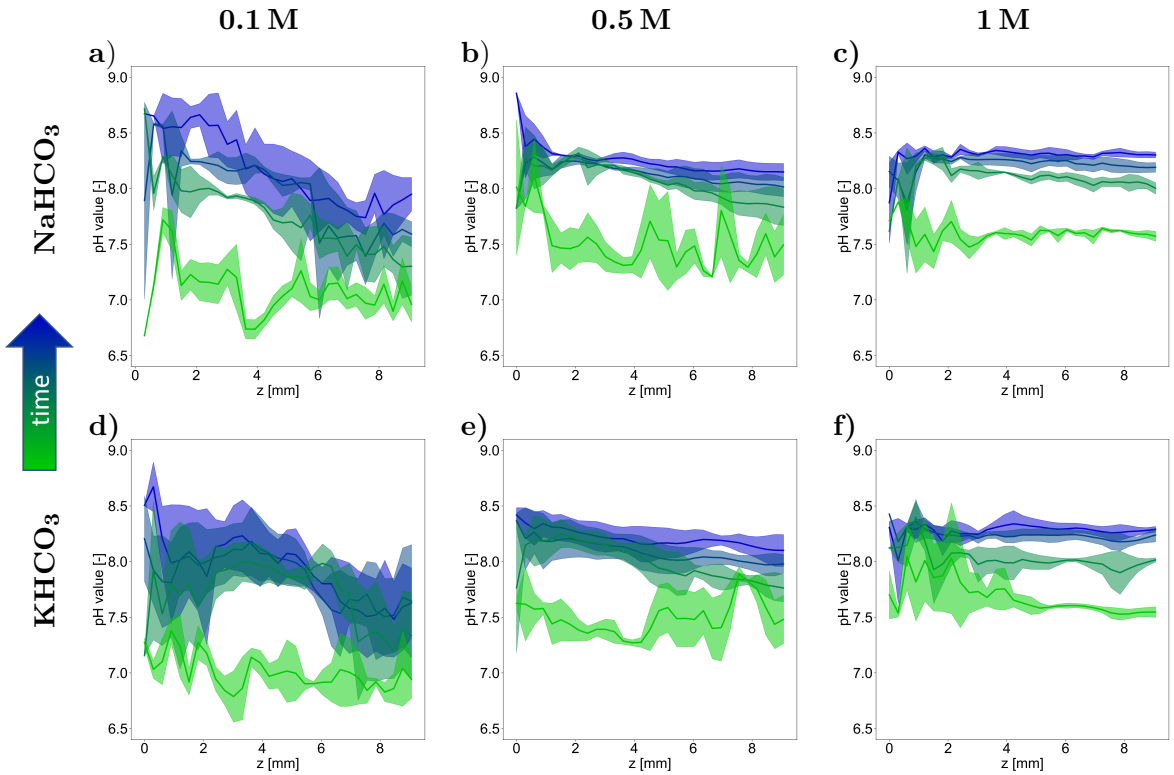

Figure 5.7: Mean pH profiles and standard error from three repeated experiments during electrolysis at ca. −1.4 V *vs.* RHE with (a) – (c) 0.1 M, 0.5 M and 1 M $NaHCO_3$ electrolyte, and (d) – (f) 0.1 M, 0.5 M and 1 M $KHCO_3$ electrolyte, respectively. The origin of the z-axis is set at the position of the WE. Temporal evolution of profiles is represented by the shift from green to blue colour.

studies [43, 45, 111]. Highest FE for formate was observed for the least buffered 0.1 M solutions, which is in accordance with literature data [29]. However, increased acetate formation was not observed for Na^+ or smaller cations. Instead it was only detected for larger cations [111]. Recently, Heenen *et al.* presented a mechanism for acetate formation via a solution-based reaction of ketene with OH^- [121] that is schematically depicted in figure 5.8.c. As it evolves as homogeneous reaction in the electrolyte, it is favoured under highly basic conditions and is governed by transport effects. They also stated that more positive potentials, *i.e.* > −1.2 V *vs.* SHE, as well as more negative potentials, *i.e.* < −1.5 V *vs.* SHE, supported this reaction, which applies to the described experiments at ca. −1.78 V *vs.* SHE. Since no external mixing force was applied except for MHD convection and CO_2 signals decreased below detection limit, it is assumed that transport of reactants was limited. Ketene intermediates could, therefore, desorb into the solution and could further react to acetate. The increased local pH gradients found in the presented measurements in $NaHCO_3$ electrolytes compared to $KHCO_3$ were due to the interplay of OH^- production, proton consumption and solution phase reactions with OH^- caused by the limited mass transport conditions [38]. Thus, steep pH gradients can be an indicator for enhanced solution-based

reaction to acetate. Interestingly, a similar contradiction to expectations of local CO_2

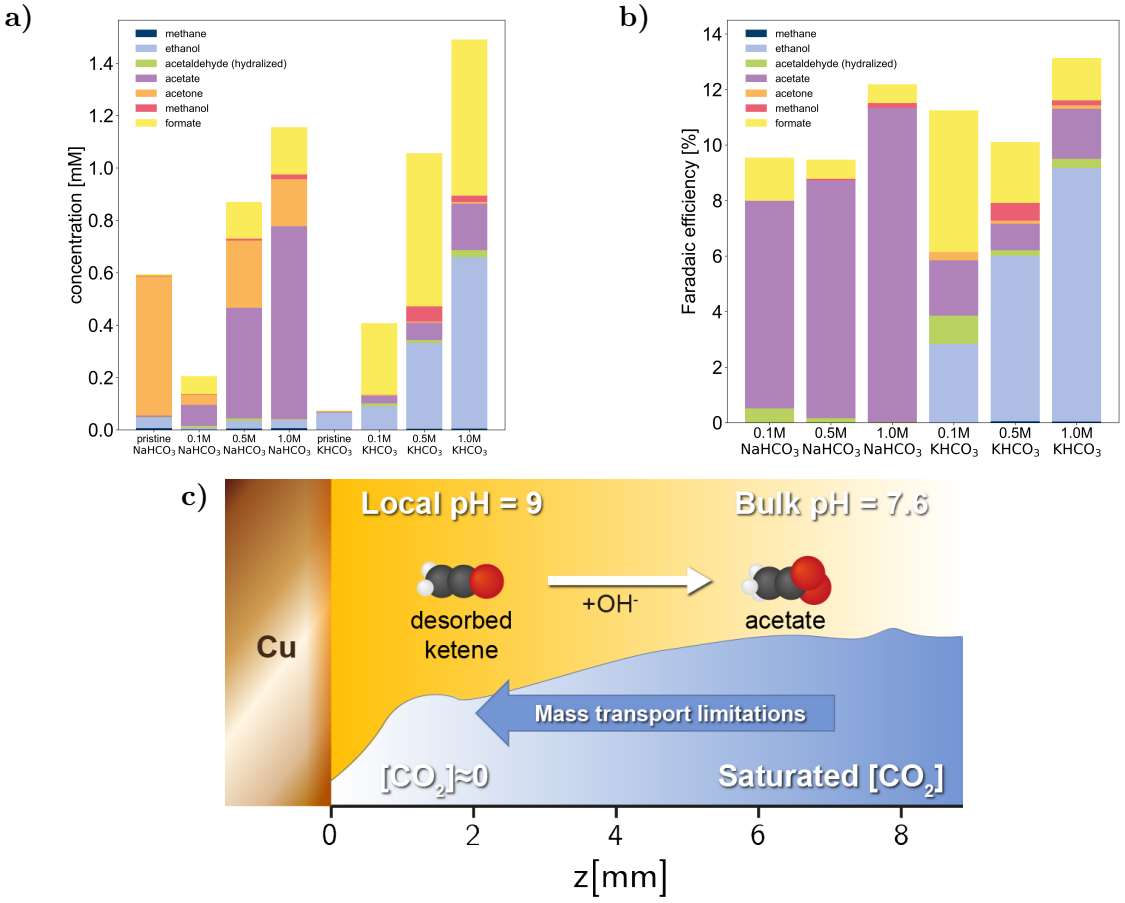

Figure 5.8: Product analysis using *ex situ* ^{1}H NMR with water suppression. (a) Concentrations of products detected in liquid solution of 0.1 M, 0.5 M and 1 M $NaHCO_3$ and $KHCO_3$ after *in operando* experiments at ca. −1.4 V *vs.* RHE and concentrations of impurities detected in pristine $NaHCO_3$ and $KHCO_3$ electrolytes. (b) Resulting Faradaic efficiencies of eCO_2R products for 0.1 M, 0.5 M and 1 M $NaHCO_3$ and $KHCO_3$ electrolytes. (c) Schematic of the solution-based acetate formation mechanism proposed by Heenen *et al.* [121], applied to the presented *in operando* experiments.

concentration was noticed by Malkani *et al.* [112]. With increased buffer capacity by larger cations, a higher interfacial CO_2 concentration is expected. However, CO_2 resonances stay longer above the detection limit for the less buffered $NaHCO_3$ electrolytes. As the total FE of eCO_2R for $KHCO_3$ electrolytes is higher compared to $NaHCO_3$ despite lower CO_2 availability, it is suggested that larger cations accelerate eCO_2R regardless of decreased interfacial CO_2 solubility [112].

5.3.5 Estimation of systematic errors

To estimate uncertainties in figure 5.5, 5.6 and 5.7 in the main text, peak broadening near the electrode was considered as systematic error of the estimation of chemical shifts, while

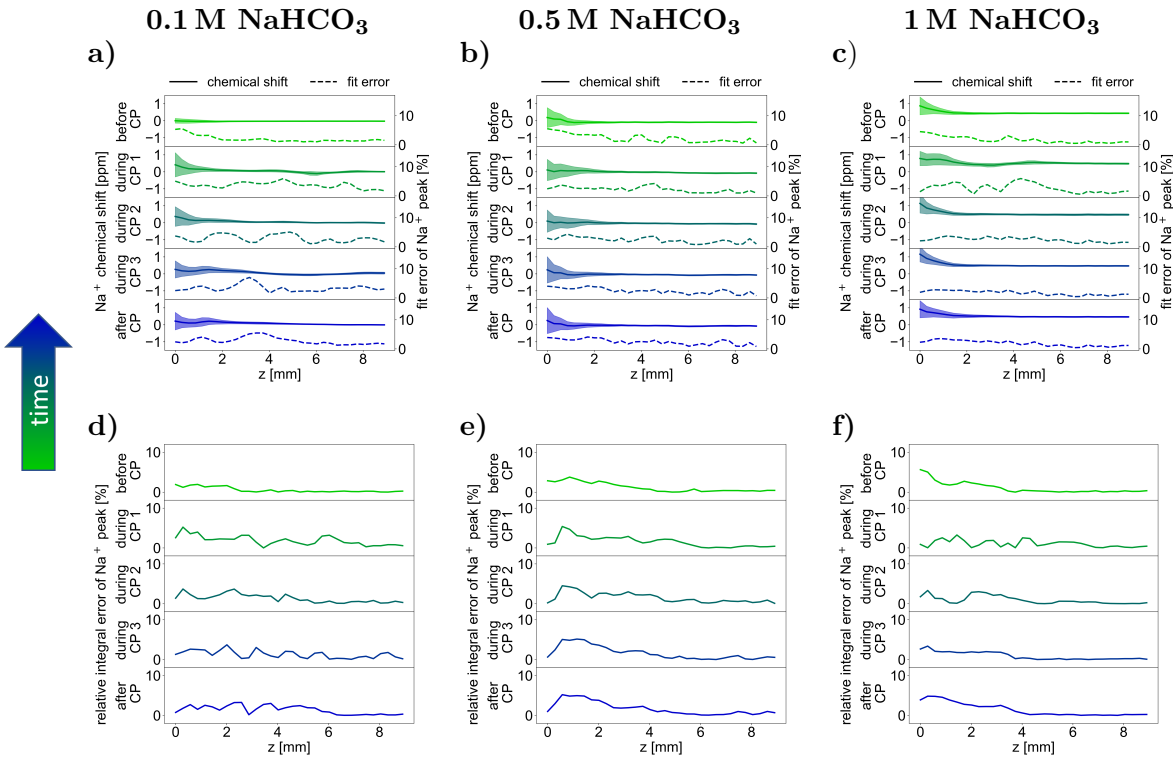

Figure 5.9: Error estimation of ^{23}Na CSI of 0.1 M, 0.5 M and 1 M $NaHCO_3$ electrolyte, respectively, supplementing *in operando* experiments in figure 5.5 in the main text. (a) – (c) The FWHM is depicted as uncertainty interval of the Na^+ chemical shift, as well as the mean relative fit error of the Na^+ peak, and (d) – (f) the relative integral error of Na^+ peak is depicted as a function of z for five exemplary measurements, one before, three during and one after CP under electrolytic conditions.

the difference between the integral of the fitted peak and the integral of the data was considered as systematic error of the estimation of integrals. For the latter, the relative error was calculated by,

$$\frac{\varepsilon_s}{s} = \left| \frac{s_{\text{fitted}}}{s_{\text{data}}} - 1 \right| . \tag{5.4}$$

For five exemplary measurements – one before, three during and one after CP under electrolytic conditions – figure 5.9 to 5.13 depict the z-dependent errors of various variables presented in the main text. Figure 5.9 depicts uncertainties of the ^{23}Na CSI measurements, *i.e.* FWHM as uncertainty interval of the chemical shift, the relative integral error described in equation 5.4 and the z-dependent mean relative fit error calculated by the 'lmfit' package for Python as a goodness-of-fit measure. The latter describes the confidence interval at every data point in the spectrum, in which there is a probability of 68.3 % to find the true value of this data point [122, 123]. This confidence interval is related to the fit value at the respective data point and averaged over the whole fit to provide the mean relative error of every fit at every point on the z-axis. Figure 5.10, 5.11 and 5.12 depict

the estimation of systematic errors of the values that were used to determine the pH value, *i.e.* the carbonate chemical shift and the integrals of carbonate and CO_2. To estimate the error of pH determination, the propagation of errors in equation 3.3 and 3.12 in the main text was considered.

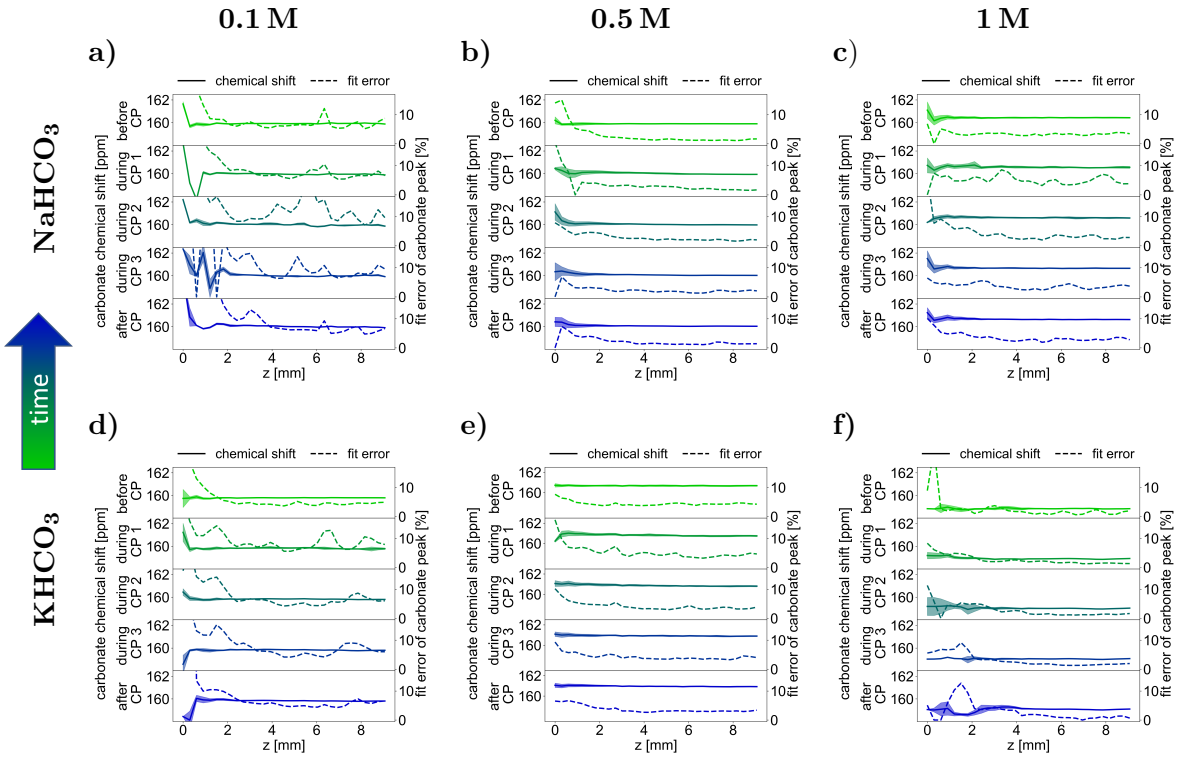

Figure 5.10: Error estimation of ^{13}C CSI in terms of carbonate chemical shift and integral, supplementing *in operando* experiments in figure 5.5 in the main text. The FWHM is depicted as uncertainty interval of the carbonate chemical shift, as well as the mean relative fit error of the carbonate peak, as a function of z for five exemplary measurements, one before, three during and one after CP under electrolytic conditions, determined for experiments with (a) – (c) 0.1 M, 0.5 M and 1 M $NaHCO_3$ and (d) – (f) $KHCO_3$ electrolyte, respectively.

Below the threshold value of pH = 7.4, the pH error $\varepsilon_{\mathrm{pH}}$ was calculated by,

$$\varepsilon_{\mathrm{pH}} = \sqrt{\left(\frac{\partial \mathrm{pH}}{\partial[\mathrm{HCO_3^-}]}\varepsilon_{[\mathrm{HCO_3^-}]}\right)^2 + \left(\frac{\partial \mathrm{pH}}{\partial[\mathrm{CO_2}]}\varepsilon_{[\mathrm{CO_2}]}\right)^2} \tag{5.5}$$

$$\varepsilon_{\mathrm{pH}} = \sqrt{\left(\frac{1}{\ln(10)[\mathrm{HCO_3^-}]}\varepsilon_{[\mathrm{HCO_3^-}]}\right)^2 + \left(-\frac{1}{\ln(10)[\mathrm{CO_2}]}\varepsilon_{[\mathrm{CO_2}]}\right)^2}. \tag{5.6}$$

As the concentrations of HCO_3^- and CO_2 are equivalent to the integrals of the peaks of the respective species, equation 5.6 can be expressed using the relative integral errors

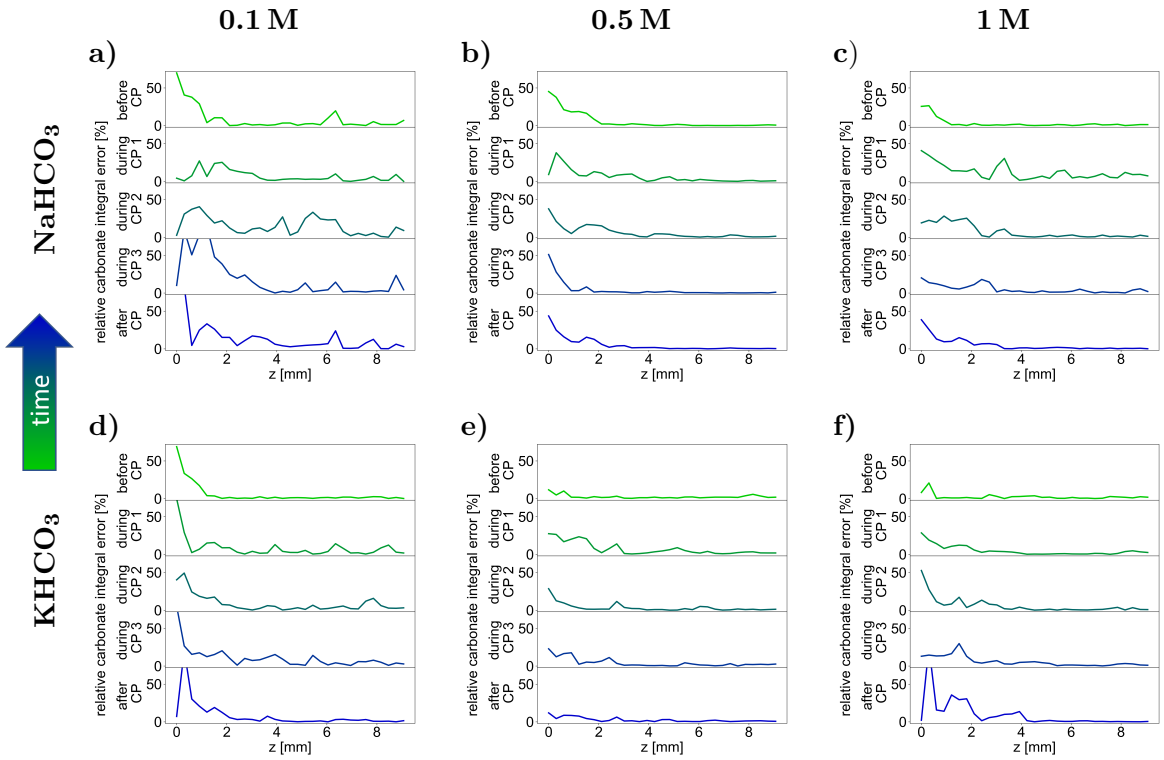

Figure 5.11: Error estimation of ^{13}C CSI in terms of relative integral error of the carbonate resonance, supplementing *in operando* experiments in figure 5.5 in the main text. The relative integral error is depicted as uncertainty interval of the carbonate integral, as a function of z for five exemplary measurements, one before, three during and one after CP under electrolytic conditions, determined for experiments with (a) – (c) 0.1 M, 0.5 M and 1 M $NaHCO_3$ and (d) – (f) $KHCO_3$ electrolyte, respectively.

determined by equation 5.4,

$$\varepsilon_{\mathrm{pH}} = \sqrt{\left(\frac{1}{\ln(10)}\frac{\varepsilon_{\mathrm{s}_{[\mathrm{HCO_3^-}]}}}{\mathrm{s}_{[\mathrm{HCO_3^-}]}}\right)^2 + \left(-\frac{1}{\ln(10)}\frac{\varepsilon_{\mathrm{s}_{[\mathrm{CO_2}]}}}{\mathrm{s}_{[\mathrm{CO_2}]}}\right)^2}\,. \tag{5.7}$$

For pH values above the threshold value of pH = 7.4, the pH error was calculated as error propagation of equation 3.12,

$$\varepsilon_{\mathrm{pH}} = \frac{\partial \mathrm{pH}}{\partial \delta_{\mathrm{c}}}\varepsilon_{\delta_c} \tag{5.8}$$

$$\varepsilon_{\mathrm{pH}} = \frac{\delta_{\mathrm{CO_3^{2-}}} - \delta_{\mathrm{HCO_3^-}}}{\ln(10)(\delta_{\mathrm{CO_3^{2-}}} - \delta_c)(\delta_c - \delta_{\mathrm{HCO_3^-}})}\varepsilon_{\delta_c}\,. \tag{5.9}$$

Consequently, the pH error $\varepsilon_{\mathrm{pH}}$ above the threshold value depends not only of the CCS error ε_{δ_c}, but also the value of δ_c itself. The CCS error is assumed to be equivalent to the half peak width, *i.e.* $\frac{\mathrm{FWHM}}{2}$. The resulting errors of the pH value are depicted as uncertainty intervals of pH profiles in figure 5.13 for the six exemplary experiments with

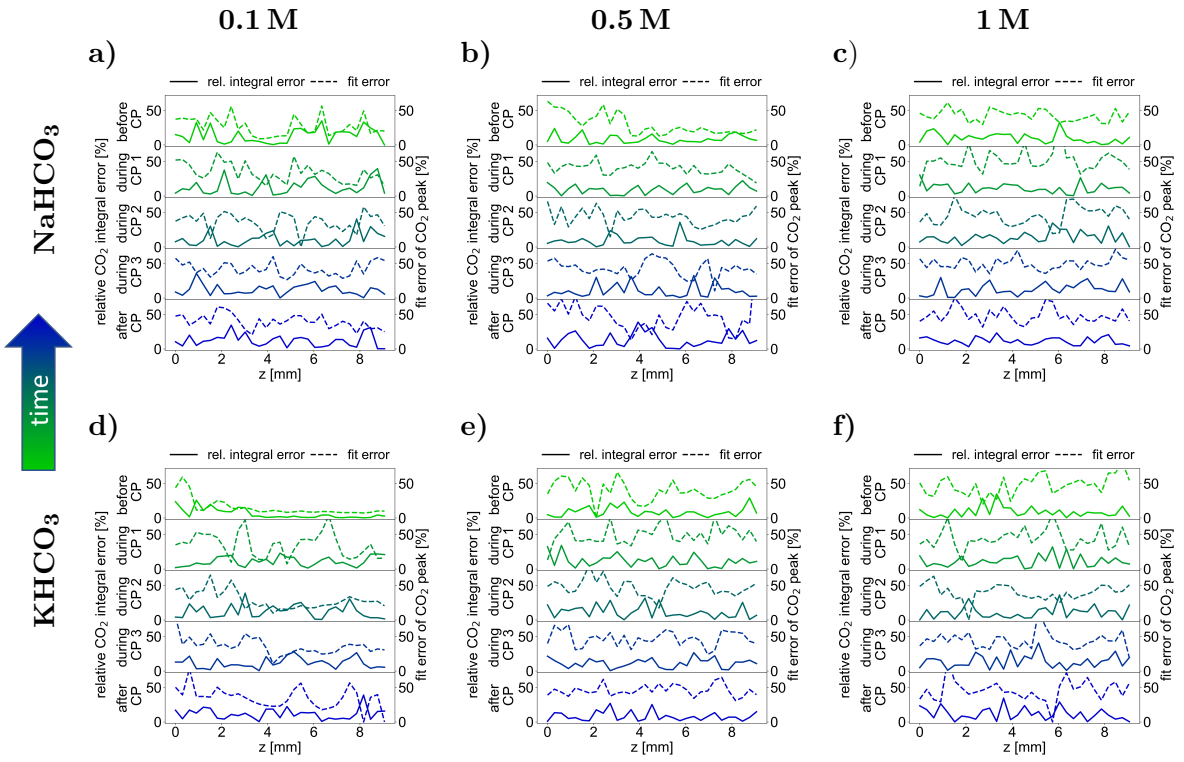

Figure 5.12: Error estimation of ^{13}C CSI in terms of relative integral error of the CO_2 resonance, supplementing *in operando* experiments in figure 5.5 in the main text. The relative integral error is depicted as uncertainty interval of the CO_2 integral, as well as the mean relative fit error of the CO_2 peak, as a function of z for five exemplary measurements, one before, three during and one after CP under electrolytic conditions, determined for experiments with (a) – (c) 0.1 M, 0.5 M and 1 M $NaHCO_3$ and (d) – (f) $KHCO_3$ electrolyte, respectively.

0.1 M, 0.5 M and 1 M $NaHCO_3$ and $KHCO_3$ electrolyte.

In general, all measurements showed increased uncertainties in terms of FWHM and fit errors in electrode proximity, *i.e.* at low z values. FWHM of carbonate peaks were on the order of 0.1 ppm in the bulk and increased to ca. 0.5 ppm, and even ca. 1 ppm in some cases, in electrode proximity.

Reasons for peak broadening in electrode proximity can be manifold. As it is observed in both ^{13}C and ^{23}Na measurements, magnetic field inhomogeneities partially accounted for this peak broadening. At the same time, the extent of broadening differ between ^{13}C and ^{23}Na measurements, indicating that also other effects had to be considered. A spatial distribution of chemical and physical environments of the spins in the plane perpendicular to the z-axis, which could not be spatially resolved, would explain such an additional peak broadening.

Fit errors near the electrode were higher in ^{13}C measurements. This could be caused by more pronounced peak broadening compared to ^{23}Na measurements and, therefore,

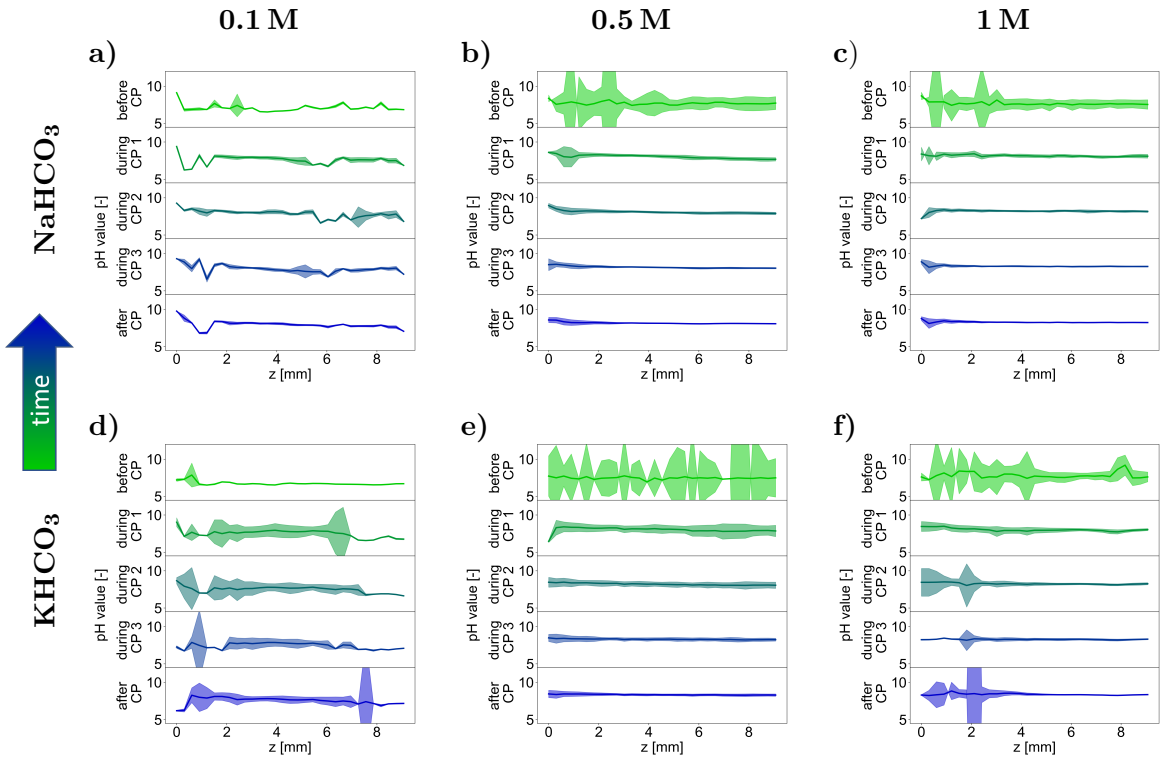

Figure 5.13: Estimation of systematic errors of the determined pH profiles as a result of error propagation in equations 3.3 and 3.12, supplementing *in operando* experiments in figure 5.6 in the main text. The systematic error is depicted as error bars at the pH profiles as a function of z for five exemplary measurements, one before, three during and one after CP under electrolytic conditions, determined for experiments with (a) – (c) 0.1 M, 0.5 M and 1 M $NaHCO_3$ and (d) – (f) $KHCO_3$ electrolyte, respectively.

worse signal-to-noise ratio. Also, unsymmetrical peaks shapes could explain increased errors, which may be resolved by fitting a second function to the data. However, fit errors were below 15 % in the investigated volume for Na^+ and carbonate resonances. In larger distance to the electrode, the fit errors were below 5 % mostly. Fit errors of CO_2 resonances reached values of up to 50 %. This is due to low initial concentration and consumption of dissolved CO_2 during electrolysis. Especially near the electrode, CO_2 is scarce during operation and, thus, barely detectable.

The relative integral errors, as calculated using equation 5.4, exhibited a rising trend towards the WE for all peaks but remained consistently below 10 % for Na^+ and mostly below 50 % for carbonate and CO_2. This error increase is mainly due to decreased signal to noise ratio in ^{13}C measurements compared to ^{23}Na.

The systematic error in pH values resulting from the errors of CCS and relative integral errors of carbonate and CO_2 predominately depended on the equation that was used for pH determination. Therefore, the error bars in figure 5.13 largely differed around the threshold value pH = 7.4. Generally, errors were large if the pH was determined using the CCS in

equation 3.12. More precisely, the error increased drastically, if δ_c was close to the chemical shift $\delta_{HCO_3^-}$ of pure $HCO_3{}^-$. In that case, $(\delta_c - \delta_{HCO_3^-})$ in the denominator of equation 5.9 took on a small value, which increased the value of the whole term. This is expressed by large error bars in pH profiles that are close to pH = 7.4, which is especially the case for profiles during CP with 0.1 M initial $NaHCO_3$ and $KHCO_3$ concentration and profiles before CP with 0.5 M and 1 M initial $NaHCO_3$ and $KHCO_3$ concentration. However, the measurements taken at the end of CP, which were primarily considered for the discussion of local pH effects and their interplay with cation effects, exhibit comparatively low systematic errors. Also considering statistical errors presented in section 5.3.3, the validity of the presented methodology was confirmed despite statistical and systematic uncertainties.

5.4 Conclusion

This study introduces a new method for spatially resolved local pH determination in bicarbonate electrolyte based on the ^{13}C resonances of the $CO_2/HCO_3^-/CO_3^{2-}$ equilibrium. By variation of the electrolyte concentration and the cation identity, the various buffer capacities of the electrolytes could be visualised under CO_2 reductive conditions at a Cu electrode. Using ^{23}Na profiles, decreased local pH could be attributed to an increased buffering effect of cation dehydration for larger cations. As predicted by theoretical calculations, we provided experimental evidence of the dehydration of the cation hydration shell during electrolysis. Furthermore, increased FE for acetate was stated for $NaHCO_3$ electrolyte and could be correlated to steep pH gradients by considering a mechanism of solution-based reaction of ketene intermediates with OH^-. However, the results confirmed that the buffering effect of the cation hydrolysis alone can not be accountable for the increased activity and selectivity of eCO_2R with increasing cation size. The differences in local pH profiles comparing $KHCO_3$ and $NaHCO_3$ electrolytes were not substantial enough to account for the variations in product distributions. As recently reported, stabilisation of eCO_2R intermediates and interfacial electric field effects remain the most important explanations of cation effects [42]. Nonetheless, the presented method has the potential to help engineering not only the electrode but also the electrolyte and, therefore, tailoring the EEI. For example by mixing electrolytes or by using non-aqueous electrolytes, the desired product distribution and selectivity may be tuned by determining local reaction conditions [104]. To effectively contribute to the engineering of EEIs, the greatest challenge is to overcome the mass transport limitations intrinsic to the presented *in operando* cell design.

5.5 Postface

The main part of this chapter was performed and researched by the author of the thesis, in particular:

1. The development and construction of the *in operando* electrolysis cell.
2. The conduction of the *in operando* MRI experiments of CO_2 electrolysis at Cu WE.
3. The processing and analysis of all electrochemical experiments.
4. The processing and analysis of all NMR experiments

Minor parts of this chapter were performed with assistance of the following co-worker:

1. The construction of the *in operando* electrolysis cell and conduction of the *in operando* MRI experiments was assisted by Johannes Kochs (IEK-9, Forschungszentrum Jülich GmbH, Germany).
2. The graphical presentation in figure 5.8 was supported by Sebastian B. C. Lehmann.

Chapter 6

Thesis summary, conclusion and outlook

In this thesis, *in operando* magnetic resonance techniques were developed and applied to investigate the complex interplay of species dissolved in the electrolyte during Cu-catalysed electrochemical Carbon Dioxide Reduction (eCO_2R).

First, pH determination by evaluating the ^{13}C resonances of HCO_3^-/CO_3^{2-} and CO_2 was presented. Despite errors due to introduction of electrically conductive materials and bubble formation in the sensitive Nuclear Magnetic Resonance (NMR) volume, the method was proven capable of determination of local pH near the electrode. Local pH values and product distributions at varied applied potentials were in accordance with literature.

Afterwards, the electrochemical cell and experiment protocol previously described was adjusted to enable application of Magnetic Resonance Imaging (MRI) techniques. Simulations of the magnetic field B_0 and the Radio Frequency (RF) field B_1 near the conductive electrode were in good agreement with experimental results. Thus, distortions caused by components of the electrochemical cell could be estimated by the calculations, and their influence on the *in operando* measurements were evaluated. The adjustments have been shown to establish stable electrochemical conditions at the electrode/electrolyte interface (EEI), which in turn resulted in reproducible potential dependent product distributions.

Finally, the results of experiments with varying concentrations of $KHCO_3$ and $NaHCO_3$ were presented through ^{13}C and ^{23}Na Chemical Shift Imaging (CSI). Increasing local pH profiles could be visualised and set into context with changes in the ^{23}Na resonance of Na^+ ions. In particular, increasing ^{23}Na chemical shifts near the electrode were attributed to partial dehydration of Na^+ cations. This was consistent with a mechanism proposed by Singh *et al.* describing additional buffering in electrode proximity by cation hydrolysis [111]. Also, the increasing trend of buffering capacity with increasing cation size reported therein could be confirmed by comparison of local pH values in $KHCO_3$ and $NaHCO_3$ electrolytes. Moreover, experiments with steeper pH gradients, as was found for $NaHCO_3$, showed increased acetate formation. This observation was explained by a mechanism for solution-based reaction of ketene intermediates proposed by Heenen *et al.* [121]. The results indicate that not only surface pH, but also the pH gradient in the electrolyte plays a role in product selectivity under specific reaction conditions.

Throughout all experiments and cell configurations, two major challenges were encoun-

tered that hindered the comparability with large scale electrolysis experiments. On the one hand, bubble formation did not only affect the electrochemical performance of eCO_2R, but also the MRI measurements. On the other hand, low concentration of dissolved CO_2 resulted in CO_2 scarcity at the electrode, as no external gas flow was supplied.

By implementing a Gas Diffusion Electrode (GDE) and gas flow in the *in operando* cell, several issues can be resolved. The local CO_2 availability would be comparable to industrially relevant requirements, bubble detachment would be enhanced and steady-state conditions enable measurements independent of experiment time. However, the implementation of such a method would require a redesigned cell in an NMR probe that offers more space and better accessibility. Also, it has to be considered that using ^{13}C enriched reactants in a flow cell will be expensive, because large quantities will be needed.

Increasing the spatial resolution of the presented experiments is currently limited by the required experiment time, which would otherwise exceed the time of catalyst deactivation. To improve the resolution of the electrolyte at the EEI, a surface-selective excitation should be employed. Simulations have shown that an increased B_1 field in electrode proximity is expected, which could be utilised in numerically optimised pulse sequences using optimal control by employing the increased nutation frequencies to select spins near the electrode.

A reliable platform for calculation of numerical pulses for *in operando* NMR measurements based on B_1 simulations could also be utilised to enable *in operando* ^1H measurements. These are not yet possible due to the strong ^1H resonance of water and insufficient *in operando* water suppression. Optimal control pulse sequences raise hope for successful suppression of the solvent peak during *in operando* electrolysis, providing deeper insight into the reaction mechanisms of products and intermediates.

Appendix A

Pulse program for Bruker TopSpin

```
;MS_1dCSI
;based on diffSe 2D Steiskal Tanner sequence
;phase-encoded chemical shift imaging along z-axis
;
;$CLASS=diff
;$DIM=2D
;$TYPE=exp

#include <Grad.incl>
#include <Avance.incl>
#include <Grad_Pulse.incl>

define list<gradient> diff_ramp=<$GPNAM31>

"acqt0=0"
"p2=2*p1"

;-----------------------------------------------------------
ze
10u
5m pl1:f1                              ;set rf power level
start, 100u ;GRAD_SYNC

;------------------- Decoupler ----------------------------
#ifdef DEC
  1u pl12:f2                       ; decoupler use pl12
        1u do:f2                          ; decoupler off during d1
#endif

;------------------------ Lock----------------------------
#ifdef LOCK
  d1 LOCKH_OFF                ; lock on during d1
  d11 UNBLKGRAD             ; unblank gradient amplifier, lock hold during
    experiment
#endif
#ifndef LOCK
  d1  H2_PULSE
  d11 UNBLKGRAMP                   ; unblank gradient amplifier
#endif

;------------------------- Spoiler recovery sequence ------
#ifdef SpoilRec
  p1:f1 ph11
  p23:gp23        ;(10m:1=18 G/cm)
  d2
```

```
  p1:f1 ph12
  p24:gp24        ;(1m:-5=-90 G/cm)
  d2
  d23 BLKGRAMP
#endif

;------------------ Start of dummy gradient loop ----------
#ifdef dummyGrad
  dummy, 1u
      d11 UNBLKGRAMP      ; unblank gradient amplifier
    gradPulse(cnst1, cnst2, cnst3, d17, d18, d16, l8, l9, diff_ramp)
    d2        ; gradient stabilisation time
    d9 BLKGRAMP     ; tau
  lo to dummy times l13       ; l13 number of dummy gradient pulses
#endif

;-------------------------- Start of experiment -----------
p1:f1 ph1         ; 90 degree pulse
d12
d11 UNBLKGRAMP          ; unblank gradient amplifier
gradPulse(cnst1, cnst2, cnst3, d17, d18, d16, l8, l9, diff_ramp)
d2            ; gradient stabilisation time
1u BLKGRAMP

;-------------------------- Water suppression -------------
#ifdef WSUP
  (p20:sp1 ph5):f1
  1u pl1:f1
#endif

;-----------------------------------------------------------
d9            ; to increase tau

;-------------------------- Watergate ---------------------
#ifdef WG
  p1*0.231 ph3              ;start selective watergate pi pulse
  d25*2
  p1*0.692 ph3
  d25*2
  p1*1.462 ph3
  d25*2
  p1*1.462 ph4
  d25*2
  p1*0.692 ph4
  d25*2
  p1*0.231 ph4
#endif

#ifndef WG
#ifdef Slice
      d11 UNBLKGRAMP      ; unblank gradient amplifier
      d22 grad{(cnst14) | (cnst15) | (cnst16)}
      p12:sp2:f1 ph2
      d22 groff
      d11 pl1:f1 BLKGRAMP
#else

#ifdef RefGrad
      d11 UNBLKGRAMP      ; unblank gradient amplifier
      d22 grad{(cnst14) | (cnst15) | (cnst16)}
      d22 groff
```

```
      d11 BLKGRAMP
#endif

      p2:f1 ph2         ; 180 degree pulse

#ifdef RefGrad
      d11 UNBLKGRAMP      ; unblank gradient amplifier
      d22 grad{(cnst14) | (cnst15) | (cnst16)}
      d22 groff
      d11 BLKGRAMP
#endif

#endif
#endif

;---------------------------------------------------------
d12           ; tau

;--------------------------- Water suppression -------------
#ifdef WSUP
      (p20:sp1 ph5):f1
      1u pl1:f1
#endif

;---------------------------------------------------------
d11
d18
d16           ; delay instead of refocussing
d2            ; gradient stabilisation time
1u
d9            ; to increase tau

;--------------------------- Decoupler ---------------------
#ifdef DEC
    go=start ph31 cpd2:f2           ; start acquisition with decoupling
#endif
#ifndef DEC
    go=start ph31                   ; start acquisition
#endif

;------------------------------ Aquisition -----------------
100u mc #0 to start F1QF(calgrad(diff_ramp))


;--------------------------- Decoupler ---------------------
#ifdef DEC
        100m do:f2                      ; wait for data storage, decoupler
   off
#endif
#ifndef DEC
        100m                            ; wait for data storage
#endif

;------------------------ Lock ---------------------------
#ifdef LOCK
      100m rf #0 LOCKH_OFF    ; reset file pointer, lock on
#endif
#ifndef LOCK
      100m rf #0              ; reset file pointer
#endif
```

```
;-----------------------------------------------------------
lo to start times l1      ; l1 = Number of repetitions
exit

;---------------------- Phase cycles -----------------------
#ifdef WG
ph1=0 2
ph3=0 0 1 1 2 2 3 3
ph4=2 2 3 3 0 0 1 1
ph31=0 2 2 0
#endif
#ifndef WG
ph1=0 2
ph2=0 0 1 1 2 2 3 3
ph31=2 0 0 2
#endif
ph11= 0
ph12= 1

;--------------------------- Comments on parameters -------
;pl1: f1 channel - power level for pulse (default)
;p1: f1 channel -  90 degree pulse
;p2: f1 channel -  180 degree pulse
;pl2: f2 channel - default not used
;pl12: f2 channel - decoupling power
;d17: gradient ramp up time
;d16: gradient ramp down time
;d18: gradient duration
;d1: relaxation delay; 1-5 * T1
;d2: gradient stabilisation time
;d9: to increase echo time tau
;d11: gradient amplifier unblank delay 200 us

;ns: 4 * n
;td1: number of points in k-space
;l1: Repetitions of the whole experiment
;l13: number of dummy gradient pulses

;$Id: MS_1dCSI,v 1.0 2023/05/16 m.schatz$
```

Listing A.1: Code of CSI pulse sequence for Bruker Topspin.

References

[1] A. Neslen, "Germany's e-fuel EU loophole could mean '135bn more litres of petrol burnt'", *The Guardian* **22.3.2023**.

[2] K. Abnett, "EU-German deal to map path for e-fuel cars after 2035", *Reuters Media* **27.3.2023**.

[3] J. Liboreiro, "In win for Germany, EU agrees to exempt e-fuels from 2035 ban on new sales of combustion-engine cars", *Euronews* **28.3.2023**.

[4] European Union, Regulation of the European Parliament and of the Council amending Regulation (EU) 2019/631 as regards strengthening the CO_2 emission performance standards for new passenger cars and new light commercial vehicles in line with the Union's increased climate ambition, **22 February 2023**.

[5] United Nations, Paris Agreement, **2015**.

[6] European Academies' Science Advisory Council, Hydrogen and synthetic fuels, **2020**.

[7] Climate Analytics, 1.5°C pathways for the EU27: accelerating climate action to deliver the Paris Agreement, **2022**.

[8] Agora Verkehrswende | Agora Energiewende, The Future Cost of Electricity-Based Synthetic Fuels, **2018**.

[9] C. Müller, A. Hoffrichter, L. Wyrwoll, C. Schmitt, M. Trageser, T. Kulms, D. Beulertz, M. Metzger, M. Duckheim, M. Huber, M. Küppers, D. Most, S. Paulus, H. J. Heger, A. Schnettler, "Modeling framework for planning and operation of multi-modal energy systems in the case of Germany", *Applied Energy* **2019**, *250*, 1132–1146.

[10] S. Teske, T. Pregger, S. Simon, T. Naegler, J. Pagenkopf, Ö. Deniz, B. van den Adel, K. Dooley, M. Meinshausen, "It Is Still Possible to Achieve the Paris Climate Agreement: Regional, Sectoral, and Land-Use Pathways", *Energies* **2021**, *14*, 2103.

[11] S. Nitopi, E. Bertheussen, S. B. Scott, X. Liu, A. K. Engstfeld, S. Horch, B. Seger, I. E. L. Stephens, K. Chan, C. Hahn, J. K. Nørskov, T. F. Jaramillo, I. Chorkendorff, "Progress and Perspectives of Electrochemical CO_2 Reduction on Copper in Aqueous Electrolyte", *Chemical reviews* **2019**, *119*, 7610–7672.

[12] R. G. Grim, Z. Huang, M. T. Guarnieri, J. R. Ferrell, L. Tao, J. A. Schaidle, "Transforming the carbon economy: challenges and opportunities in the convergence of low-cost electricity and reductive CO_2 utilization", *Energy & Environmental Science* **2020**, *13*, 472–494.

[13] J. Albo, M. Alvarez-Guerra, P. Castaño, A. Irabien, "Towards the electrochemical conversion of carbon dioxide into methanol", *Green Chemistry* **2015**, *17*, 2304–2324.

[14] Y. Y. Birdja, E. Pérez-Gallent, M. C. Figueiredo, A. J. Göttle, F. Calle-Vallejo, M. T. M. Koper, "Advances and challenges in understanding the electrocatalytic conversion of carbon dioxide to fuels", *Nature Energy* **2019**, *4*, 732–745.

[15] J. Qiao, Y. Liu, F. Hong, J. Zhang, "A review of catalysts for the electroreduction of carbon dioxide to produce low-carbon fuels", *Chemical Society reviews* **2014**, *43*, 631–675.

[16] H.-R. " Jhong, S. Ma, P. J. A. Kenis, "Electrochemical conversion of CO_2 to useful chemicals: current status, remaining challenges, and future opportunities", *Current Opinion in Chemical Engineering* **2013**, *2*, 191–199.

[17] R. Kortlever, J. Shen, K. J. P. Schouten, F. Calle-Vallejo, M. T. M. Koper, "Catalysts and Reaction Pathways for the Electrochemical Reduction of Carbon Dioxide", *The Journal of Physical Chemistry Letters* **2015**, *6*, 4073–4082.

[18] D. D. Zhu, J. L. Liu, S. Z. Qiao, "Recent Advances in Inorganic Heterogeneous Electrocatalysts for Reduction of Carbon Dioxide", *Advanced Materials* **2016**, *28*, 3423–3452.

[19] Y. J. Sa, C. W. Lee, S. Y. Lee, J. Na, U. Lee, Y. J. Hwang, "Catalyst-electrolyte interface chemistry for electrochemical CO_2 reduction", *Chem. Soc. Rev.* **2020**, *49*, 6632–6665.

[20] A. J. Bard, L. R. Faulkner, *Electrochemical Methods: Fundamentals and Applications*, 2nd Edition, John Wiley & Sons Inc, [s.l.], **2000**.

[21] C. H. Hamann, W. Vielstich, *Elektrochemie*, 4., vollst. überarb. und aktualisierte Aufl., Wiley-VCH, Weinheim, **2005**.

[22] A. Mustafa, B. G. Lougou, Y. Shuai, Z. Wang, S. Razzaq, J. Zhao, H. Tan, "Theoretical insights into the factors affecting the electrochemical reduction of CO 2", *Sustainable Energy & Fuels* **2020**, *4*, 4352–4369.

[23] T. E. Teeter, P. van Rysselberghe, "Reduction of Carbon Dioxide on Mercury Cathodes", *The Journal of chemical physics* **1954**, *22*, 759–760.

[24] Y. Hori, K. Kikuchi, A. Murata, S. Suzuki, "Production of Methane and Ethylene in Electrochemical Reduction of Carbon Dioxide at Copper Electrode in Aqueous Hydrogencarbonate solution", *Chemistry Letters* **1986**, *15*, 897–898.

[25] Y. Hori, A. Murata, R. Takahashi, S. Suzuki, "Electroreduction of carbon monoxide to methane and ethylene at a copper electrode in aqueous solutions at ambient temperature and pressure", *Journal of the American Chemical Society* **1987**, *109*, 5022–5023.

[26] Y. Hori, A. Murata, R. Takahashi, S. Suzuki, "Enhanced formation of ethylene and alcohols at ambient temperature and pressure in electrochemical reduction of carbon dioxide at a copper electrode", *Journal of the Chemical Society Chemical Communications* **1988**, 17.

[27] Y. Hori, A. Murata, R. Takahashi, "Formation of hydrocarbons in the electrochemical reduction of carbon dioxide at a copper electrode in aqueous solution", *Journal of the Chemical Society Faraday Transactions 1: Physical Chemistry in Condensed Phases* **1989**, *85*, 2309.

[28] Y. Hori, H. Wakebe, T. Tsukamoto, O. Koga, "Electrocatalytic process of CO selectivity in electrochemical reduction of CO_2 at metal electrodes in aqueous media", *Electrochimica Acta* **1994**, *39*, 1833–1839.

[29] Y. Hori in *Modern Aspects of Electrochemistry*, (Eds.: C. G. Vayenas, R. E. White, M. E. Gamboa-Aldeco), Modern Aspects of Electrochemistry, 42, Springer-Verlag, s.l., **2008**, pp. 89–189.

[30] A. Bagger, W. Ju, A. S. Varela, P. Strasser, J. Rossmeisl, "Electrochemical CO_2 Reduction: A Classification Problem", *Chemphyschem : a European journal of chemical physics and physical chemistry* **2017**, *18*, 3266–3273.

[31] K. P. Kuhl, E. R. Cave, D. N. Abram, T. F. Jaramillo, "New insights into the electrochemical reduction of carbon dioxide on metallic copper surfaces", *Energy & Environmental Science* **2012**, *5*, 7050.

[32] E. Wilhelm, R. Battino, R. J. Wilcock, "Low-pressure solubility of gases in liquid water", *Chemical Reviews* **1977**, *77*, 219–262.

[33] B. H. Gibbons, J. T. Edsall, "Rate of Hydration of Carbon Dioxide and Dehydration of Carbonic Acid at 25°", *Journal of Biological Chemistry* **1963**, *238*, 3502–3507.

[34] J. Zosel, W. Oelßner, M. Decker, G. Gerlach, U. Guth, "The measurement of dissolved and gaseous carbon dioxide concentration", *Measurement Science and Technology* **2011**, *22*, 072001.

[35] M. Dunwell, Q. Lu, J. M. Heyes, J. Rosen, J. G. Chen, Y. Yan, F. Jiao, B. Xu, "The Central Role of Bicarbonate in the Electrochemical Reduction of Carbon Dioxide on Gold", *Journal of the American Chemical Society* **2017**, *139*, 3774–3783.

[36] B. Deng, M. Huang, X. Zhao, S. Mou, F. Dong, "Interfacial Electrolyte Effects on Electrocatalytic CO_2 Reduction", *ACS Catalysis* **2022**, *12*, 331–362.

[37] G. Marcandalli, M. C. O. Monteiro, A. Goyal, M. T. M. Koper, "Electrolyte Effects on CO_2 Electrochemical Reduction to CO", *Accounts of chemical research* **2022**, *55*, 1900–1911.

[38] A. Xu, N. Govindarajan, G. Kastlunger, S. Vijay, K. Chan, "Theories for Electrolyte Effects in CO_2 Electroreduction", *Accounts of chemical research* **2022**, *55*, 495–503.

[39] N. Gupta, M. Gattrell, B. MacDougall, "Calculation for the cathode surface concentrations in the electrochemical reduction of CO_2 in $KHCO_3$ solutions", *Journal of Applied Electrochemistry* **2006**, *36*, 161–172.

[40] A. S. Varela, M. Kroschel, T. Reier, P. Strasser, "Controlling the selectivity of CO_2 electroreduction on copper: The effect of the electrolyte concentration and the importance of the local pH", *Catalysis Today* **2016**, *260*, 8–13.

[41] T. N. Nguyen, J. Guo, A. Sachindran, F. Li, A. Seifitokaldani, C.-T. Dinh, "Electrochemical CO_2 reduction to ethanol: from mechanistic understanding to catalyst design", *Journal of Materials Chemistry A* **2021**.

[42] M. C. O. Monteiro, A. Mirabal, L. Jacobse, K. Doblhoff-Dier, S. C. Barton, M. T. M. Koper, "Time-Resolved Local pH Measurements during CO_2 Reduction Using Scanning Electrochemical Microscopy: Buffering and Tip Effects", *JACS Au* **2021**, *1*, 1915–1924.

[43] A. Murata, Y. Hori, "Product Selectivity Affected by Cationic Species in Electrochemical Reduction of CO_2 and CO at a Cu Electrode", *Bulletin of the Chemical Society of Japan* **1991**, *64*, 123–127.

[44] O. Ayemoba, A. Cuesta, "Spectroscopic Evidence of Size-Dependent Buffering of Interfacial pH by Cation Hydrolysis during CO_2 Electroreduction", *ACS Applied Materials & Interfaces* **2017**, *9*, 27377–27382.

[45] J. Resasco, L. D. Chen, E. Clark, C. Tsai, C. Hahn, T. F. Jaramillo, K. Chan, A. T. Bell, "Promoter Effects of Alkali Metal Cations on the Electrochemical Reduction of Carbon Dioxide", *Journal of the American Chemical Society* **2017**, *139*, 11277–11287.

[46] A. S. Malkani, J. Li, N. J. Oliveira, M. He, X. Chang, B. Xu, Q. Lu, "Understanding the electric and nonelectric field components of the cation effect on the electrochemical CO reduction reaction", *Science advances* **2020**, *6*.

[47] M. C. O. Monteiro, F. Dattila, B. Hagedoorn, R. García-Muelas, N. López, M. T. M. Koper, "Absence of CO_2 electroreduction on copper, gold and silver electrodes without metal cations in solution", *Nature Catalysis* **2021**, *4*, 654–662.

[48] A. Goyal, G. Marcandalli, V. A. Mints, M. T. M. Koper, "Competition between CO_2 Reduction and Hydrogen Evolution on a Gold Electrode under Well-Defined Mass Transport Conditions", *Journal of the American Chemical Society* **2020**, *142*, 4154–4161.

[49] T. Burdyny, W. A. Smith, "CO_2 reduction on gas-diffusion electrodes and why catalytic performance must be assessed at commercially-relevant conditions", *Energy & Environmental Science* **2019**, *12*, 1442–1453.

[50] M. H. Levitt, *Spin dynamics: Basics of nuclear magnetic resonance*, 2. ed., Wiley, Chichester, **2015**.

[51] *Understanding NMR Spectroscopy (2004)*, (Ed.: J. Keeler), Apollo - University of Cambridge Repository, **2016**.

[52] R. W. Brown, Y.-C. N. Cheng, E. M. Haacke, M. R. Thompson, R. Venkatesan, Y.-C. N. Cheng, *Magnetic Resonance Imaging: Physical Principles and Sequence Design*, 2nd ed., Wiley, Newark, NJ, **2014**.

[53] M. Pietrzak, S. Jopa, A. Mames, M. Urbanczyk, M. Wozny, T. Ratajczyk, "Recent Progress in Liquid State Electrochemistry Coupled with NMR Spectroscopy", *ChemElectroChem* **2021**, *8*, 4181–4198.

[54] M. M. Britton, "Magnetic resonance imaging of electrochemical cells containing bulk metal", *Chemphyschem : a European journal of chemical physics and physical chemistry* **2014**, *15*, 1731–1736.

[55] J. A. Richards, D. H. Evans, "Flow cell for electrolysis within the probe of a nuclear magnetic resonance spectrometer", *Analytical Chemistry* **1975**, *47*, 964–966.

[56] P. F. d. Silva, B. F. Gomes, C. M. S. Lobo, L. H. K. Queiroz Júnior, E. Danieli, M. Carmo, B. Blümich, L. A. Colnago, "Electrochemical NMR spectroscopy: Electrode construction and magnetic sample stirring", *Microchemical Journal* **2019**, *146*, 658–663.

[57] S. Benders, B. F. Gomes, M. Carmo, L. A. Colnago, B. Blümich, "In-situ MRI velocimetry of the magnetohydrodynamic effect in electrochemical cells", *Journal of magnetic resonance (San Diego Calif. : 1997)* **2020**, *312*, 106692.

[58] R. D. Webster, "*In situ* electrochemical-NMR spectroscopy. Reduction of aromatic halides", *Analytical Chemistry* **2004**, *76*, 1603–1610.

[59] F. Hallberg, I. Furó, P. V. Yushmanov, P. Stilbs, "Sensitive and robust electrophoretic NMR: instrumentation and experiments", *Journal of Magnetic Resonance* **2008**, *192*, 69–77.

[60] S. Klod, F. Ziegs, L. Dunsch, "*In situ* NMR spectroelectrochemistry of higher sensitivity by large scale electrodes", *Analytical Chemistry* **2009**, *81*, 10262–10267.

[61] U. Bussy, P. Giraudeau, V. Silvestre, T. Jaunet-Lahary, V. Ferchaud-Roucher, M. Krempf, S. Akoka, I. Tea, M. Boujtita, "*In situ* NMR spectroelectrochemistry for the structure elucidation of unstable intermediate metabolites", *Analytical and Bioanalytical Chemistry* **2013**, *405*, 5817–5824.

[62] S. Jovanovic, P. P. M. Schleker, M. Streun, S. Merz, P. Jakes, M. Schatz, R.-A. Eichel, J. Granwehr, "An electrochemical cell for *in operando* ^{13}C nuclear magnetic resonance investigations of carbon dioxide/carbonate processes in aqueous solution", *Magnetic Resonance* **2021**, *2*, 265–280.

[63] J. Xie, X. You, Y. Huang, Z. Ni, X. Wang, X. Li, C. Yang, D. Zhang, H. Chen, H. Sun, Z. Chen, "3D-printed integrative probeheads for magnetic resonance", *Nature Communications* **2020**, *11*, 5793.

[64] M. M. Britton, P. M. Bayley, P. C. Howlett, A. J. Davenport, M. Forsyth, "*In Situ*, Real-Time Visualization of Electrochemistry Using Magnetic Resonance Imaging", *The Journal of Physical Chemistry Letters* **2013**, *4*, 3019–3023.

[65] S. Krachkovskiy, M. L. Trudeau, K. Zaghib, "Application of Magnetic Resonance Techniques to the *In Situ* Characterization of Li-Ion Batteries: A Review", *Materials (Basel Switzerland)* **2020**, *13*.

[66] O. Pecher, J. Carretero-González, K. J. Griffith, C. P. Grey, "Materials' Methods: NMR in Battery Research", *Chemistry of Materials* **2017**, *29*, 213–242.

[67] S. Chandrashekar, N. M. Trease, H. J. Chang, L.-S. Du, C. P. Grey, A. Jerschow, "^{7}Li MRI of Li batteries reveals location of microstructural lithium", *Nature materials* **2012**, *11*, 311–315.

[68] R. Bhattacharyya, B. Key, H. Chen, A. S. Best, A. F. Hollenkamp, C. P. Grey, "*In situ* NMR observation of the formation of metallic lithium microstructures in lithium batteries", *Nature materials* **2010**, *9*, 504–510.

[69] S. A. Krachkovskiy, J. D. Bazak, P. Werhun, B. J. Balcom, I. C. Halalay, G. R. Goward, "Visualization of Steady-State Ionic Concentration Profiles Formed in Electrolytes during Li-Ion Battery Operation and Determination of Mass-Transport Properties by *in Situ* Magnetic Resonance Imaging", *Journal of the American Chemical Society* **2016**, *138*, 7992–7999.

[70] S. A. Kayser, A. Mester, A. Mertens, P. Jakes, R.-A. Eichel, J. Granwehr, "Long-run *in operando* NMR to investigate the evolution and degradation of battery cells", *Physical chemistry chemical physics : PCCP* **2018**, *20*, 13765–13776.

[71] S. Klamor, K. Zick, T. Oerther, F. M. Schappacher, M. Winter, G. Brunklaus, "^{7}Li *in situ* 1D NMR imaging of a lithium ion battery", *Physical Chemistry Chemical Physics* **2015**, *17*, 4458–4465.

[72] H. J. Chang, A. J. Ilott, N. M. Trease, M. Mohammadi, A. Jerschow, C. P. Grey, "Correlating Microstructural Lithium Metal Growth with Electrolyte Salt Depletion in Lithium Batteries Using ^{7}Li MRI", *Journal of the American Chemical Society* **2015**, *137*, 15209–15216.

[73] A. J. Ilott, M. Mohammadi, H. J. Chang, C. P. Grey, A. Jerschow, "Real-time 3D imaging of microstructure growth in battery cells using indirect MRI", *Proceedings of the National Academy of Sciences of the United States of America* **2016**, *113*, 10779–10784.

[74] K. Romanenko, M. Forsyth, L. A. O'Dell, "New opportunities for quantitative and time efficient 3D MRI of liquid and solid electrochemical cell components: Sectoral Fast Spin Echo and SPRITE", *Journal of Magnetic Resonance* **2014**, *248*, 96–104.

[75] G. J. Rees, D. Spencer Jolly, Z. Ning, T. J. Marrow, G. E. Pavlovskaya, P. G. Bruce, "Imaging Sodium Dendrite Growth in All–Solid–State Sodium Batteries Using 23 Na T2 –Weighted Magnetic Resonance Imaging", *Angewandte Chemie* **2021**, *133*, 2138–2143.

[76] J. M. Bray, C. L. Doswell, G. E. Pavlovskaya, L. Chen, B. Kishore, H. Au, H. Alptekin, E. Kendrick, M.-M. Titirici, T. Meersmann, M. M. Britton, "Operando visualisation of battery chemistry in a sodium-ion battery by ^{23}Na magnetic resonance imaging", *Nature Communications* **2020**, *11*, 2083.

[77] Y. Xiang, G. Zheng, Z. Liang, Y. Jin, X. Liu, S. Chen, K. Zhou, J. Zhu, M. Lin, H. He, J. Wan, S. Yu, G. Zhong, R. Fu, Y. Li, Y. Yang, "Visualizing the growth process of sodium microstructures in sodium batteries by in-situ ^{23}Na MRI and NMR spectroscopy", *Nature Nanotechnology* **2020**, *15*, 883–890.

[78] M. Schatz, S. Jovanovic, R.-A. Eichel, J. Granwehr, "Quantifying local pH changes in carbonate electrolyte during copper-catalysed CO_2 electroreduction using *in operando* ^{13}C NMR", *Scientific Reports* **2022**, *12*.

[79] R. I. Masel, Z. Liu, H. Yang, J. J. Kaczur, D. Carrillo, S. Ren, D. Salvatore, C. P. Berlinguette, "An industrial perspective on catalysts for low-temperature CO_2 electrolysis", *Nature nanotechnology* **2021**.

[80] M. Gattrell, N. Gupta, A. Co, "A review of the aqueous electrochemical reduction of CO_2 to hydrocarbons at copper", *Journal of Electroanalytical Chemistry* **2006**, *594*, 1–19.

[81] A. A. Peterson, F. Abild-Pedersen, F. Studt, J. Rossmeisl, J. K. Nørskov, "How copper catalyzes the electroreduction of carbon dioxide into hydrocarbon fuels", *Energy & Environmental Science* **2010**, *3*, 1311.

[82] S. Zhu, B. Jiang, W.-B. Cai, M. Shao, "Direct Observation on Reaction Intermediates and the Role of Bicarbonate Anions in CO_2 Electrochemical Reduction Reaction on Cu Surfaces", *Journal of the American Chemical Society* **2017**, *139*, 15664–15667.

[83] M. Dunwell, X. Yang, B. P. Setzler, J. Anibal, Y. Yan, B. Xu, "Examination of Near-Electrode Concentration Gradients and Kinetic Impacts on the Electrochemical Reduction of CO_2 using Surface-Enhanced Infrared Spectroscopy", *ACS Catalysis* **2018**, *8*, 3999–4008.

[84] J. Resasco, Y. Lum, E. Clark, J. Z. Zeledon, A. T. Bell, "Effects of Anion Identity and Concentration on Electrochemical Reduction of CO_2", *ChemElectroChem* **2018**, *5*, 1064–1072.

[85] A. D. Handoko, C. W. Ong, Y. Huang, Z. G. Lee, L. Lin, G. B. Panetti, B. S. Yeo, "Mechanistic Insights into the Selective Electroreduction of Carbon Dioxide to Ethylene on Cu_2O-Derived Copper Catalysts", *The Journal of Physical Chemistry C* **2016**, *120*, 20058–20067.

[86] A. S. Hall, Y. Yoon, A. Wuttig, Y. Surendranath, "Mesostructure-Induced Selectivity in CO_2 Reduction Catalysis", *Journal of the American Chemical Society* **2015**, *137*, 14834–14837.

[87] M. Moradzaman, G. Mul, "Infrared Analysis of Interfacial Phenomena during Electrochemical Reduction of CO_2 over Polycrystalline Copper Electrodes", *ACS Catalysis* **2020**, *10*, 8049–8057.

[88] S. Sen, D. Liu, G. T. R. Palmore, "Electrochemical Reduction of CO_2 at Copper Nanofoams", *ACS Catalysis* **2014**, *4*, 3091–3095.

[89] S. E. Weitzner, S. A. Akhade, J. B. Varley, B. C. Wood, M. Otani, S. E. Baker, E. B. Duoss, "Toward Engineering of Solution Microenvironments for the CO_2 Reduction Reaction: Unraveling pH and Voltage Effects from a Combined Density-Functional-Continuum Theory", *The Journal of Physical Chemistry Letters* **2020**, *11*, 4113–4118.

[90] M. C. Monteiro, M. T. Koper, "Measuring local pH in electrochemistry", *Current Opinion in Electrochemistry* **2021**, *25*, 100649.

[91] K. Yang, R. Kas, W. A. Smith, "*In Situ* Infrared Spectroscopy Reveals Persistent Alkalinity near Electrode Surfaces during CO_2 Electroreduction", *Journal of the American Chemical Society* **2019**, *141*, 15891–15900.

[92] D. A. Henckel, M. J. Counihan, H. E. Holmes, X. Chen, U. O. Nwabara, S. Verma, J. Rodríguez-López, P. J. A. Kenis, A. A. Gewirth, "Potential Dependence of the Local pH in a CO_2 Reduction Electrolyzer", *ACS Catalysis* **2021**, *11*, 255–263.

[93] D. J. Scholz, M. A. Janich, U. Köllisch, R. F. Schulte, J. H. Ardenkjaer-Larsen, A. Frank, A. Haase, M. Schwaiger, M. I. Menzel, "Quantified pH imaging with hyperpolarized ^{13}C-bicarbonate", *Magnetic Resonance in Medicine* **2015**, *73*, 2274–2282.

[94] Y. Hori, H. Konishi, T. Futamura, A. Murata, O. Koga, H. Sakurai, K. Oguma, ""Deactivation of copper electrode" in electrochemical reduction of CO_2", *Electrochimica Acta* **2005**, *50*, 5354–5369.

[95] D. T. Sawyer, A. Sobkowiak, J. L. Roberts, *Electrochemistry for chemists*, 2. ed., Wiley, New York, **1995**.

[96] R. W. Adams, C. M. Holroyd, J. A. Aguilar, M. Nilsson, G. A. Morris, "'Perfecting" WATERGATE: clean proton NMR spectra from aqueous solution", *Chemical Communications* **2013**, *49*, 358–360.

[97] I. Katsounaros, J. C. Meier, S. O. Klemm, A. A. Topalov, P. U. Biedermann, M. Auinger, K. J. Mayrhofer, "The effective surface pH during reactions at the solid–liquid interface", *Electrochemistry Communications* **2011**, *13*, 634–637.

[98] K. Y. Leung, C. C. L. McCrory, "Effect and Prevention of Trace Ag + Contamination from Ag/AgCl Reference Electrodes on CO_2 Reduction Product Distributions at Polycrystalline Copper Electrodes", *ACS Applied Energy Materials* **2019**, *2*, 8283–8293.

[99] J. J. Helmus, C. P. Jaroniec, "Nmrglue: an open source Python package for the analysis of multidimensional NMR data", *Journal of biomolecular NMR* **2013**, *55*, 355–367.

[100] D. Li, N. Li, G. Xia, Z. Zheng, J. Wang, N. Xiao, W. Zhai, G. Wu, "An in-situ study of copper electropolishing in phosphoric acid solution", *Int. J. Electrochem. Sci* **2013**, *8*, 1041.

[101] G. Jiang, D. Han, Z. Han, J. Gao, X. Wang, Z. Weng, Q.-H. Yang, "Rational Manipulation of Intermediates on Copper for CO_2 Electroreduction Toward Multicarbon Products", *Transactions of Tianjin University* **2022**, *28*, 265–291.

[102] C. He, M. D. Guiver, F. Mighri, S. Kaliaguine, "Surface orientation of hydrophilic groups in sulfonated poly(ether ether ketone) membranes", *Journal of colloid and interface science* **2013**, *409*, 193–203.

[103] G. B. Darband, M. Aliofkhazraei, S. Shanmugam, "Recent advances in methods and technologies for enhancing bubble detachment during electrochemical water splitting", *Renewable and Sustainable Energy Reviews* **2019**, *114*, 109300.

[104] M. Moura de Salles Pupo, R. Kortlever, "Electrolyte Effects on the Electrochemical Reduction of CO_2", *Chemphyschem : a European journal of chemical physics and physical chemistry* **2019**, *20*, 2926–2935.

[105] J.-B. Vennekötter, T. Scheuermann, R. Sengpiel, M. Wessling, "The electrolyte matters: Stable systems for high rate electrochemical CO_2 reduction", *Journal of CO_2 Utilization* **2019**, *32*, 202–213.

[106] Y. Hori, R. Takahashi, Y. Yoshinami, A. Murata, "Electrochemical Reduction of CO at a Copper Electrode", *The Journal of Physical Chemistry B* **1997**, *101*, 7075–7081.

[107] J. E. Huang, F. Li, A. Ozden, A. Sedighian Rasouli, F. P. García de Arquer, S. Liu, S. Zhang, M. Luo, X. Wang, Y. Lum, Y. Xu, K. Bertens, R. K. Miao, C.-T. Dinh, D. Sinton, E. H. Sargent, "CO_2 electrolysis to multicarbon products in strong acid", *Science* **2021**, *372*, 1074–1078.

[108] X. Zhu, J. Huang, M. Eikerling, "Electrochemical CO_2 Reduction at Silver from a Local Perspective", *ACS Catalysis* **2021**, *11*, 14521–14532.

[109] M. M. Waegele, C. M. Gunathunge, J. Li, X. Li, "How cations affect the electric double layer and the rates and selectivity of electrocatalytic processes", *The Journal of chemical physics* **2019**, *151*, 160902.

[110] F. Zhang, A. C. Co, "Direct Evidence of Local pH Change and the Role of Alkali Cation during CO_2 Electroreduction in Aqueous Media", *Angewandte Chemie (International ed. in English)* **2020**, *59*, 1674–1681.

[111] M. R. Singh, Y. Kwon, Y. Lum, J. W. Ager, A. T. Bell, "Hydrolysis of Electrolyte Cations Enhances the Electrochemical Reduction of CO_2 over Ag and Cu", *Journal of the American Chemical Society* **2016**, *138*, 13006–13012.

[112] A. S. Malkani, J. Anibal, B. Xu, "Cation Effect on Interfacial CO_2 Concentration in the Electrochemical CO_2 Reduction Reaction", *ACS Catalysis* **2020**, *10*, 14871–14876.

[113] S. Dieckhöfer, D. Öhl, J. R. C. Junqueira, T. Quast, T. Turek, W. Schuhmann, "Probing the Local Reaction Environment During High Turnover Carbon Dioxide Reduction with Ag-Based Gas Diffusion Electrodes", *Chemistry (Weinheim an der Bergstrasse Germany)* **2021**, *27*, 5906–5912.

[114] M. C. O. Monteiro, A. Mirabal, L. Jacobse, K. Doblhoff-Dier, S. C. Barton, M. T. M. Koper, "Time-Resolved Local pH Measurements during CO_2 Reduction Using Scanning Electrochemical Microscopy: Buffering and Tip Effects", *JACS Au* **2021**, *1*, 1915–1924.

[115] A. J. Welch, A. Q. Fenwick, A. Böhme, H.-Y. Chen, I. Sullivan, X. Li, J. S. DuChene, C. Xiang, H. A. Atwater, "Operando Local pH Measurement within Gas Diffusion Electrodes Performing Electrochemical Carbon Dioxide Reduction", *The Journal of Physical Chemistry C* **2021**, *125*, 20896–20904.

[116] X. Lu, C. Zhu, Z. Wu, J. Xuan, J. S. Francisco, H. Wang, "*In Situ* Observation of the pH Gradient near the Gas Diffusion Electrode of CO_2 Reduction in Alkaline Electrolyte", *Journal of the American Chemical Society* **2020**, *142*, 15438–15444.

[117] T. J. Edwards, G. Maurer, J. Newman, J. M. Prausnitz, "Vapor-liquid equilibria in multicomponent aqueous solutions of volatile weak electrolytes", *AIChE Journal* **1978**, *24*, 966–976.

[118] H. Matsushima, T. Iida, Y. Fukunaka, "Gas bubble evolution on transparent electrode during water electrolysis in a magnetic field", *Electrochimica Acta* **2013**, *100*, 261–264.

[119] C. Deverell, R. E. Richards, "Nuclear magnetic resonance studies of alkali metal halide solutions", *Molecular Physics* **1966**, *10*, 551–564.

[120] Z.-X. Luo, Y.-Z. Xing, S. Liu, Y.-C. Ling, A. Kleinhammes, Y. Wu, "Dehydration of Ions in Voltage-Gated Carbon Nanopores Observed by *in Situ* NMR", *The Journal of Physical Chemistry Letters* **2015**, *6*, 5022–5026.

[121] H. H. Heenen, H. Shin, G. Kastlunger, S. Overa, J. A. Gauthier, F. Jiao, K. Chan, "The mechanism for acetate formation in electrochemical CO_2 reduction on Cu: selectivity with potential, pH, and nanostructuring", *Energy & Environmental Science* **2022**, *15*, 3978–3990.

[122] Least squares fitting with kmpfit — Kapteyn Package (home), **11.10.2019**.

[123] J. R. Wolberg, *Data analysis using the least-squares method: How to extract the most information from experiments*, Springer, Berlin and London, **2005**.